Université d'Ottawa • University of Ottawa

Université d'Ottawa · University of Ottawa

FACULTÉ DES ÉTUDES SUPÉRIEURES ET POSTDOCTORALES

FACULTY OF GRADUATE AND POSTDOCTORAL STUDIES

Graham Alan FERRIER

AUTEUR DE LA THÈSE - AUTHOR OF THESIS

M. Sc. (Physics)

GRADE - DEGREE

Department of Physics

FACULTÉ, ÉCOLE, DÉPARTEMENT - FACULTY, SCHOOL, DEPARTMENT

TITRE DE LA THÈSE - TITLE OF THE THESIS

Spectral Characterization of Distributed Brillouin Sensors in the Transient Regime

X. Bao

DIRECTEUR DE LA THÈSE - THESIS SUPERVISOR

CO-DIRECTEUR DE LA THÈSE - THESIS CO-SUPERVISOR

EXAMINATEURS DE LA THÈSE - THESIS EXAMINERS

J. Armitage

R. Munger

R. Williams

J.-M. De Koninck, Ph.D.

LE DOYEN DE LA FACULTÉ DES ÉTUDES SUPÉRIEURES ET POSTDOCTORALES

SIGNATURE

DEAN OF THE FACULTY OF GRADUATE AND POSTDOCTORAL STUDIES

Spectral Characterization of Distributed Brillouin Sensors in the Transient Regime

By

Graham Alan Ferrier

Thesis submitted to
the Faculty of Graduate and Postdoctoral Studies
in Partial Fulfillment of the Requirements for the Degree of

Master of Science

Ottawa-Carleton Institute for Physics
University of Ottawa
Ottawa, Canada
November 2003

Your file Votre référence
ISBN: 0-612-90070-3
Our file Notre référence
ISBN: 0-612-90070-3

Abstract

Brillouin scattering based fibre optic sensors have been actively researched over the past decade due to their enhanced sensitivity to environmental parameters such as temperature and strain. Applications range from dynamic health monitoring of civil structures such as bridges, pipelines, and nuclear reactors to real-time threshold applications such as fire detection. As temperature and strain changes often represent the first symptoms of structural degradation, the development of Brillouin scattering based technology will bear considerable scientific as well as economic benefit.

Brillouin sensors employing the probe-pump amplification technique obtain distributed spatial information along a fibre using narrow pulses. In this study, the impact of pulse width and extinction ratio on the overall Brillouin spectrum shape is investigated. From independent theoretical and experimental investigations, a comprehensive curve fitting method is proposed to reveal the physical nature of Brillouin scattering in the transient regime.

Acknowledgements

I would like to thank my supervisor, Prof. Xiaoyi Bao, for providing me this opportunity to engage in fibre optics research. I have greatly enjoyed learning from our enlightening discussions on Brillouin scattering and various physics topics, and am thankful for her promptness and patience throughout my learning process. I am also appreciative of the opportunity to work with many experienced and skilled colleagues. Early in the research effort, Xiaodong Zeng, Qinrong Yu and Guilin Wu were excellent coworkers whom worked long hours to help assemble and test the Brillouin scattering apparatus. In addition, they taught me valuable information regarding various electrical and optical components within the system. I'll always remember the road trips, and experiences gained during field tests! I wish to thank Shahraam Afshar for working long hours with me on simulations, and for his contagious positive outlook on research. Our discussions were always informative and often entertaining. Always remember, "We love T_0, the Weibull profile, and Gain flattening…along with funny looking Brillouin spectra!" Thanks also for introducing me to MATLAB, Fortran, and Scientific Workplace!

Many thanks go to Lufan Zou for working diligently with me on various experimental investigations and for always challenging my opinions and assumptions. I have truly appreciated his hard work, continuous encouragement, and positive attitude! I wish to thank Brendan Lake for assisting me in preparing the temperature spectrum measurements and for many Brillouin scattering Q&A sessions. Many thanks also go to Prof. Liang Chen for arranging regular enlightening group seminars, and challenging us all with tough, but often fundamental questions. I thank all past and present Fibre Optic Group members and the University of Ottawa Physics Department for providing an easy-going and pleasant learning environment. I wish to thank Robert Steffen, Marc Demers, Sankara Papavinasam, Andrew Johnston, and Zhigang Liu for their supervision and contributions to specific projects. I wish to thank the University of Ottawa and ISIS Canada for financial support of this research. Finally, I express deepest thanks to my family for always believing in me and pushing me forward, and to God for making absolutely everything possible.

TABLE OF CONTENTS

List of Figures

List of Tables

Chapter 1: Introduction

Over the past decade, fibre optic technology has emerged as a dominating field of scientific research through numerous sensing and communication applications. Optical fibres offer a variety of advantageous properties including low attenuation, fast response, immunity to electromagnetic interference, and high sensitivity to physical parameters such as temperature and strain. One approach to retrieving strain and temperature information from optical fibres involves measuring their nonlinear response to strong laser fields. In particular, the strongest nonlinear response occurs when the material responds macroscopically giving rise to a light scattering process known as Brillouin scattering.

Brillouin scattering is a three-wave inelastic scattering of incident, coherent light (photons) from the dynamic macroscopic thermal fluctuations (phonons) within a transparent material such as silica (SiO_2) optical fibre. In this photon-phonon process, a laser beam propagates axially along the fibre and a small portion (1 in 10^5) scatters from the existing thermal fluctuations. Since the molecules of all media exhibit thermal motion at a temperature above absolute zero, this *dynamic* photon-phonon interaction will couple energy into the natural vibrational modes of the structure, creating a sound wave. The scattered light thus emerges from the interaction at a Doppler shifted higher or lower frequency depending on the direction of the sound wave, whose frequency spectrum can then be characterized in terms of the strain and thermal histories within the fibre.

Distributed temperature and strain sensing is achieved using Brillouin optical time domain analysis (BOTDA) whereby an optical pulse of width τ is delivered into a proximal fibre end while a counter-propagating continuous wave (CW) pump light beam arrives from the distal end. When these beams interact within a timeframe $T \rightarrow T+\tau$, a mutual energy exchange between the beams occurs and the pump signal depletion (or amplification) of duration τ is detected at the proximal fibre end after a timeframe $2T \rightarrow 2T+\tau$. Consequently, the signal detected within this timeframe corresponds to an interaction occurring over timeframe $T \rightarrow T+\tau$, thus providing a means for obtaining the spatial information. The energy exchange process is called Brillouin gain or loss [Bao *et al.* 1993a, Bao *et al.* 1993b] depending on whether the pump beam gains or loses energy during the interaction, and is governed by the relative frequencies of the two counter-propagating laser beams. In our system, the Brillouin loss method is preferred since it gives rise to amplified pulses rather than depleted ones, and consequently allows for measuring longer fibre lengths and enhanced signal-to-noise ratios (SNR).

1.1 Research Objectives

This thesis presents a contribution to the ongoing research in distributed fibre optic sensing at the University of Ottawa. Our research began at the University of New Brunswick where over four years, an automated distributed fibre optic sensing system capable of measuring either strain or temperature with enhanced spatial resolution capability (< 1 m) was developed. In that time, numerous laboratory and theoretical investigations confirmed that simultaneous distributed sensing of temperature and strain was achievable [Smith 1999, DeMerchant 2000, Brown 2000]. With this in mind, the research focussed on testing the system performance in real field applications where environmental factors impose the major limitations on physical measurements. During that time, Zeng and coworkers acquired physical measurements of a bridge, nuclear reactor, and a concrete curing process [Zeng 2003] using this system.

This thesis aims to improve on the conventional understanding of the Brillouin spectrum when implementing optical pulses shorter than the phonon lifetime of silica (~ 10 ns). Although narrow pulses naturally lead to short spatial resolutions, they can also significantly broaden the Brillouin spectral linewidth. Since the Brillouin linewidth is a measure of temperature and strain accuracy, it is important to understand the conditions whereby the linewidth narrows or broadens. In addition, although BOTDA is a standard mechanism for acquiring spatial information, its effectiveness is hampered when employing an electro-optic modulator (EOM) for optical pulse generation. Essentially, due to design limitations, the EOM continuously allows a small amount of CW light to enter the fibre when the laser is active. Therefore, the subsequent CW interactions before and after the pulse enters a given fibre position influence the resulting Brillouin spectrum by carrying the temperature and strain information from the neighbouring regions toward the detector.

This thesis begins with an introduction to nonlinear optics and Brillouin scattering. Next, a description of the experimental apparatus is given with emphasis on the working principles of the main optical components that manipulate the light before and after the Brillouin scattering process in the sensing fibre occurs. The remaining chapters detail the main results of the thesis. Chapter 4 describes the competition of co-propagating CW (leakage) and pulsed light waves for amplification from an oncoming CW pump beam and the implications of leakage on the Brillouin spectrum. Chapter 5 introduces the concept of Brillouin temperature spectra for threshold monitoring, and Chapter 6 presents the circumferential and longitudinal strain distributions along an internally pressurized end-capped 1.8 m steel pipeline. Finally, Chapter 7 summarizes the main findings and discusses possibilities for future development.

Chapter 2: Nonlinear Optics and Brillouin Scattering

This chapter describes the response of a dielectric material to an electric field. In particular, an input electric field having frequency dependent (E_{ω}) and independent (E_{DC}) components generates various parametric and inelastic processes. From the laws of energy and momentum conservation, the inelastic processes yield Stokes and Anti-Stokes scattered waves along with optical and acoustic phonons. The inelastic process yielding acoustic phonons is Brillouin scattering. From the momentum vector diagram of the Brillouin scattering process, a derivation of the Brillouin frequency (acoustic phonon frequency) will provide a relationship between material properties such as refractive index and acoustic velocity (n, V_a) and physical properties such as strain and temperature. Finally, a discussion of spontaneous, stimulated, and amplified Brillouin scattering will aid in facilitating the investigation and understanding of light interaction in the fibre.

2.1 Nonlinear Optics

Nonlinear studies in optics awaited the advent of laser technology since the electric field and power density of incoherent sunlight (~100 V/m and 20 W/m^2) and those of other non-laser light sources were insufficient to produce nonlinear effects, which only occur when the electric field is intense (E ~ 10^5 V/m) [Shen 1984] and when the light source is coherent. Consequently, the invention of the laser (E ~ 10^6 V/m, I ~ 10^9 W/m^2) in 1960 effectively unleashed a series of interesting linear and nonlinear optical phenomena; many of which are listed in Table 2.1.

The linear responses in dielectric materials are measured in terms of the polarization induced in the material by an electric field. When a neutral molecule is placed in an electric field, its positive ($+q$) and negative ($-q$) charges are pulled in opposite directions. An electric dipole is effectively created when the centres of positive and negative charge become separated by a distance $-\vec{r}$, and thus the molecule acquires a dipole moment $\vec{p} = q\vec{r}$, where $-q$ is the electric charge. If there are N molecules per unit volume, then the electric polarization (i.e.

dipole moment per unit volume) becomes $\vec{P} = N\vec{p}$ [Yariv 1971]. Therefore, the molecule becomes *polarized* in the presence of an electric field. Nonlinear responses, however, become possible through the anharmonic response of bound electrons to increasing input electric fields. Since the electric field intensities in this regime are comparable to the forces that bind electrons to nuclei, the refractive index will vary with the electric field, thus making the dielectric itself a radiation source by changing the frequency of light propagation.

Linear: 1st Order Classical Optics:	Nonlinear: 2nd order Materials lacking inversion symmetry:	Nonlinear: 3rd order
Superposition Reflection Refraction Birefringence Absorption	2nd harmonic generation Three-wave mixing Optical Rectification Parametric Amplification Pockel's Effect	3rd harmonic generation Kerr Effect Raman Scattering *Brillouin Scattering* Optical Phase Conjugation Four-wave Mixing

Table 2.1: Linear and Nonlinear Processes [Pedrotti and Pedrotti 1993]

Nonlinear optics generally consists of two processes: parametric and inelastic. Parametric processes collectively describe situations where the dielectric material is passive and only mediates the interaction among several optical waves. In other words, the nuclei are assumed to remain fixed, and the resulting effects arise purely from the existence of the input electric field. Such processes are *parametric* because they involve modulation of a medium parameter such as the refractive index. Inelastic processes, however, require the dielectric material to actively participate in the process through either molecular vibrations (Raman scattering) or density variations (Brillouin scattering). Such processes take into account the instantaneous nuclear positions in addition to the input field.

2.2 Parametric Processes

When the polarization is investigated in terms of the input electric field, various parametric processes can be mathematically deduced. As shown in Equation 2.1 [Pedrotti and Pedrotti 1993], the polarization is expressed generally as a power series of the electric field, where ε_0 is the vacuum permittivity and the susceptibilities, $\chi^{(m)}$, are defined as the ease with which positive and negative charges can be separated by an applied electric field. The linear susceptibility is $\chi^{(1)}$ and the nonlinear second and third order susceptibilities are $\chi^{(2)}$ and $\chi^{(3)}$ respectively. The susceptibilities are normally (m+1) rank tensors having $3^{(m+1)}$ elements, but can be expressed as pure constants depending on material symmetry and the crystalline orientation relative to the input electric field. Since the magnitudes of $\chi^{(m)}$ drop off rapidly with increasing m, the polarization is practically expressed to the third order.

$$P = \varepsilon_0\left(\chi^{(1)}E + \chi^{(2)}E^2 + \chi^{(3)}E^3 + ...\right) \tag{2.1}$$

When an input plane wave ($E = E_0 \cos\omega t$) propagates through a material, the resulting polarization (Equation 2.3) comprises additional harmonics (2ω, 3ω...) along with a frequency independent component known as optical rectification [Bass *et al.* 1962b]. However, both optical rectification and second harmonic generation (SHG) [Franken *et al.* 1961] cannot generally be produced in silica optical fibres due to their isotropic nature (i.e. P=-P as E=-E $\rightarrow \chi^{(2)}=0$). However, SHG can occur when a permanent static field develops in the optical fibre and couples through the $\chi^{(3)}$ term [Fujii 1980, Agrawal 1995, Moll 2002].

$$P(t) = \varepsilon_0\left(\chi^{(1)}E_0 \cos\omega t + \chi^{(2)}E_0^{\;2}\cos^2\omega t + \chi^{(3)}E_0^{\;3}\cos^3\omega t\right) \tag{2.2}$$

$$P(t) = \varepsilon_0\left(\chi^{(1)}E_0 \cos\omega t + \chi^{(2)}E_0^{\;2}\frac{1}{2}(1+\cos 2\omega t) + \chi^{(3)}E_0^{\;3}\frac{1}{4}(3\cos\omega t + \cos 3\omega t)\right) \tag{2.3}$$

When two fields of different frequencies ω_1 and ω_2 propagate in an optical material, their interference leads to output signals with frequencies $\omega_1 + \omega_2$ and $\omega_1 - \omega_2$. The processes are called sum and difference frequency generation [Bass *et al.* 1962a] and represent the more general case of second harmonic generation ($\omega_1 + \omega_2 = 2\omega_1$) and optical rectification ($\omega_1 - \omega_2 = 0$) respectively.

In linear optics, the refractive index is a constant value defined as $n=\sqrt{\varepsilon_r}=\sqrt{1+\chi^{(1)}}$, where ε_r is the relative permittivity of the material. However, in nonlinear optics, the refractive index becomes affected by the input electric field. The linear electro-optic effect (Pockels effect) results in electro-optic amplitude (e.g. section 3.2) or phase modulation whereas the quadratic electro-optic effect (Kerr effect) appears as a refractive index change induced by the electric field intensity ($I=c\varepsilon E^2$). Hence, the optical AC Kerr effect is given by

$$n=n_1+n_2 I \tag{2.4}$$

where n_l is the average refractive index, and the nonlinear refractive index for amorphous silica is $n_2 \approx 3.2\times10^{-20}\, m^2/W$ [Stolen and Lin 1978]. The nonlinear refractive index plays a critical role in effects such as self phase modulation (SPM) and cross phase modulation (XPM) [Agrawal 1997]. As shown in Table 2.2, the DC Kerr effect has a similar form but arises from a static field intensity, I_{DC}.

$\varepsilon_0\chi^{(1)}\{E(\cos\omega_1 t+\cos\omega_2 t)+E_{DC}\}$	Linear Optics
$\varepsilon_0\chi^{(2)}E^2(1+E_{DC})[\cos(\omega_1+\omega_2)t+\cos(\omega_2-\omega_1)t]$	Sum/Difference Frequency Generation
$\frac{1}{2}\varepsilon_0\chi^{(2)}E^2[\cos 2\omega_1 t+\cos 2\omega_2 t]$	Second Harmonic Generation
$\frac{1}{4}\varepsilon_0\chi^{(3)}E^3[\cos 3\omega_1 t+\cos 3\omega_2 t]$	Third Harmonic Generation
$\frac{3}{4}\varepsilon_0\chi^{(3)}E^3[\cos(\pm 2\omega_1\pm\omega_2)t+\cos(\pm 2\omega_2\pm\omega_1)t]$	Parametric Frequency Generation
$\frac{9}{4}\varepsilon_0\chi^{(3)}E^3[\cos\omega_1 t+\cos\omega_2 t]$	Optical (AC) Kerr Effect
$3\varepsilon_0\chi^{(3)}E_{DC}{}^2E[\cos\omega_1 t+\cos\omega_2 t]$	Quadratic (DC) Kerr Effect

Table 2.2: Common linear and nonlinear polarization effects derived using Equations 2.1 and 2.5.

Using a generalized input electric field having co-propagating optical frequencies, ω_1 and ω_2, along with a DC component given by

$$E_{input}(t) = E\cos(\omega_1 t) + E\cos(\omega_2 t) + E_{DC}, \tag{2.5}$$

yields the linear and nonlinear polarization terms shown in Table 2.2.

2.3 Inelastic Processes

Processes involving energy transfer from the optical wave to the surrounding material wherein the energy changes in form are inelastic processes. Two such processes are Raman and Brillouin scattering [Raman 1928, Brillouin 1922].

2.3.1 Raman Scattering

Raman scattering is based on the inelastic scattering of photons from changes in the dielectric polarizability, which result from vibrational motion. The polarizability can be altered either by applying an electric field or simply from the vibrational motion of molecules at given temperatures. The former method can be explained by considering the simple classical picture of a linear chain of silicon and oxygen atoms shown in Figure 2.1 [Mauro 2003].

Typically, the interaction between incident light and the material occurs through its electron clouds since they occupy more space than their respective nuclei. In particular, the incident beam will initiate atomic polarization by deforming the electron cloud such that the centres of positive and negative charge no longer coincide with one another. In Figure 2.1, the process begins when the input field polarizes the first silicon atom (dark-shaded circle). To restore charge equilibrium, the neighbouring oxygen atom (light-shaded circle) will polarize itself in the opposite direction. The next silicon atom responds likewise to the polarization of the oxygen atom, and finally a chain reaction of shifting electron clouds (outer rings) results. Connecting the centres of negative charge reveals a sinusoidal perturbation in the volume susceptibility. Such a perturbation constitutes an *optical phonon* since the deformation of electron clouds respond with speeds comparable to light speed.

In the above example, since the incident photon gives energy in creating the optical phonon, its frequency when scattered will be downshifted. Quantum mechanically, the molecule is excited into a higher energy vibrational state. However, when the material already exhibits vibrational motion in higher, discrete energy states (i.e. higher temperatures), the photon-phonon interaction annihilates the existing phonon, i.e. it reduces to a lower energy vibrational state. The scattered beams are referred to as Stokes and Anti-Stokes (see section 2.3.2.2) when optical phonons are created and annihilated respectively.

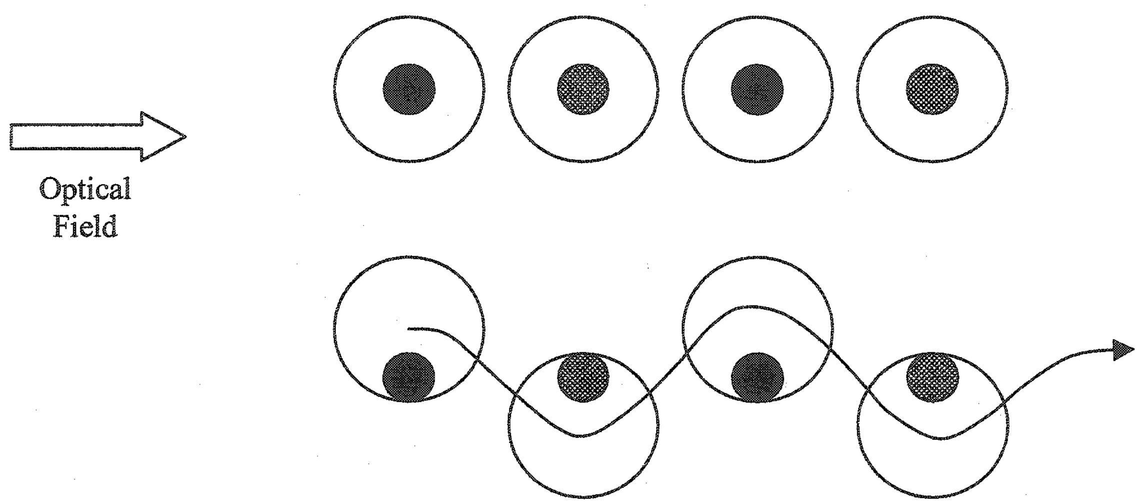

Figure 2.1: Optical Phonon Propagation [Mauro 2003]. The dark- and light-shaded circles are silicon and oxygen atoms, respectively, while the outer rings represent the outer boundary of the electron cloud.

When the molecules are in thermal equilibrium, the quantum level is averaged over a Boltzmann distribution [Mills 1998]. Therefore, the population of molecules in the ground state and excited states will determine the intensities of the Anti-Stokes and Stokes Raman lines (I_{AS} and I_S), through

$$\frac{I_{AS}}{I_S} = \frac{\omega_{AS}^4}{\omega_S^4}\exp\left(-\frac{h\nu}{kT}\right) \tag{2.6}$$

where h and k are the Planck and Boltzmann constants, ω_{AS} and ω_S are the Anti-Stokes and Stokes frequencies, T is the fibre temperature, and ν is the frequency of the exciting line.

Typically, the Stokes line is stronger than the Anti-Stokes line since there is a low population of molecules in excited states when operating at room temperature. When $T = 0K$, there are zero molecules originally in the excited state (i.e. $I_{AS}=0$) whereas when $T \to \infty$, the anti-Stokes intensity reaches a maximum given by

$$\frac{I_{AS}}{I_S} = \frac{\omega_{AS}^4}{\omega_S^4}. \tag{2.7}$$

Finally, the phase matching conditions between the pump and scattered waves are flexible in Raman scattering since the material is amorphous having many vibrational and rotational frequencies among the varying-strength and varying-orientation chemical bonds [Rogers 2000]. Hence, Raman scattering occurs over a broad range of frequencies (THz).

2.3.2 Brillouin Scattering

Brillouin scattering is based on the inelastic scattering of photons from moving density fluctuations in the fibre, which result from naturally occurring lattice vibrations (spontaneous) or from strong forces exerted by the input electric field upon the molecular structure (stimulated). The spontaneous and stimulated Brillouin scattering processes are discussed further in sections 2.6 and 2.7. Since the density varies with time and position, the scattered photons experience a Doppler frequency shift with a magnitude equal to the frequency of the density fluctuations. Through direct proportionality ($E = \hbar\omega$), this frequency shift represents the corresponding energy difference between the incident and scattered photons. This energy difference represents the energy of *acoustic phonons* (sound waves).

However, in contrast with Raman scattering, Brillouin scattering requires a more stringent phase-matching condition between the incident and scattered (Stokes or Anti-Stokes) beams and acoustic waves since the material responds macroscopically as a coherent whole, even in amorphous media. In particular, Brillouin scattering has a preferred backscattering direction as shown later based on the momentum vector representation of the process.

2.3.2.1 Dispersion Curve

A more accurate quantum-mechanical description of Raman and Brillouin scattering in terms of Stokes and Anti-Stokes scattered waves is necessary to properly characterize their properties. To quantify these scattering effects, the dispersion relationship in the material must be known. The characteristic dispersion equation for a diatomic (SiO_2) linear chain is

$$\omega^2 = \frac{K}{M_1 M_2}\left(M_1 + M_2 \pm \sqrt{M_1 + M_2 + 2M_1 M_2 \cos ka}\right) \tag{2.8}$$

where K represents the strength of the force between adjacent atoms, and M_1, M_2 are their corresponding masses [Ashcroft and Mermin 1976]. The positive and negative signs represent the optical and acoustic branches plotted in Figure 2.2. For Brillouin scattering, the acoustic branch describes the behaviour of the propagating sound wave within the fibre. Although silica glass is amorphous, the material will maintain short-range crystalline order well within the first Brillouin zone where the dispersion curve is linear. In particular, within the first Brillouin zone, the acoustic branch has a dispersion relation of the form $\omega = V_a k$ characteristic of sound waves when $k << \pi/a$, where a is the displacement between adjacent ions. In the Brillouin scattering process considered here, this linear relation holds true.

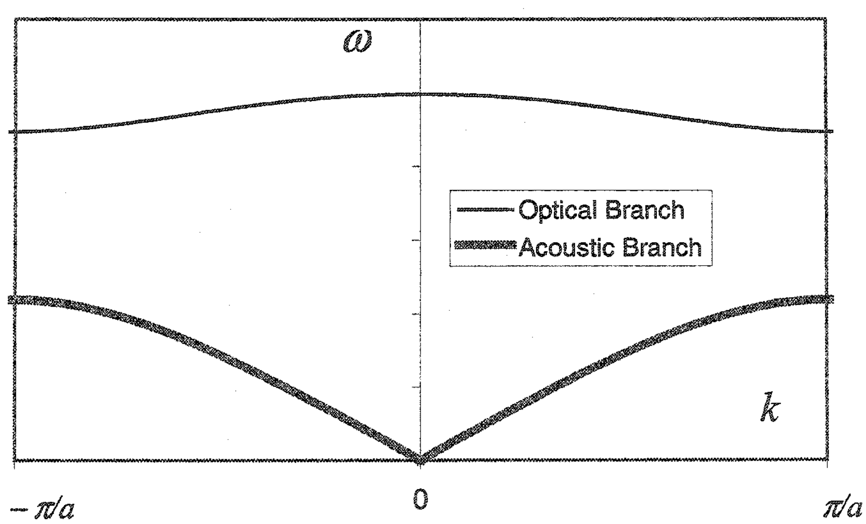

Figure 2.2: Optical (top curve) and acoustic (bottom curve) branches within the first Brillouin zone, $k \in [-\pi/a, \pi/a]$.

2.3.2.2 Stokes and Anti-Stokes Scattering

The interaction of light with a material follows the laws of energy and momentum conservation. Therefore, the scattering of incident light from the material occurs at an angle dependent on the direction of the resulting acoustic vibration or wave, and the corresponding energy (E) and momentum (p) conservation relationships are

$$E_p = E_s \pm E_a, \qquad p_p = p_s \pm p_a, \tag{2.9}$$

where the plus and minus signs describe the Stokes and Anti-Stokes processes whereby the resulting scattered light is frequency down-shifted or up-shifted respectively. The subscripts correspond to the pump, Stokes (or Anti-Stokes), and acoustic waves.

In both Stokes and Anti-Stokes scattering (Figure 2.3), a molecule is excited into a higher virtual energy state for a short lifetime given by $\Delta T \approx h/\Delta\varepsilon$, where $\Delta\varepsilon$ is the energy difference between the virtual and real energy levels. After spending ΔT in the virtual energy state, the molecule subsequently drops to a lower energy level, resulting in the emission of a lower (Stokes) or higher (Anti-Stokes) energy photon. In the case of Stokes scattering, the molecule elevates into a higher energy state whereas in Anti-Stokes scattering, the molecule gives energy to generate the higher energy photon.

Dividing Equations 2.9 by $\hbar$ yields analogous relationships for frequency and wavenumber given as

$$\omega_p = \omega_s \pm \omega_a, \qquad k_p = k_s \pm k_a \tag{2.10}$$

Since momentum conservation must occur in magnitude and direction, the momentum vector diagram of the process shown in Figure 2.4 must be satisfied. Following Pythagorean's theorem and the law of cosines, the equations describing Figure 2.4 are given respectively as

$$k_p^{\ 2} - k_s^{\ 2} + 2k_s\delta = k_a^{\ 2} \tag{2.11}$$

$$\delta = k_s - k_p \cos\theta \tag{2.12}$$

Combining Equations 2.11 and 2.12 yields

$$k_p^{\ 2} + k_s^{\ 2} - 2k_s k_p + 4k_s k_p \sin^2(\theta/2) = k_a^{\ 2} \tag{2.13}$$

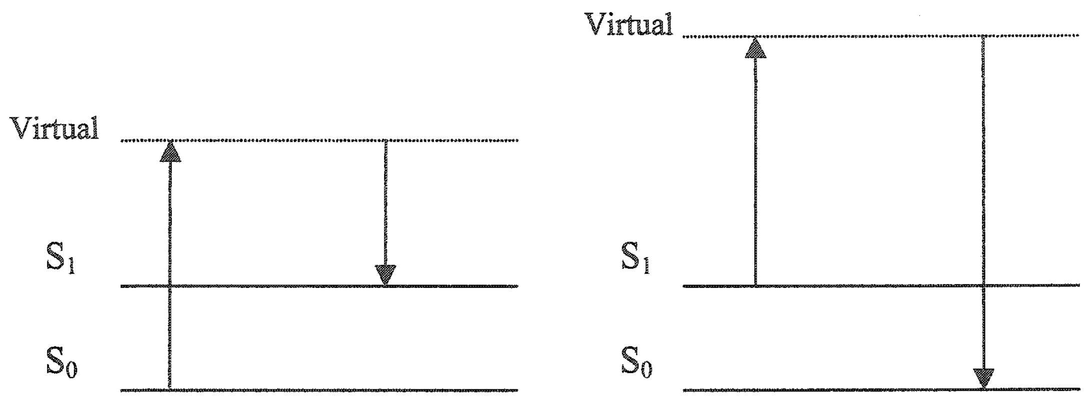

(a) Stokes (b) Anti-Stokes

Figure 2.3: Energy level diagrams illustrating the Stokes (a) and Anti-Stokes (b) processes. The ground and excited states are S_0 and S_1 respectively.

Since $k << \pi/a$, the scattering process has a linear dispersion relationship given by $\omega = 2\pi v = V_a k$, where V_a is the acoustic velocity. In addition, the pump and Stokes frequencies are approximately equal (i.e. $c >> V_a \rightarrow k_p \cong k_s$). Therefore, the Brillouin frequency is written as

$$v_B = \frac{2nV_a}{\lambda_p} \sin\frac{\theta}{2}, \tag{2.14}$$

where n and λ_p are the refractive index and pump wavelength respectively, whereas θ represents the angle between the incident and scattered light beams. Therefore, within the confined geometry of silica fibres, the maximum Brillouin frequency occurs when $\theta = \pi$ (backscattered) and is given by

$$v_B = \frac{2nV_a}{\lambda_p}. \tag{2.15}$$

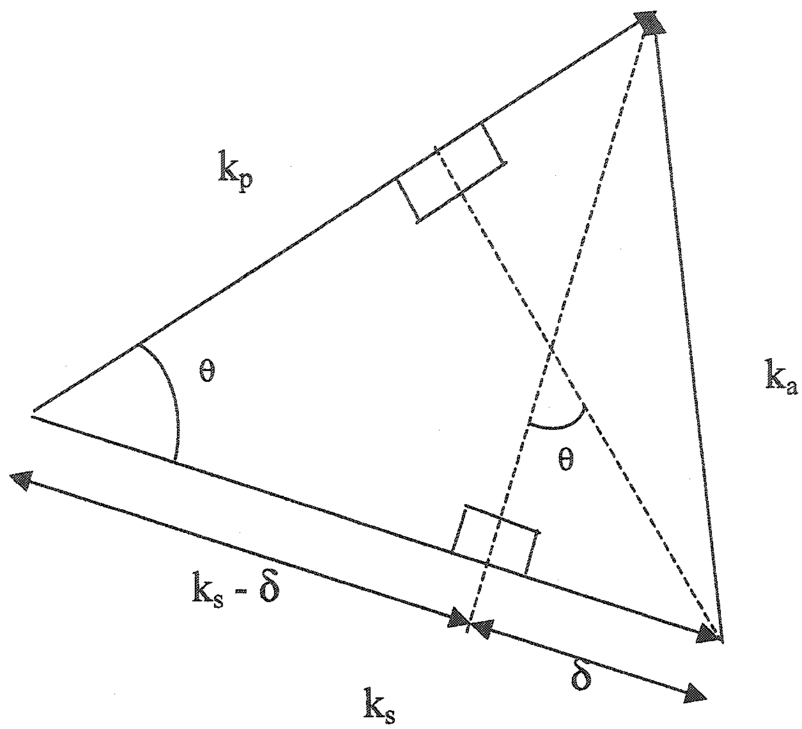

Figure 2.4: Vectorial representation of the Stokes interaction of the pump (k_p), Stokes (k_s), and acoustic (k_a) waves. Here, $k_p = k_s + k_a$. Conversely, the Anti-Stokes diagram would have the arrowhead of k_a pointing downward.

For a 1.319 μm pump wavelength, 1.4675 refractive index [Corning 1998], and 5750 m/s acoustic velocity [Smith 1999], the Brillouin frequency of silica fibre at room temperature is approximately 12800 MHz. As a material property, the Brillouin frequency has a direct linear relationship with strain and temperature given by

$$\nu_B = \nu_{B0} + C_T(T - T_0) + C_\varepsilon(\varepsilon - \varepsilon_0), \tag{2.16}$$

where T_0 and ε_0 are the temperature and strain corresponding to a reference Brillouin frequency ν_{B0}. The temperature and strain coefficients, C_T and C_ε, are material properties representing the temperature- and strain-frequency slopes. Since no two separate fibres are structurally identical, determination of these coefficients through appropriate laboratory temperature and strain calibrations is required. Ultimately, this linear relationship (Equation

2.16) makes Brillouin scattering a simple and powerful technique for temperature and strain sensing.

2.4 Three Coupled Differential Equations

The electrostrictive coupling of counter-propagating pump and Stokes optical fields is governed by Maxwell's equations (Equations 2.17a and 2.17b), while the acoustic field is described by the Navier-Stokes equation given by Equation 2.17c [Kaiser and Maier 1972, Valley 1986, Afshaarvahid and Munch 2001].

$$\left(\frac{\partial}{\partial z}-\frac{n}{c}\frac{\partial}{\partial t}\right)E_p = ig_1 Q E_s - \frac{1}{2}\alpha E_p, \tag{2.17a}$$

$$\left(\frac{\partial}{\partial z}+\frac{n}{c}\frac{\partial}{\partial t}\right)E_s = -ig_1 Q^* E_p + \frac{1}{2}\alpha E_s, \tag{2.17b}$$

$$\left(\frac{\partial}{\partial t}+\Gamma\right)Q = -ig_2 E_p E_s^* + f. \tag{2.17c}$$

The pump, Stokes, and acoustic fields are E_p, E_s, and Q respectively, f is the Langevin thermal noise term (see section 2.6), and the coupling coefficients, g_1 and g_2, are related to the Brillouin gain coefficient through $g_B = 2g_1 g_2 / \Gamma_1$, where $\Gamma_1 = 1/2\tau$ and τ is the phonon lifetime. In the absence of a driving force, Equation 2.17c reduces to

$$\left(\frac{\partial}{\partial t}+\Gamma\right)Q = 0 \tag{2.18}$$

Since the complex detuning parameter is given by $\Gamma = \Gamma_1 + i\Gamma_2$, where $\Gamma_2 = 2\pi(\nu - \nu_B)$ and ν is the beat frequency of the pump and Stokes beams, integration of Equation 2.18 yields the acoustic wave intensity as

$$I = QQ^* = Q_0^{\,2} e^{-2\Gamma_1 t} = Q_0^{\,2} e^{-t/\tau}, \tag{2.19}$$

where Q_0 is the acoustic field amplitude. Essentially, in the absence of a driving force, the phonon lifetime (~ 10 ns for silica fibre) indicates the rate at which the acoustic wave intensity decays.

In the steady-state regime, where the interaction length exceeds the phonon lifetime, the time derivatives in Equations 2.17 can be neglected to yield two coupled differential equations:

$$\frac{\partial}{\partial z}E_p = \frac{g_1 g_2}{\Gamma}\left|E_s\right|^2 E_p + \frac{1}{2}\alpha E_p \tag{2.20}$$

$$\frac{\partial}{\partial z}E_s = \frac{g_1 g_2}{\Gamma^*}\left|E_p\right|^2 E_s - \frac{1}{2}\alpha E_s \tag{2.21}$$

By realizing that $\frac{\partial}{\partial z}I_p = E_p^* \frac{\partial}{\partial z}E_p + E_p \frac{\partial}{\partial z}E_p^*$, Equations 2.20 and 2.21 can be written in terms of intensities as

$$\frac{\partial}{\partial z}I_p = g_B(\omega) I_s I_p - \alpha I_p \tag{2.22}$$

$$\frac{\partial}{\partial z}I_s = g_B(\omega) I_s I_p + \alpha I_s \tag{2.23}$$

where $g_B(\omega) = g_B \frac{\Gamma_1^2}{\Gamma_1^2 + \Gamma_2^2}$ and $g_B = \frac{2 g_1 g_2}{\Gamma_1}$.

2.5 Brillouin Frequency Spectrum

The previous discussion of Stokes and Anti-Stokes waves emphasized the importance of energy and momentum conservation in obtaining the acoustic wave. However, due to line-broadening mechanisms such as homogeneous (natural) and inhomogeneous (impurities) broadening, this amplification process actually occurs over a distribution of frequencies about the central Brillouin frequency, where the pump-Stokes interaction is greatest. Using the undepleted pump approximation, direct integration of Equations 2.17 expresses the Brillouin frequency spectrum as [Boyd and Rzazewski 1990]

$$S(\omega) = \frac{4h\omega_s(N+1)}{ncA\Gamma_1}\left[\exp\left(\frac{G(\Gamma_1/2)^2}{\omega^2 + (\Gamma_1/2)^2}\right) - 1\right], \tag{2.24}$$

where $G = g_B I_p L$ is the single-pass Brillouin gain factor (i.e. no reflection), ω is the frequency deviation from the Brillouin frequency, N is the mean number of phonons per acoustic field mode, A is the cross sectional area, n is the refractive index, Γ_1 is the spontaneous Brillouin linewidth, and ω_s is the Stokes frequency.

The Brillouin frequency spectrum evolves from a Lorentzian to a Gaussian lineshape and narrows as the input laser intensity increases from the low- to high-gain limits. In the low-gain limit (G<<1), the series expansion, $e^x \approx 1 + x$, approximates the exponential term yielding the Lorentzian Equation 2.25. Equation 2.26, having a Gaussian form, is determined by pulling out $\exp(G)$ and making $\omega^2 << (\Gamma/2)^2$, which occurs in the high-gain limit (G>>1).

$$S(\omega) = \frac{h\omega_s(N+1)G\Gamma_1}{ncA}\frac{1}{\omega^2 + (\Gamma_1/2)^2} \tag{2.25}$$

$$S(\omega) = \frac{4h\omega_s(N+1)}{ncA\Gamma_1}\exp(G)\exp\left(\frac{-4G\omega^2}{\Gamma_1^2}\right) \tag{2.26}$$

For G>>1, the gain-narrowed spectrum has a linewidth (full width at half maximum – FWHM) equal to $\Delta\omega = \Gamma_1\sqrt{\ln 2/G}$. Although the linewidth narrows and approaches zero for large G, the large unaccounted pump depletion eventually yields a minimum non-zero linewidth [Yeniay 2002].

As evidenced in Chapter 4, the Brillouin spectral shape can also change when a pulsed beam experiences Brillouin scattering, especially when the interaction length is shorter than the phonon lifetime.

2.6 Spontaneous Brillouin Scattering

Spontaneous Brillouin scattering occurs when low intensity light scatters off thermal fluctuations (Langevin noise term, f) vibrating in random directions, which initiate a weak backward scattering and can quickly lead to the stimulated Brillouin scattering (SBS) process [Boyd and Rzazewski 1990]. This backscattered Brillouin intensity varies linearly with input pump intensity when operating below the threshold for stimulated Brillouin scattering [Kaiser and Maier 1972]. In this regime, the scattered light does not enhance the thermal noise or acoustic properties. The Brillouin frequency spectrum in this regime assumes a Lorentzian distribution, which is characteristic of a homogeneous process whereby all atoms have a unique vibrational frequency. Hence, the interaction is only limited by a single phonon lifetime of the host material. Silica optical fibres (τ = 10 *ns*) yield a 15.9 MHz ($\Delta\nu = 1/2\pi\tau$) spontaneous Brillouin linewidth from the interaction of a low intensity CW beam when fibre impurities are absent or negligibly affect the interaction [Agrawal 1997].

2.7 Stimulated Brillouin Scattering (SBS)

Stimulated Brillouin scattering (SBS) in single mode optical fibre is characterized by an efficient transfer of optical power from a wave propagating in one direction to a wave in the opposite direction. In particular, the strong interaction of an input pump wave with its inelastically scattered counterpart generates a refractive index grating along the fibre core through the process of electrostriction, which will be explained shortly. For a pump-Stokes interaction, the index variation acts like a Bragg grating travelling away from the pump at the acoustic velocity. The backscattered Stokes wave is therefore Doppler shifted to a lower frequency than the forward propagating pump wave.

2.7.1 Electrostriction

When two equally polarized light waves of different optical frequencies counter-propagate in the same electrostrictive material, their superposition yields interference fringes, creating strong and weak electric field intensity zones as shown in Figure 2.5. When the frequency of interference fringes matches the Brillouin frequency, the optical field exerts a strong torque on the electric dipoles not already aligned with the field (Figures 2.6a and 2.6b). This rotation forces an atomic reorientation, and movement along the field propagation direction toward regions of high electric field. Since the input field amplitude varies periodically at the acoustic wavelength, it will also generate high and low atomic density regions. This occurs because the electric fields acting on adjacent dipoles are not identical, and thus yield different electrostrictive pressures through [Boyd 1992]

$$p_{st} = -\rho \frac{\partial \varepsilon}{\partial \rho} \frac{E^2}{8\pi} = -\frac{\gamma_e E^2}{8\pi}, \tag{2.27}$$

where γ_e is the electrostrictive constant and E is the electric field strength. The negative sign indicates a reduced pressure, which allows for an atomic build-up into regions of high electric field (Figure 2.6c). In low-loss optical fibres, electrostriction is the main physical mechanism employed by an optical field to generate a pressure wave, and its impact emerges directly through the Brillouin gain coefficient (as in Equations 2.22, 2.23)

$$g_B(\nu_B) = \frac{\gamma_e^2 \omega^2}{2nc^3 V_A \rho_0 \Gamma_B} \tag{2.28}$$

where ω is the laser frequency, ρ_0 is the unperturbed fibre density, V_A is the acoustic velocity in silica, and Γ_B is the spontaneous Brillouin linewidth. As previously mentioned, the creation and exponential decay of the acoustic pressure wave occurs over approximately 10 ns, the phonon lifetime of silica.

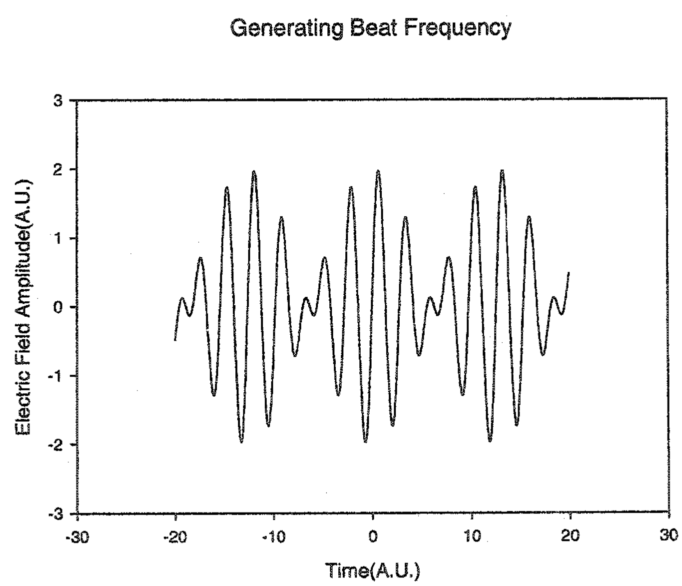

Figure 2.5: Two counter-propagating beams of different frequencies are coupled through an induced acoustic field in the fibre. Subsequent refractive index modulation yields regions of high and low electric field intensity.

2.7.2 SBS Generator and Amplifier

In optical fibres, the SBS amplifier and SBS generator are two configurations commonly used to capture SBS signals. In the SBS generator, a single laser propagates through the fibre whereas the SBS amplifier employs two counter-propagating laser beams for amplification of the scattered light. In the SBS generator configuration, the process of Brillouin scattering begins spontaneously from the existing thermal fluctuations. However, when the product of the pump and Stokes fields, E_pE_S, exceeds the Langevin thermal contribution, f, the electric fields then predominantly drive the amplitude of the acoustic wave Q through Equation 2.17c.

In the SBS amplifier, the existence of a second laser (ν_2) enhances the Stokes scattered light from the first laser (ν_s) when the two frequencies match, i.e. $\nu_2 = \nu_s$. During the Brillouin amplification process, the two lasers have different energies ($E = \hbar\omega$), and thus introduce an energy exchange from the higher to lower energy laser beam. As explained earlier, the Brillouin gain or loss process occurs depending on whether the pump gains or loses energy, and both processes can theoretically be determined by simply changing the sign of g_B (+/- implies Brillouin loss and gain respectively) in the coupled differential equations.

When the input optical intensity of a single laser reaches a critical value, it can single-handedly initiate strong Brillouin scattering by creating strong Stokes waves. Unfortunately, this is an undesirable effect for long-range Brillouin sensors since nearly a full (100% reflectivity) pump-to-Stokes conversion eventually occurs over a short interaction length. Since distributed sensing requires a high Brillouin gain over long sensing lengths (L>>pulse width), the laser power cannot exceed the Brillouin threshold power [Smith 1972]

$$P_{th} = \frac{21A_{eff}}{g_B(\nu_B)L_{eff}}\left(1+\frac{\Delta\nu_P}{\Delta\nu_B}\right), \tag{2.29}$$

where A_{eff} is the effective core area, $g_B(\nu_B)$ is the Brillouin gain coefficient (when $\nu = \nu_B$), $\Delta\nu_p$ and $\Delta\nu_B$ are the laser and Brillouin linewidths, and the effective length is $L_{eff} = \left(1+e^{-\alpha L}\right)/\alpha$ (for a pulse: $L_{eff} = c\tau/2n$) where L and α are the fibre length and attenuation rate, respectively. Since $\Delta\nu_p << \Delta\nu_B$ in most Brillouin scattering experiments, the second term in Equation 2.29 is often ignored.

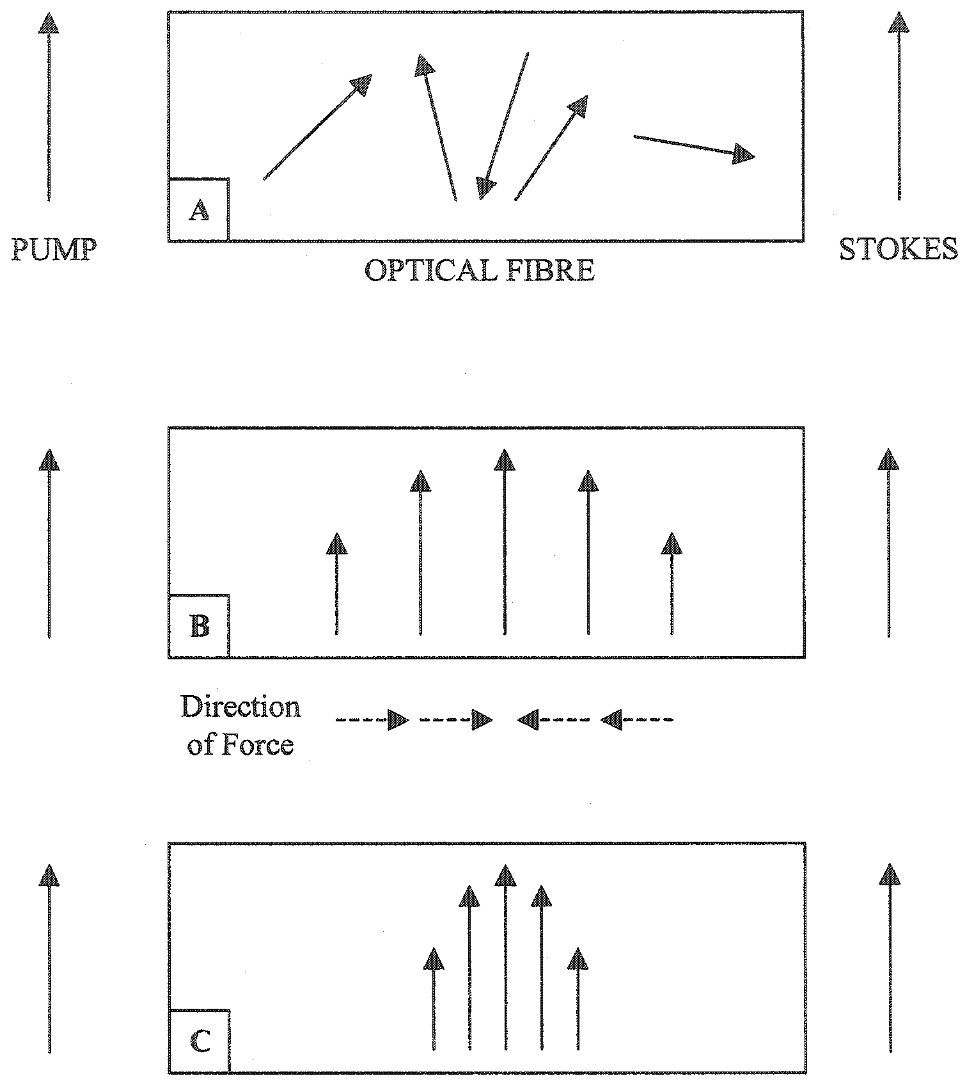

Figure 2.6: Electrostriction process in optical fibre. Before delivering counter-propagating pump and Stokes input beams into the fibre, the silica molecules have randomly oriented dipoles according to their amorphous structure (A). When the pump and Stokes waves interfere through an acoustic field, the total electric field intensity varies sinusoidally along the fibre for some instant in time (B) and the electric dipoles align with the field. Therefore, molecules located in regions of weak electric field thus move into regions of maximum electric field (C).

Chapter 3: Brillouin Sensor Configuration - Working Principles

In this chapter, a description of the Brillouin loss scattering apparatus given in Figure 3.1 brings an emphasis to the working principles of the optical subsystem, i.e. the electro-optic modulator, circulator, isolator, and couplers. The system begins with two Nd:YAG ~1319 nm lasers counter-propagating through the optical subsystem. Upon passing through the electro-optic modulator (EOM), the CW probe beam becomes pulsed. Afterward, this pulsed beam enters the 3-port circulator through port A and exits via port B and onward through a 99:1 optical coupler, which allows for optical pulse (1%) monitoring while the remaining light (99%) enters the sensing fibre.

Meanwhile, the CW pump beam passes through an automated polarization controller, which will either scramble or fix the polarization when dealing with single-mode or polarization maintaining fibres respectively. In single-mode fibre, the polarization states, and hence the Brillouin interactions, of the incoming light beams vary randomly at different positions. Therefore, polarization scrambling ensures that an average Brillouin interaction occurs continuously throughout the fibre. However, due to the asymmetric refractive index profile in polarization maintaining fibres, the polarization can be maintained over long fibre lengths when the input polarization is initially fixed along either the slow or fast axis.

Next, a 95:5 coupler splits the pump beam for Brillouin interaction in the sensing fibre (95%) and for monitoring the beat frequency of the two lasers (5%). In the former case, the light enters a variable attenuator, which controls the amount of light allowed into the sensing fibre. The variable attenuator ensures that the Brillouin interaction occurs below the SBS threshold, which varies with fibre length and its Brillouin frequency distributions [Shiraki *et al.* 1996]. Finally, an optical isolator directs the pump beam into the sensing fibre while blocking any counter-propagating light that may destabilize the pump laser.

When the two counter-propagating beams generate Brillouin amplification in the sensing fibre, the Brillouin signal moves through the 99:1 coupler, and then passes through the optical circulator by following a path from port B to port C. A photodetector-amplifier combination then converts the optical signal into an electrical signal and amplifies it before entering the Lecroy LSA 1000 data acquisition system.

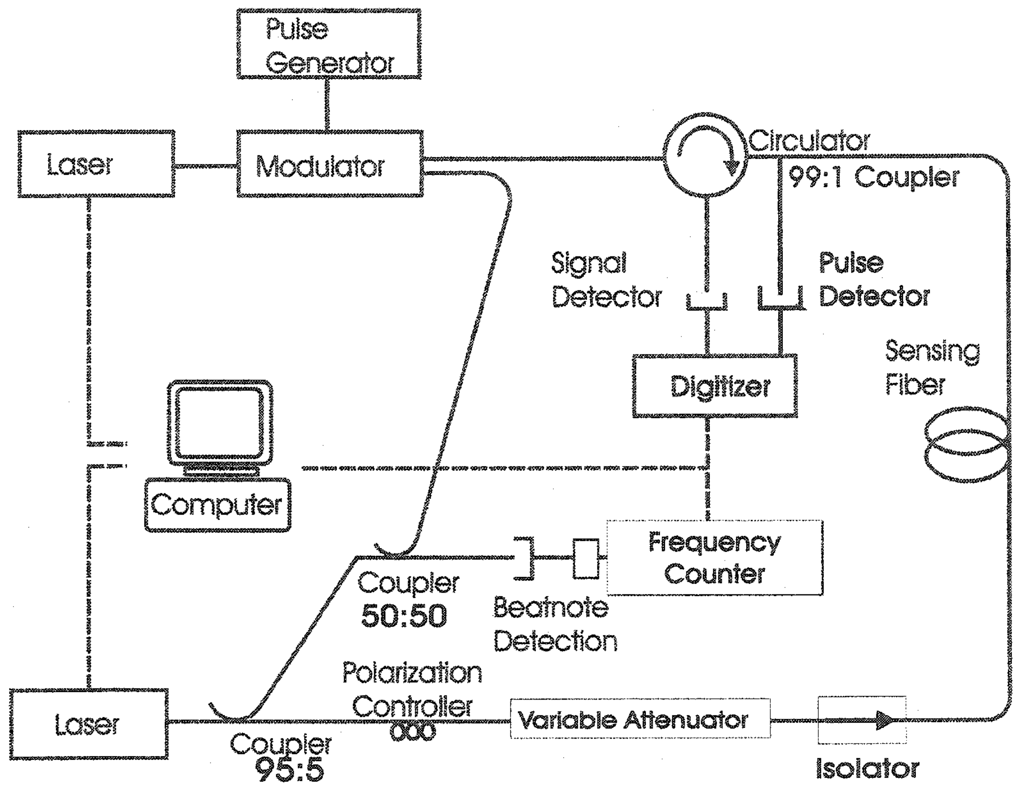

Figure 3.1: Probe-pump distributed Brillouin sensing system configuration. The top and bottom lasers are the probe and pump lasers respectively. After Zeng [Zeng 2003], but modified slightly.

3.1 Electro-Optic Modulator

The electro-optic modulator is an active optical device that achieves amplitude or phase modulation of incoming light by exploiting the electro-optic effect, whereby the application of an electric field alters the optical properties of an electro-optic crystal. The linear electro-optic effect manifests itself in non-centrosymmetric materials such as GaAs (cubic crystal), KDP (tetragonal), and $LiNbO_3$ (trigonal). Since $LiNbO_3$ has a large Pockels coefficient and subsequently diminished requirements on voltage and length, it is the preferred material for electro-optic modulation. In general, the relationship between refractive index change and applied field E is

$$n(E) = n - \frac{1}{2}n^3 rE - \frac{1}{2}n^3 sE^2 + \ldots; \tag{3.1}$$

where n is the original refractive index, and r, s are the relevant linear and quadratic electro-optic tensor elements respectively. Since electro-optic modulators are dominated by the linear electro-optic effect, the second term in Equation 3.1 dictates the refractive index change. Using Equation 3.1, the corresponding phase change, $\Delta\phi$, is then

$$\Delta\phi = \omega\Delta t = \frac{\omega L \Delta n}{c} = \frac{\omega L n^3 rE}{2c} = \frac{\omega n^3 rV}{2c}, \tag{3.2}$$

where $V = EL$ is the applied voltage over an interaction length L, ω is the optical frequency, and c is the speed of light in vacuum.

In our system, the Y-balanced Mach-Zehnder integrated modulator configuration, shown in Figure 3.2, converts a radio frequency (RF) pulse from the electrical to optical domain so it can propagate and collect spatial information along the sensing fibre. Upon entering the Mach-Zehnder interferometer, the CW probe laser signal splits equally (50:50) into the signal and reference arms. By varying their refractive index difference, a phase shift proportional to the applied voltage occurs according to Equation 3.2. Consequently, when this voltage is applied to the signal arm while maintaining an unperturbed reference arm, the relative phase difference produces an output intensity modulation. The two light waves then recombine and split again 50:50 into two outputs differing by a π phase shift (see section 3.2). Generally, the recombined electric field of the light entering output 1 can be written as the sum of the fields arriving from the signal (E_S) and reference (E_R) arms:

$$E = E_S \exp(i(\omega t + \Delta\phi)) + E_R \exp(i\omega t)$$
$$E = \exp(i\omega t)[E_S \exp(i\Delta\phi) + E_R] \tag{3.3}$$

Since the intensity is proportional to the product of E and its conjugate, the intensity is

$$I_1 \propto E_S{}^2 + E_R{}^2 + 2E_S E_R \cos\Delta\phi \tag{3.4}$$

For a perfect 50:50 transmission, $E_R = E_S = E/2$, the intensity is simplified as

$$I_1 \propto \frac{E^2}{2}[1+\cos\Delta\phi], \tag{3.5}$$

where E is the input electric field amplitude. When the phase difference ($\Delta\phi$) between the two arms equals π, the total intensity contribution from the signal and reference beams (i.e. P_{CW}) drops to zero, whereas an intensity minimum (non-zero DC component, see Figure 3.3) given by $I_1 \propto |E_S - E_R|^2$ occurs without perfect 50:50 transmission. Since evanescent coupling between the output arms creates a π phase difference (see section 3.2) between the two output light beams, the light intensity entering output 2 is

$$I_2 \propto E_S^{\ 2} + E_R^{\ 2} + 2E_S E_R \cos(\Delta\phi + \pi)$$

$$I_2 \propto E_S^{\ 2} + E_R^{\ 2} - 2E_S E_R \cos\Delta\phi \tag{3.6}$$

Therefore, for output 2, the maximum ($\Delta\phi = \pi$, plus sign), and minimum ($\Delta\phi = 0$, negative sign) intensities are

$$I_2 \propto E_S^{\ 2} + E_R^{\ 2} \pm 2E_S E_R = (E_S \pm E_R)^2 \tag{3.7}$$

Again, if the signal and reference arm amplitudes are equal and $\Delta\phi = \pi$, all of the input light reaches output 2, i.e. $I_1 = 0$ and $I_2 = E^2$.

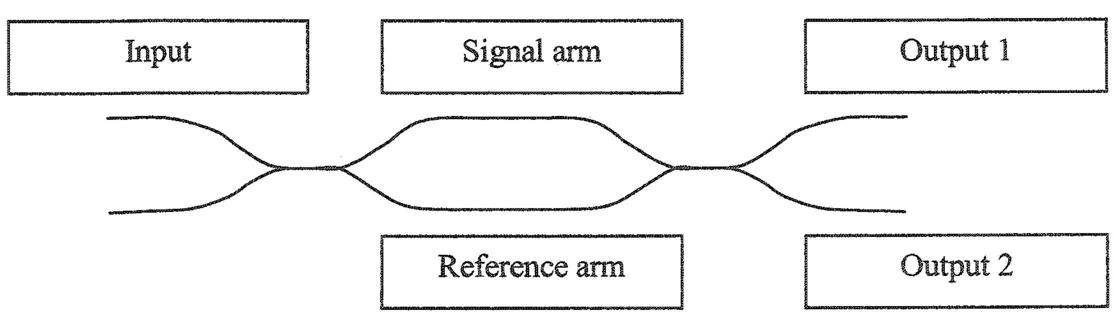

Figure 3.2: Mach-Zehnder interferometer configuration

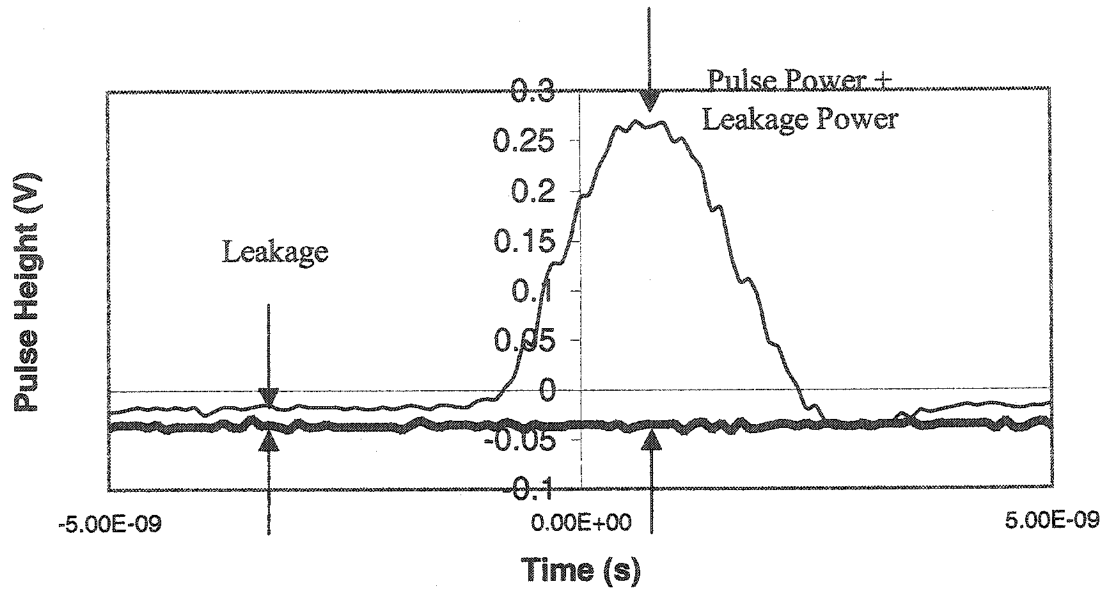

Figure 3.3: An optical Gaussian pulse obtained experimentally revealing both a pulse and CW leakage component (indicated by arrows).

However, due to physical design limitations, an EOM has a finite extinction ratio defined as the ratio of the maximum ($\Delta\phi = 0$) and minimum ($\Delta\phi = \pi$) output optical powers:

$$R_x(dB) = 10\log\left(\frac{P_{pulse} + P_{CW}}{P_{CW}}\right) \tag{3.8}$$

The logarithmic nature of the decibel unit, *dB*, allows large ratios (1000) to be expressed as much smaller numbers (30 *dB*). As an industry standard, electro-optic modulators typically exhibit maximum finite extinction ratios between 25-30 *dB* (when $\Delta\phi = \pi$). Consequently, P_{CW} is never exactly zero for a few reasons. First, the splitting ratio of the input light entering the Mach-Zehnder interferometer must theoretically be 50:50 as shown above. However, due to losses associated with light coupling, an exact 50:50 splitting ratio cannot be obtained. Second, it is difficult to obtain an exact π phase difference between the splitting arms since the modulator arms can experience thermal fluctuations. As previously mentioned, an input (bias) voltage controls the path (phase) difference. If this voltage is not precisely V_π (Figure 3.4), then P_{CW} cannot be zero. Finally, the polarizations of the beams entering the signal and reference arms must be equal to avoid phase changes resulting from birefringence.

As shown in Figure 3.4, optical pulse generation is achieved by temporarily applying a driving radio frequency (RF) pulse with an electric field amplitude *E* such that the refractive indices of the signal and reference arms yield an output exhibiting constructive interference for a duration τ.

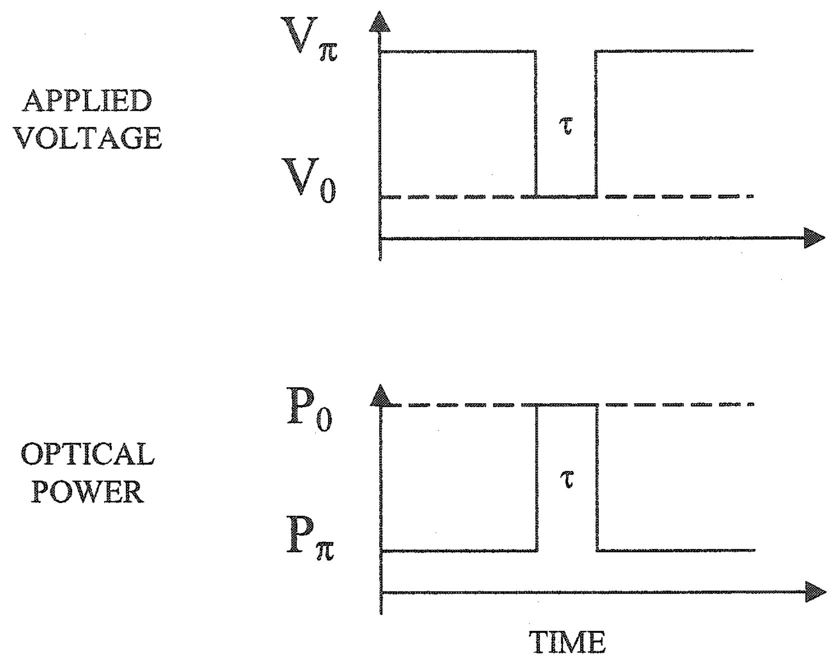

Figure 3.4: Applied voltage and optical power versus time. An applied voltage V_π generates a π phase difference between the signal and reference arms, and thus a minimum power P_π. Conversely, a voltage V_0 generating a zero phase difference allows for a maximum power transmission given by P_0. Thus, optical pulse generation occurs during the application of the applied voltage V_0 over a pulse duration τ.

3.2 Directional Coupling

In the electro-optic modulator configuration shown in Figure 3.2, there are two 2x2 directional couplers, which channel the incoming light into and out of the Mach-Zehnder interferometer. To understand how directional couplers operate, a basic understanding of coupled mode theory is required. The following interpretation follows that of Lee and Yariv

[Lee 1986, Yariv 1989]. As shown in the integrated optical coupler illustrated in Figure 3.5, the input power enters the coupler configuration and is shared between the two fibre cores when they are brought into close proximity.

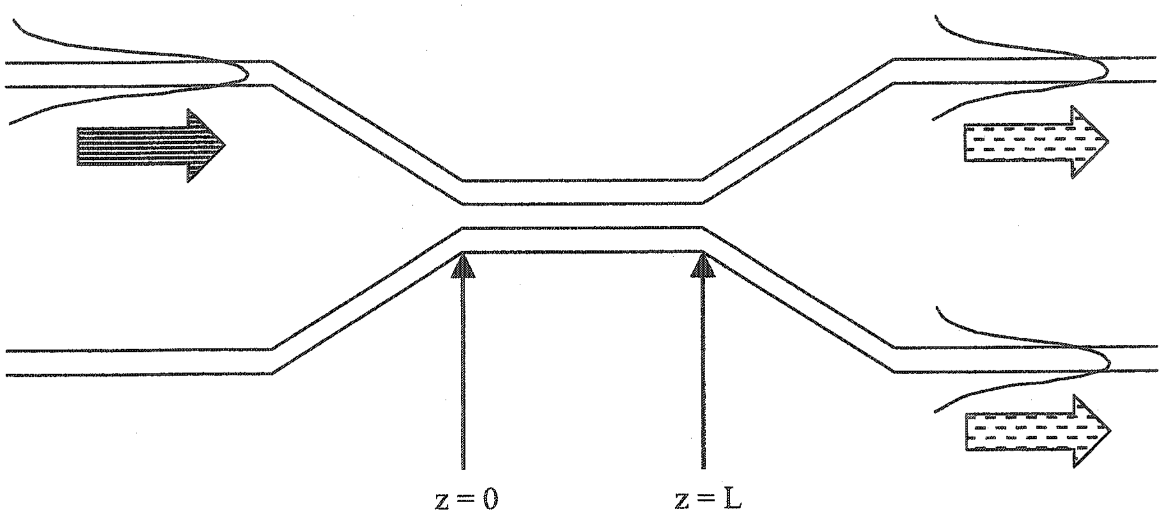

Figure 3.5: The amount of light propagating through either core is dependent on the coupling fibre length. Directional couplers have specified coupling ratios (e.g. 50:50, 90:10...) achieved by modifying either the coupling length or changing the fibre core separation.

Within each fibre cross section, the radial electric field distribution $F(x,y)$ resembles a Gaussian profile described by

$$F(x,y) = F_0 \exp\left(-\frac{x^2+y^2}{2{r_0}^2}\right) = F_0 \exp\left(-\frac{r^2}{2{r_0}^2}\right) \tag{3.9}$$

where r_0 is the mode-field radius representing the effective distribution region. While the majority of the field is concentrated in the core region, a smaller amount (~10-20%) propagates in the outer fibre cladding region. The cladding field distribution decays exponentially away from the core for a sufficiently large radial coordinate and ultimately comprises the evanescent field of the fibre. When two fibre cores are within a few wavelengths of one another, the evanescent field from one fibre may travel into the adjacent core. This results in a power transfer between the two cores, which depends on their alignment, symmetry, interaction length, and relative optical properties. The coupled mode equations describing the electric field amplitudes in both fibre cores for a given propagation length z are given as

$$\frac{d}{dz}A_1(z) = i(\beta_1 A_1(z) + \kappa_{12}A_2(z)) \tag{3.10a}$$

$$\frac{d}{dz}A_2(z) = i(\kappa_{21}A_1(z) + \beta_2 A_2(z)) \tag{3.10b}$$

where β_m and κ_{mn} are the propagation and coupling constants of the fibre cores respectively, and A_m is the electric field amplitude within the m^{th} core after a coupling length z. The radial field (Equation 3.9) is included through $A(z)$ and has an amplitude normalized to unity. Through matrix methods, and knowing that $P_i(z) = |A_i(z)|^2$, the power in each waveguide can be determined as

$$P_1(z) = P_0 \frac{|\kappa_{21}|^2}{S^2} \sin^2(Sz) \tag{3.11}$$

$$P_2(z) = P_0 \left[\left(\frac{\Delta k}{2S} \right)^2 \sin^2(Sz) + \cos^2(Sz) \right] \tag{3.12}$$

where

$$S = \sqrt{\left(\frac{\Delta k}{2} \right)^2 + \kappa_{21}\kappa_{12}} \; ; \qquad \Delta k = \beta_2 - \beta_1 \,.$$

For phase matched waveguides, $\Delta k = 0$ and $\kappa_{21} = \kappa_{12} = \kappa$, Equations 3.11 and 3.12 are simplified as

$$P_1(z) = P_0 \sin^2(\kappa z), \tag{3.13}$$

$$P_2(z) = P_0 \cos^2(\kappa z). \tag{3.14}$$

Phase matched fibre cores provide ideal forward wave coupling by allowing a full power transfer from one fibre to another over a specific coupling length. When the cores are not phase matched, the maximum power transfer is a smaller fraction of the input power dependent on the degree of phase mismatch Δk.

The phase difference between the modes describing the power oscillation between the two fibre cores, known as super-modes γ^+ and γ^-, after a given coupling length L is given by $\Phi = (\gamma^+ - \gamma^-)L = 2S$. For the case of phase-matched fibre cores, a 50:50 splitting ratio occurs when $\Phi = \pi/2$, i.e. $L = \pi/4\kappa$ and $P_1 = P_2 = \frac{1}{2}P_0$. Hence, since the electro-optic modulator described earlier uses two 50:50 couplers, the net phase difference between its output arms is $\Phi = \pi/2 + \pi/2 = \pi$.

3.3 Optical Isolator

Two types of passive optical devices designed to route optical signals for single or multiple functioning are optical isolators and circulators. Both devices manipulate the light polarization using light filtering polarizers, and devices such as Faraday rotators and waveplates, which rotate the light polarization. In this way, the light intensity propagating in particular directions can be completely transmitted or blocked. The intensity of light exiting a polarizer follows the Law of Malus given by

$$I_{out} = I_{in} \cos^2 \theta , \tag{3.15}$$

where θ is the angle between the polarizer and the polarization angle of the incoming light I_{in}. When the polarizer alignment is parallel to the input light, 100% of the light passes through whereas 0% passes through a perpendicularly ($\theta = \pi/2$) aligned polarizer. The optical isolator makes use of the Law of Malus while employing a Faraday rotator, which rotates the light polarization +45° regardless of the direction of light propagation as shown in Figure 3.6. Vertically polarized light entering the optical isolator will be fully transmitted through vertically aligned "polarizer 1" followed by a +45° polarization rotation by the Faraday rotator, allowing for full light transmission through an end "polarizer 2" aligned at +45°. However, when light enters the isolator from the right side, the polarization components aligned with "polarizer 2" pass through and experience an additional +45° rotation from the Faraday rotator making horizontally polarized light. When this light encounters vertical "polarizer 1", no light will pass through based on Malus' Law. Consequently, the optical isolator allows only unidirectional light propagation, and in typical optical applications, prevents laser destabilization by blocking counter-propagating light originating from reflections or other laser sources.

As a key component in the optical isolator, the Faraday rotator operates based on the Faraday effect. Essentially, under an applied magnetic field, a material becomes optically active and rotates the polarization of parallel incident light by an amount

$$\theta = VBL, \tag{3.16}$$

where B and L are the static magnetic field and interaction length, and V is the Verdet constant. In optical isolators, materials with high Verdet constants such as yttrium-iron-garnet (YIG), terbium-gallium-garnet (TGG), and terbium-aluminum-garnet (TbAlG) crystals are capable of rotating the incident polarization by 45° since the subsequent design requirements for magnetic field and length are reduced. Since the rotation direction depends solely on the magnetic field direction, the Faraday effect has a non-reciprocal nature, i.e. the polarization rotates in the same direction regardless of the input light propagation direction through the crystal.

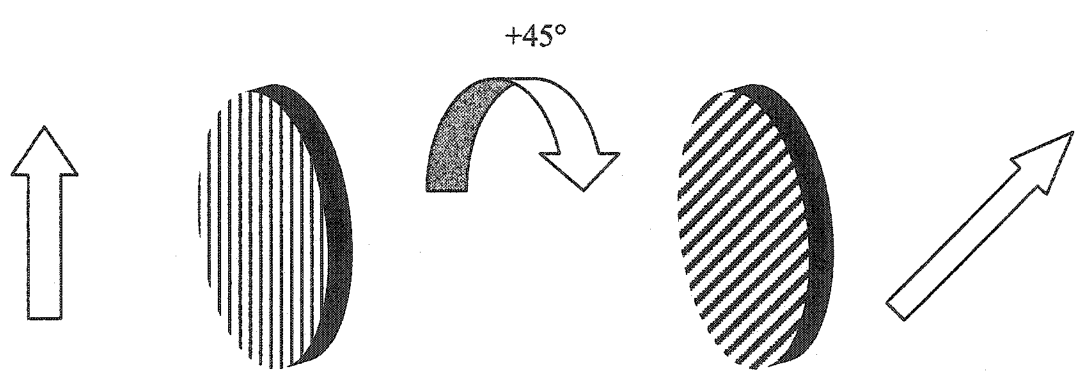

Figure 3.6: Working principle of the isolator [Hecht 1999]. Full transmission of light arriving from the left side occurs whereas light arriving from the right side is completely blocked.

3.4 Optical Circulator

As a more efficient alternative to optical couplers, the 3-port optical circulator shown in Figure 3.7 is designed to allow light transfer from two inputs into two separate outputs for optical multitasking. The design is somewhat more complex as additional waveplates are required for direction-dependent 45° polarization rotation. Unlike Faraday rotators, waveplates provide +45° or -45° rotations depending on whether the light propagates or counter-propagates through the waveplate. In addition, anisotropic birefringent materials (beam displacers) are used to separate the light beam into two perpendicularly polarized light rays known as the ordinary (O) and extraordinary (E) rays.

The input light beam entering port A encounters a beam displacer, which separates the beam into horizontally and vertically polarized beams that become directed, via separate waveplate-Faraday rotator tandems, through the second beam displacer. The horizontally and vertically polarized beams are denoted by dark circles and double-ended arrows respectively. Clearly, the -45°/+45° and +45°/+45° tandems generate 0° and 90° polarization rotations respectively. By rotating the polarization from horizontally to vertically polarized light, the resultant extraordinary beam is capable of bending through the anisotropic material toward the appropriate port.

In our system, the 3-port optical circulator routes light to its appropriate function, as shown in Figure 3.1. The light entering port A exits from port B for Brillouin interaction in the sensing fibre. The counter-propagating Brillouin signal then enters port B and exits from port C toward the detection unit for analysis. In this way, the circulator protects the EOM and probe laser by preventing output intensity from port A and utilizes the total light intensity very efficiently compared with optical couplers. Indeed, optical couplers do not exhibit the same protective measures and, depending on the coupling ratio, waste available light through unused ends.

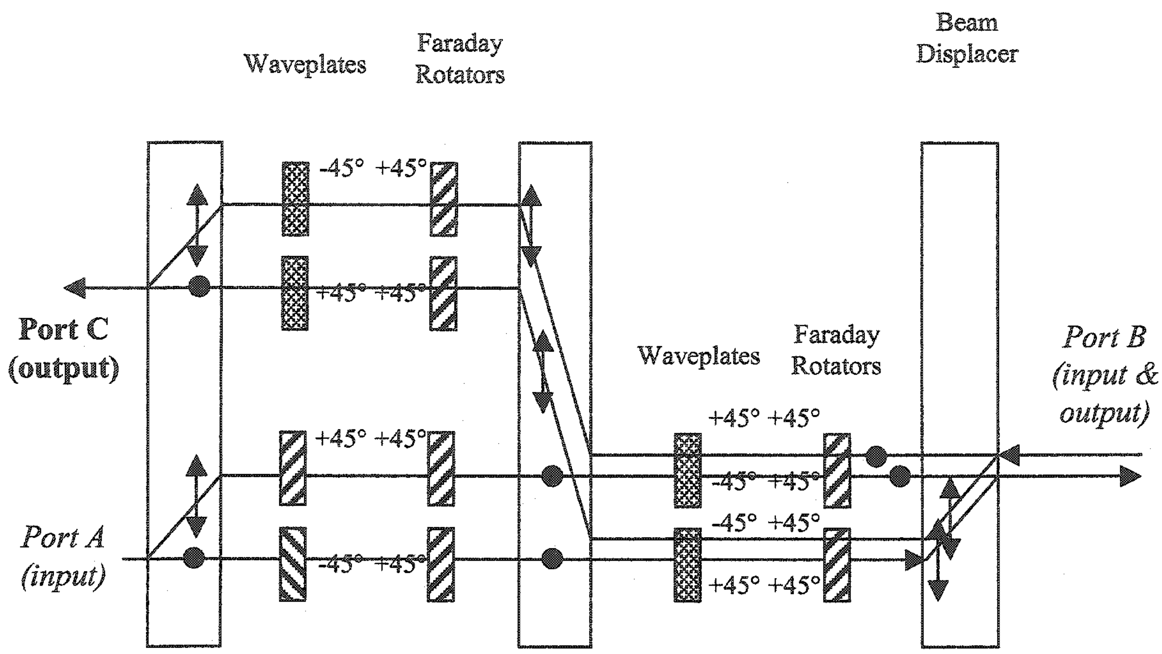

Figure 3.7: Working principle of the circulator. [Sugimoto *et al.* 1999] Light arriving from Port A exits through Port B, while light entering Port B exits through Port C.

Chapter 4: Brillouin Spectral Characterization

This chapter presents a spectral characterization of transient Brillouin scattering in optical fibres obtained from the probe-pump technique. Indeed, new experimental evidence shown here illustrates that the Brillouin spectrum exhibits a distinctly two-fold structure due to continuous wave and short-pulsed beam interactions. In addition, the employment of BOTDA for Brillouin intensity acquisition yields undesirable frequency cross talk, originating from different fibre sections, when interacting CW light waves continuously pump the phonon field. Hence, based on experimental and theoretical investigations, physical explanations of the two-fold profile structure and frequency cross talk will be given.

4.1 Introduction

Brillouin scattering based distributed fibre sensors employing the probe-pump approach have been extensively studied over the past decade due to their enhanced sensitivity to physical parameters such as strain and temperature combined with significant advantages in sensing length and spatial resolution [Bao *et al.* 1995, Brown *et al.* 1999]. Temperature and strain are determined through simple linear relationships (Equation 2.16) with the measured Brillouin frequency of an optical fibre when a maximum energy exchange occurs between two counter-propagating laser beams [Kurashima *et al.* 1990]. However, due to line-broadening mechanisms such as homogeneous (natural) and inhomogeneous (impurities) broadening, this amplification process occurs over a distribution of frequencies about the central Brillouin frequency.

Although many experimental techniques have been developed to measure temperature and/or strain in optical fibres using Brillouin scattering [Horiguchi *et al.* 1990, Bao *et al.* 1993b, Niklès *et al.* 1997], this chapter refers to the probe-pump configuration where an optical pulse gathers spatial information through Brillouin optical time domain analysis (BOTDA). In this configuration, the probe and pump beams counter-propagate in an optical fibre and through their interaction, the resulting acoustic signal amplifies via a mutual energy exchange between the two laser beams. In the Brillouin loss [Bao *et al.* 1993b] method used here, the probe beam (ν_1) amplifies at the expense of the pump beam ($\nu_2 > \nu_1$). By scanning the probe frequency ν_1 over a range of frequencies and measuring the intensity of the corresponding signal at the detector, a Brillouin loss spectral profile is obtained using the configuration shown in Figure 3.1. By fitting an appropriate function to this profile and finding the amount of shift in its resonance frequency with respect to a reference condition, one can determine temperature or strain variations. However, to find an appropriate fitting function that matches the Brillouin profile shape, it is necessary to understand the physical process behind this phenomenon.

As described in section 3.1, optical pulses are generated using an electro-optic modulator (EOM) with a Mach-Zehnder configuration (Figure 3.2), which controls the probe power output to the sensing fibre by varying the path difference between the reference and signal arms. However, even when a π phase difference exists between the two arms, the recombined field always contains a pulse and a small continuous wave (CW) component due to the imbalance of the field amplitudes. Therefore, the EOM always maintains a finite extinction ratio defined as

$$R_x = \frac{P_{pulse} + P_{leakage}}{P_{leakage}} \tag{4.1}$$

where $P_{leakage}$ and P_{pulse} are the leakage and pulse powers respectively. Hence, the Brillouin scattering process of probe-pump interaction consists of leakage-pump (CW-CW) and pulse-pump (pulse-CW) contributions.

Over the years, the Brillouin CW-CW and pulse-CW interactions have been studied separately and the corresponding steady state equations have been derived to predict the energy exchange as a function of length [Tang 1966, Bao *et al.* 1995]. The corresponding Brillouin frequency spectrum has been well documented to have a narrow (~10-100 MHz) Lorentzian shape since the interaction is mainly limited by the phonon lifetime of the material [Agrawal 1997]. Studies of the pulse-CW interaction have shown that the final Brillouin loss profile is determined by the correlation of Brillouin gain $g_B(\nu)$ [Fellay *et al.* 1997], which has a Lorentzian shape, and the frequency spectrum of the pulse.

As evidenced in Figures 4.1 a) and b), short Gaussian (and super-Gaussian – almost square) pulses ($\tau_{pulse} < \tau_{phonon} = 10ns$) yield broad Brillouin loss profiles dominated by their corresponding frequency spectra [Smith *et al.* 1999b, Naruse and Tateda 1999]. The corresponding Fourier transforms of the Gaussian ($f(t) = e^{-4\ln 2(t/\tau)^2}$) and square pulses ($f(t) = 1;\ \ -\tau/2 \le t \le \tau/2$) are:

$$F(\omega) = \sqrt{\frac{1}{2a}} e^{-\omega^2/4a}; \quad a = -4\ln 2/\tau^2 ,$$

$$F(\omega) = \sqrt{\frac{2}{\pi}} \frac{\sin(\omega\tau/2)}{\omega} .$$

However, wide pulses ($\tau_{pulse} > \tau_{phonon} = 10ns$) generate Brillouin loss profiles dominated by the Brillouin gain $g_B(\nu)$. Consequently, Brillouin sensors based on the pulse-CW interaction achieve maximum strain and temperature accuracy only when the pulse width exceeds the phonon lifetime. Hence, it was generally believed that sub-meter spatial resolutions were unachievable in pulse-CW based systems due to rapid linewidth increases when $\tau_{pulse} < \tau_{phonon} = 10ns = 1m$.

Nevertheless, experimental results reported by Bao *et al.* showed, for the first time, that sub-meter resolutions were achievable [Bao *et al.* 1999]. As shown in Figure 4.2, the Brillouin linewidth increased initially but then dropped when the pulse width fell below the phonon lifetime. This behaviour has been attributed to the finite extinction ratio ($P_{leakage} \neq 0$) of the electro-optic modulator (EOM) [Lecoeuche 2000]. However, to fully understand this phenomenon, one must also consider the overall Brillouin spectral shape variations associated with having both pulse-CW and CW-CW Brillouin interactions in the overall process, especially when using short pulses (< 5 ns).

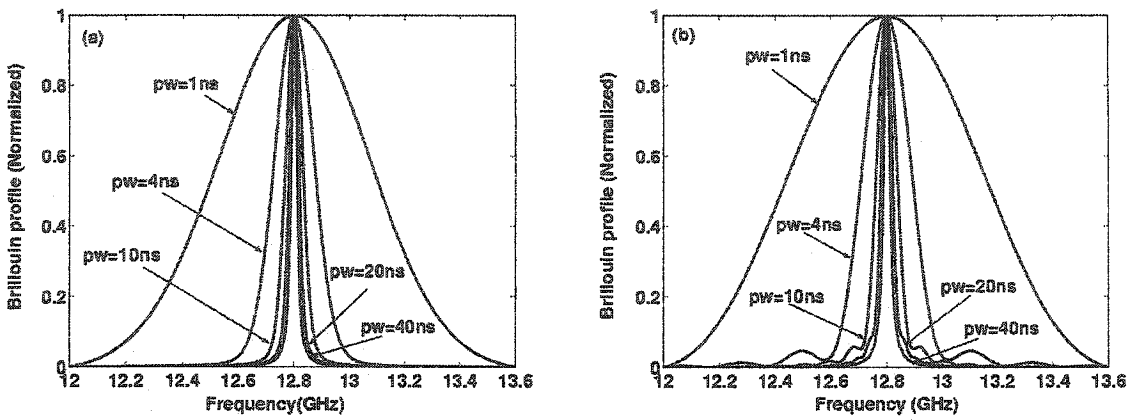

Figure 4.1: Theoretical Brillouin spectral profiles for (a) a Gaussian input pulse and (b) a super-Gaussian input pulse, of different pulse widths. These profiles resemble the frequency spectrum of the input pulse or Brillouin gain $g_B(\nu)$ for short and long pulse widths, respectively.

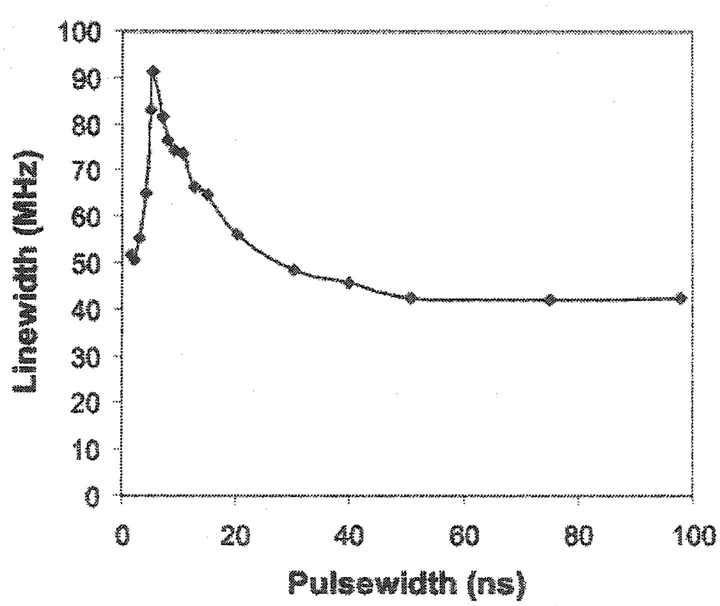

Figure 4.2: Experimental plot of linewidth vs. pulse width revealing a sudden drop in linewidth for pulse widths shorter than 10 ns [Bao *et al.* 1999].

4.2 Brillouin Profile Shape

To investigate the individual contributions from pulse-CW and CW-CW interactions, a simulation model of distributed Brillouin sensors [Afshar *et al.* 2003a and 2003b] was developed based on numerical SBS models developed by Afshaarvahid *et al.* [Afshaarvahid *et al.* 1998, Afshaarvahid and Munch 2001] in which Equations 2.17 are solved numerically. In this chapter, the theoretical plots use the modelling parameters given as follows: $g_B = 5\times10^{-3}\ cm/MW$, τ_{phonon} = 10 ns, d = 9 μm, τ_{pulse} = 1 ns, L = 6 m, P_{pump} = 5 mW, and P_{pulse} = 2 mW, where τ_{phonon} is the phonon lifetime, d is the fibre core diameter, and τ_{pulse} is the pulse width. The input probe beam is a super-Gaussian pulse plus a CW leakage component.

When the Brillouin interaction consists of pulse- and leakage-pump interactions, the overall Brillouin profile comprises both Lorentzian CW-CW and Gaussian pulse-CW contributions [Afshar *et al.* 2003a]. In particular, when the pulse width becomes narrower than the phonon lifetime, their relative contributions to the overall Brillouin profile shape are distinctly different. Under such conditions, the overall Brillouin spectral profile resembles a two-fold structure consisting of a broad Gaussian profile and a narrow Lorentzian profile. The strongest interaction ultimately determines the dominant shape and linewidth of the resultant profile.

To demonstrate this two-fold structure, the theoretical Brillouin loss profiles for 1, 4, 10, and 40 ns pulse widths, and ∞, 40, 30, and 25 *dB* extinction ratios are plotted in Figures 4.3 a)-d). For a 1 ns pulse width, the $R_x = \infty$ curve shows a broad Gaussian profile representing the pulse-CW interaction (Figure 4.3a). However, for finite extinction ratios, the overall profile resembles the underlying Gaussian profile ($R_x = \infty$) plus an additional narrow Lorentzian profile on top, which grows with increasing leakage power (decreasing extinction ratio). For extinction ratios less than 25 *dB*, the overwhelming Lorentzian interaction often makes the Gaussian interaction difficult to recognize in the overall process.

Similar behaviour is apparent in Figures 4.3 b)-d) when the pulse widths are increased to 4, 10, and 40 ns. However, the underlying profile, representing the pulse-CW interaction, narrows and approaches a Lorentzian shape when the pulse width exceeds the phonon lifetime (>10 ns). Furthermore, strong pulse-CW interactions occur when using wider pulses having higher energy. Hence, a bigger leakage power is necessary for the leakage-CW interaction to dominate the pulse-CW interaction. The side peaks in Figures 4.3 b) and c) arise from the Fourier components of the square pulse spectrum.

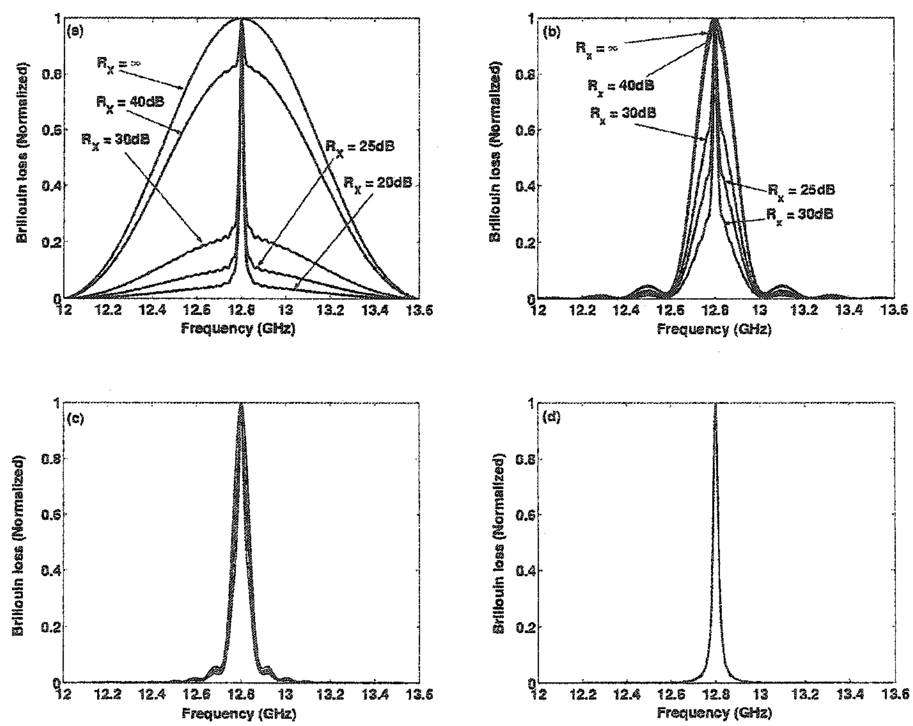

Figure 4.3: Theoretical Brillouin spectral profiles for (a) 1 ns, (b) 4 ns, (c) 10 ns, and (d) 40 ns input pulses with extinction ratios between ∞ and 25 dB (leakage powers are 0.0, 0.0002, 0.002, 0.064 mW respectively). Each profile is normalized to its intensity maximum.

Characterization of this two-fold structure can be achieved by analyzing its evolution as a function of extinction ratio and pulse width, as shown in Figures 4.4 and 4.5 respectively. In both figures, it is immediately apparent that by either increasing the extinction ratio or decreasing the pulse width, a larger fraction of the Brillouin profile assumes that of the Gaussian-shaped pulse. Conversely, when the extinction ratio decreases or pulse width increases, the Brillouin profile more closely resembles the narrow Lorentzian-shaped CW-CW interaction.

The linewidth behaviour of the Brillouin profile as a function of extinction ratio is shown in the normalized curves in Figures 4.4 a)-d). The linewidth evolution from a broad Gaussian to a narrow Lorentzian, when the extinction ratio is decreased, is apparent in all figures. A dramatic linewidth evolution is observed for short pulses (i.e. 1 and 4 ns) since their pulse-CW interactions (yielding broad Gaussian spectra) can be overwhelmed even by weak CW-CW interactions due to the lower energy pulse-CW interaction. Conversely, as the pulse width increases beyond the phonon lifetime in Figures 4.4 c), d), the corresponding Brillouin linewidth exhibits little variation as the extinction ratio is decreased since pulse-CW and CW-CW linewidths and energies are already comparable.

The evolution of the Brillouin profile as a function of pulse width and extinction ratio is shown in the normalized curves in Figures 4.5 a)-d). The corresponding insets reveal that the maximum linewidth decreases and shifts to larger pulse widths as the extinction ratio decreases. Eventually, for small extinction ratios, the linewidth remains constant for all pulse widths. Similar behaviour has been studied both experimentally [Bao *et al.* 1999] (see Figure 4.1) and numerically [Lecoeuche 2000]. However, one should be cautious about those results because a single process cannot fully describe the two-fold structure of the Brillouin loss spectrum.

For example, the plot of linewidth vs. pulse width shown in the inset of Figure 4.5 b) reveals a linewidth maximum of approximately 110 MHz for a 4 ns pulse width. Upon closer examination of the corresponding Brillouin spectrum in Figure 4.5 b), this broadening simply occurs due to a contribution from the Gaussian part of the spectrum. This creates a deceptive interpretation of Brillouin frequency resolution (see Appendix A.5 when $\beta = 1$) since the overall linewidth has normally been assumed to originate from one Lorentzian process, which is clearly not the case here. Indeed, the main practical limitation should arise from the narrow spectral portion near the tip or maximum of the Brillouin spectrum assuming it exceeds the experimental noise level. For example, if the linewidth is taken at 70% rather than at 50% maximum, the spectral widths are basically invariant with changing extinction ratio, as shown in Figure 4.5 b).

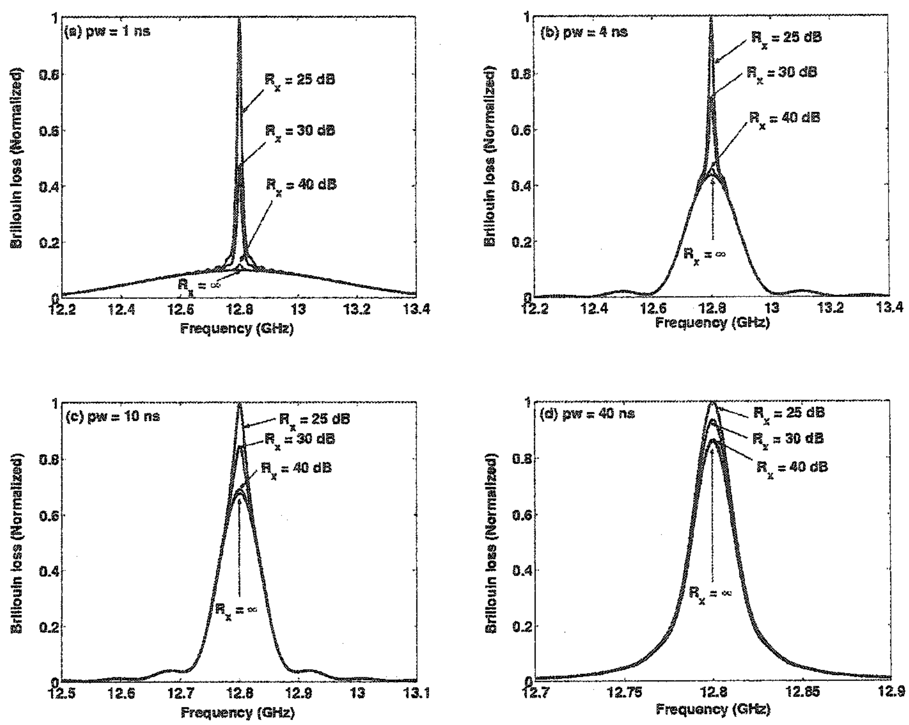

Figure 4.4: Theoretical Brillouin profiles for different extinction ratios. The pulse widths are 1, 4, 10, and 40 ns in a), b), c), and d) respectively. Decreasing the extinction ratio substantially narrows the profiles of short pulses but has almost no effect on long pulses. In each figure, all curves are normalized to the maximum intensity of the strongest profile.

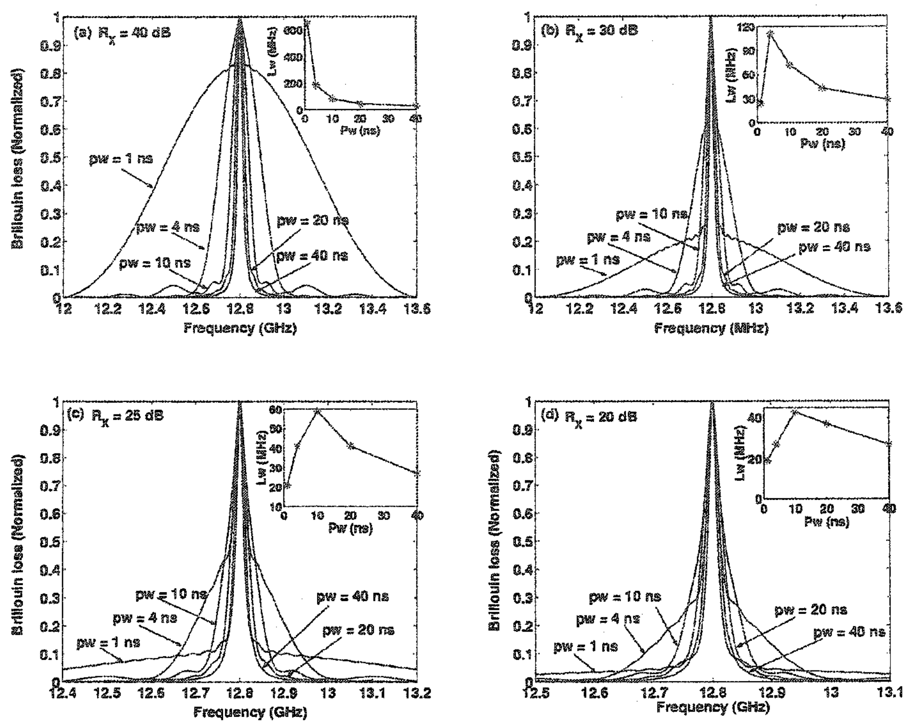

Figure 4.5: Theoretical Brillouin profiles for different pulse widths. The extinction ratios are 40, 30, 25, and 20 dB in a), b), c), and d) respectively. The corresponding insets reveal that the maximum linewidth decreases and shifts to larger pulse widths as the extinction ratio decreases. Each profile is normalized to its intensity maximum.

4.2.1 Experimental Evidence

Figure 4.6 reveals experimental evidence of a Brillouin profile resembling a twofold structure similar to that the $R_x = 25dB$ curve in Figure 4.4(a). In addition, experimental results confirm the twofold structure when the system parameters are changed. For instance, increasing the incident pulse width from 1.5 to 2.5 ns for a constant leakage power (Figure 4.7) yields a significant incline in the spectrum trunk along with an elevated top. As mentioned earlier, the power spectrum linewidth varies inversely with the time-domain pulse width as predicted by Fourier analysis. Consequently, wider pulses contain fewer frequency components and are thus narrower in frequency space. Therefore, when the underlying leakage-pump interaction remains constant for an increased pulse width, the spectrum trunk elevates and narrows. The elevation arises from an increased pulse energy and interaction length resulting from pulse widening. Such behaviour can be understood using the numerical results shown in Figure 4.8.

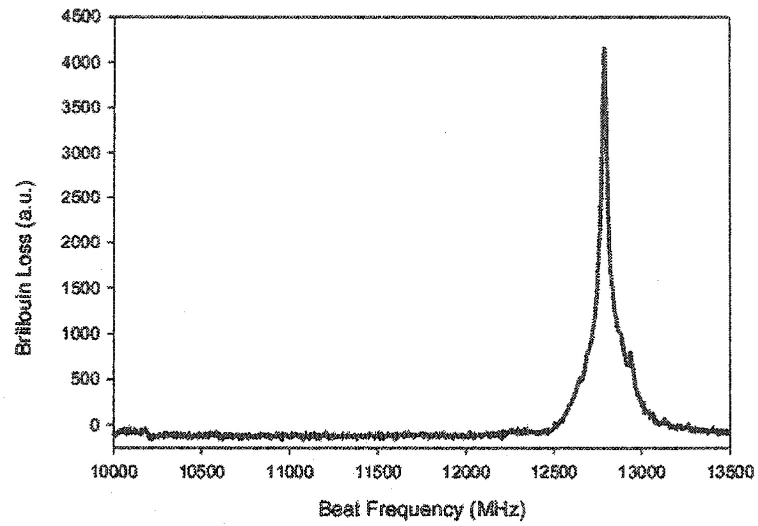

Figure 4.6: A representative experimental Brillouin spectrum revealing a twofold Gaussian-Lorentzian structure. Considerable non-uniform broadening is observed in the bottom third of the spectrum. The experimental figures shown throughout Chapter 4 were generated using a 2.0 ns pulse width, 2.0 km fibre length, 1 mW pump power, 1 mW leakage power, and 70 mW peak pulse power.

Changing the CW leakage power (extinction ratio) also consistently reveals the twofold structure. When the leakage power increases for a constant pulse width, the upper spectrum portion elevates and broadens while the much wider bottom portion (trunk) remains unchanged. This behaviour is shown experimentally in Figure 4.9, where Brillouin spectra were acquired for a 2.5 ns pulse width, and 14 and 19 dB extinction ratios. The higher intensity spectrum was acquired using the 14 dB extinction ratio (i.e. bigger leakage power). Since an increased leakage power generates a more dominant CW-CW interaction over a long interaction length, a larger Brillouin loss occurs in the narrow central region. This behaviour is numerically confirmed in Figure 4.10 where Brillouin spectra were obtained for 2.5 ns pulses and different leakage powers (extinction ratios 15 and 20 dB).

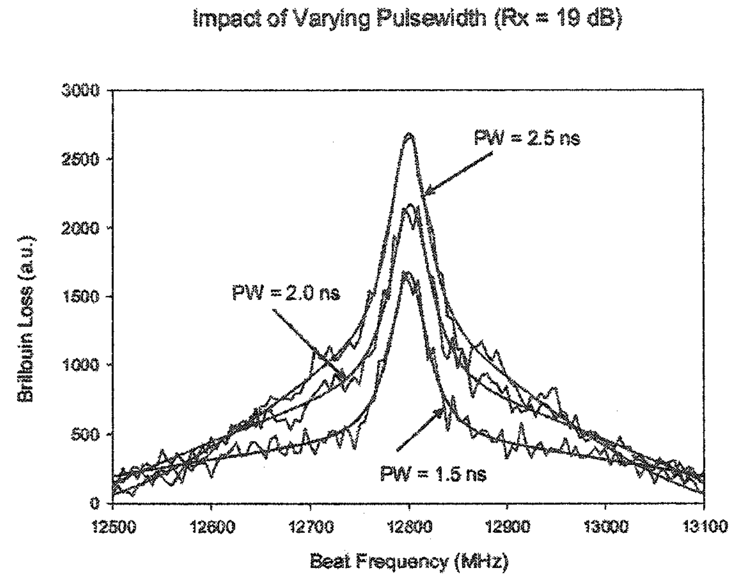

Figure 4.7: Experimental Brillouin spectra obtained by varying the pulse widths (1.5, 2.0 and 2.5 ns) for a 19 dB extinction ratio. Profile fitting was done using Equation 4.2, which is explained in section 4.3.

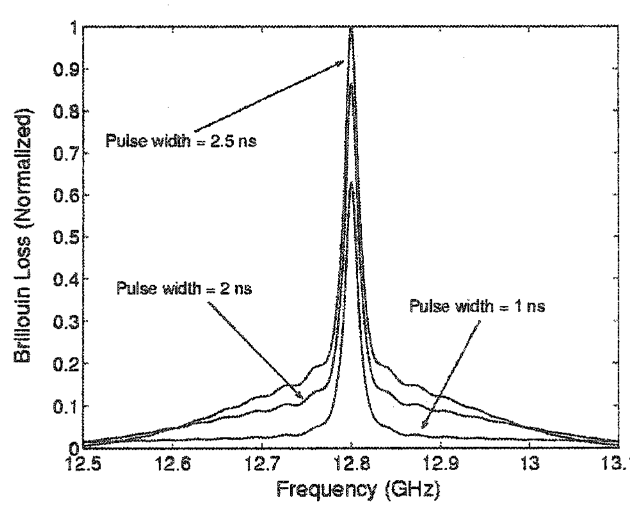

Figure 4.8: Theoretical Brillouin spectra obtained with a fixed leakage power (0.02 mW, $R_x = 20dB$) and varying pulse widths (1.0, 2.0, 2.5 ns). All profiles are normalized to the maximum intensity of the strongest profile.

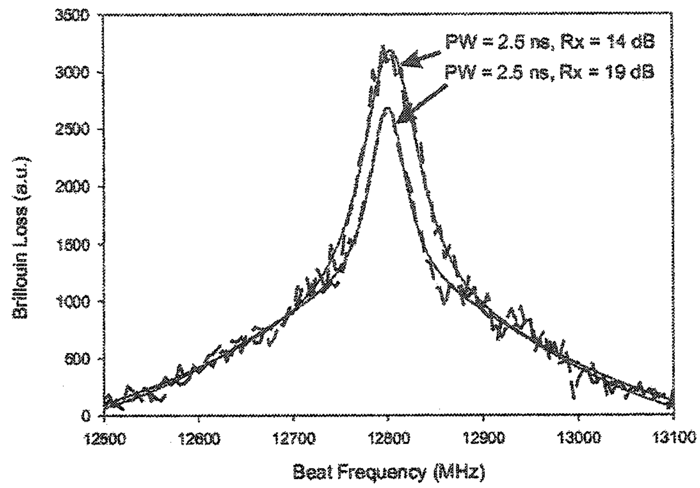

Figure 4.9: Experimental Brillouin spectra obtained by varying the extinction ratio (14 and 19 dB) for a 2.5 ns pulse width. The upper curve shows an elevated central portion due to enhanced CW-CW interaction. Profile fitting was done using Equation 4.2, which is explained in section 4.3.

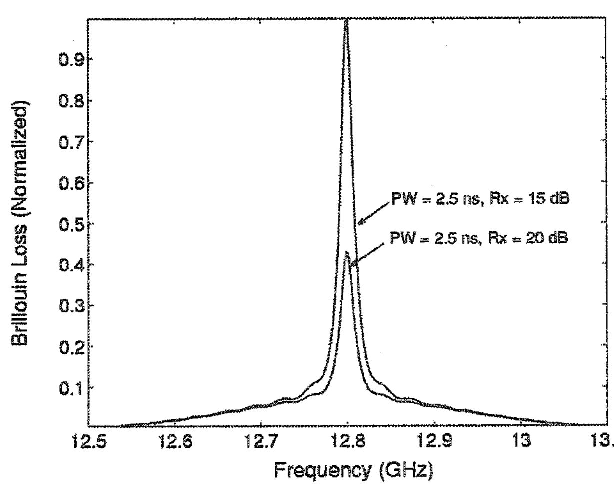

Figure 4.10: Theoretical Brillouin spectra obtained with a fixed pulse width (2.5 ns) and varying leakage powers (0.020 and 0.065 mW, $R_x = 20\, and\, 15\, dB$, respectively). Like the experimental results shown in Figure 4.9, the higher leakage curve elevates due to enhanced CW-CW interaction. Both profiles are normalized to the maximum intensity of the strongest profile.

In summary, both experimental and numerical results confirm the twofold structure of the Brillouin spectral profile. Therefore, a suitable fitting method should take this twofold structure into consideration.

4.3 Spectral Fitting Method

A spectral fitting method has been developed to account for the twofold Brillouin profile structure observed both experimentally and numerically [Ferrier *et al.* 2003]. In this method, a double linewidth pseudo-Voigt profile given as

$$P(\nu) = P_{MAX}\left(\frac{\beta}{1+4\left(\frac{\nu-\nu_B}{\gamma_1}\right)^2} + (1-\beta)\exp\left(-4\ln 2\left(\frac{\nu-\nu_B}{\gamma_2}\right)^2\right)\right) + P_0 \qquad (4.2)$$

is used to fit the experimental data.

In this form, the Brillouin loss spectrum represents a combination of Lorentzian and Gaussian distributions and has six free parameters (β, P_{MAX}, ν_B, γ_1, γ_2, P_0). The shape factor, β, determines the appropriate proportion of Brillouin loss from each process, and is dependent on interaction length and laser powers. The profile becomes Lorentzian when $\beta = 1$, and evolves to a Gaussian as $\beta \to 0$. The maximum loss of the spectrum, P_{MAX}, occurs when the beat frequency of the counter-propagating laser beams (ν) equals the Brillouin frequency of the fibre (ν_B). The full width half maximum (FWHM) or linewidth of the Brillouin spectrum is a combination of γ_1 and γ_2, the linewidths of the CW-CW and pulse-CW interactions, respectively, and P_0 is the offset power.

Figure 4.11 shows zoomed views (600 MHz) of Figure 4.6 to clearly show the differences in various fitted profiles. Curve fitting parameters were determined using the nonlinear least squares Levenberg-Marquardt algorithm [Marquardt 1963] for the constrained (forcing $0 \le \beta \le 1$) and unconstrained ($\beta \in R$) single linewidth profiles ($\gamma_1 = \gamma_2$, [Brown *et al.* 1998]) and the unconstrained double linewidth profile ($\gamma_1 \ne \gamma_2$), and their values are shown in Table 4.1. The curve fitting procedure was done using the existing code in Sigmaplot®

for the Levenburg-Marquardt algorithm, and the existing Voigt function was modified to accommodate our single and double linewidth functions. The accompanying R^2 values in Table 4.1 are the coefficients of determination and represent the goodness of fitting to the experimental data where $R^2 = 1$ indicates a perfect match. Since the constrained single linewidth profile found $\beta = 1$ (Lorentzian) rather than $\beta = 0$ to minimize the curve fitting error, an additional pure Gaussian profile ($\beta = 0$) was used to determine its compatibility with the experimental profile. As expected, the Gaussian profile provided a much poorer fit.

While the Brillouin frequency was reasonably well determined by the single linewidth profiles, the corresponding Brillouin linewidth and power predictions varied significantly from the experimental data. Such large variations in linewidth and power arise from the constrictive nature of the curve fitting, i.e. numerically forcing $0 \leq \beta \leq 1$. This restricted the flexibility of the remaining parameters. For unconstrained curve fitting, the error was reduced only when $\beta > 1$. Therefore, the experimental data cannot be represented by a Gaussian-Lorentzian single linewidth combination.

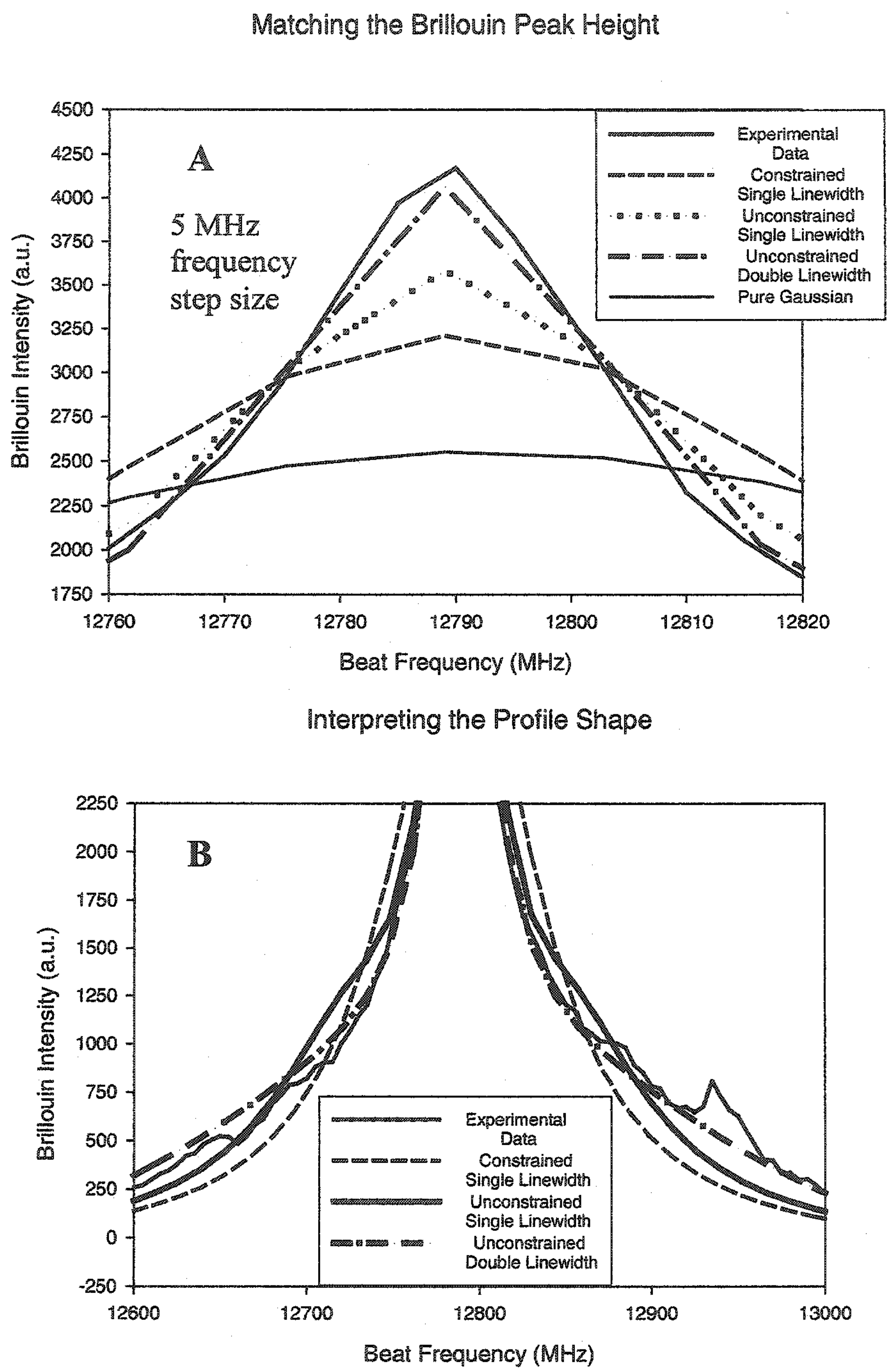

Figure 4.11: Zoomed views of Figure 4.6 showing various curve fitting methods used to comparatively examine the experimental profile data. A) Upper spectral portion for matching peak experimental height. B) Spectral trunk portion comparing goodness of fitting to overall profile shape (bottom). The peak experimental Brillouin loss is 4171.02 a.u.

	Gaussian Single Linewidth	Constrained Single Linewidth	Unconstrained Single Linewidth	Unconstrained Double Linewidth
R^2	0.88433688	0.95299197	0.98167	0.99337044
P_{MAX}	2628.8901	3308.9469	3692.9297	4168.9284
γ_1 (MHz)	156.715	104.5211	76.4911	39.4365
γ_2 (MHz)	156.715	104.5211	76.4911	310.3904
β	0.0000	1.0000	2.0674	0.7394
ν_B (MHz)	12792.0123	12789.8828	12789.4802	12789.3716
p		1.49E-04		1.49E-04

Table 4.1: Curve fitting parameters for 4 different profiles.

The differences in curve fitting are clear. The single linewidth profiles underestimate the Brillouin peak height and overestimate the Brillouin linewidth. Between the single linewidth profiles, the unconstrained profile more closely matches the experimental data by allowing $\beta > 1$, but at the expense of noticeably distorting the curve fit (see Figure 4.11b). In any case, single linewidth profiles search for one linewidth representing a uniformly varying curve, which cannot be found here.

However, the unconstrained double linewidth profile follows the experimental data extremely well in a symmetric way, thus overlooking weak asymmetries such as the peak at 12930 MHz, which is attributed to residual fibre strain. In addition, the Gaussian and Lorentzian linewidths, indicative of the pulse-CW and leakage-CW interactions respectively, are clearly distinguished. Furthermore, the Brillouin frequency and peak height are well predicted while maintaining $0 \le \beta \le 1$ comfortably, even for this unconstrained method (allowing $\beta \in R$).

To compare the statistical significance between the various curve-fitting methods, an F-test was conducted on the curve fitting data. The F-test tests the statistical significance between two curve fitting methods by examining the residuals between the fitted and experimental data. If the residuals are found to be similar, the F-test concludes that the two curve-fitting methods are not statistically significant. In other words, experimental errors dictate the main differences. However, when the residuals are very different, the F-test concludes statistical significance between the two curves. The curve fitting methods themselves should belong to the same family of functions but have differing degrees of freedom. The main output from the F-test is a probability p, which is nominally compared with the acceptable value for statistical significance, $p=0.05$ (5%). If $p < 0.05$, then one has greater than 95% confidence that the curve fits are statistically significant. However, to show scientific importance, one must obtain probability values from other data populations.

The F-test results showed that the double- and single-linewidth curve fits are statistically significant, yielding a >99% probability (p = 9.82e-171 <<< 0.05) that the curve fitting differences do not emerge only from data fluctuations (noise). To determine scientific validity, F-tests were performed on other data sets, with less-exaggerated differences in spectral shape. The results of F-tests described here reflect only those between the constrained single-linewidth and unconstrained double-linewidth curves since the unconstrained single-linewidth function is essentially non-physical, yielding $\beta > 1$. A high p-value of 1.49e-4 was found when the two curves varied weakly, and the data in Figure 4.7 generated very low p-values (9.32e-11, 5.67e-28, 2.73e-37). Such low values weren't surprising since the differences in curve fitting were visibly noticed. Again, one should not expect the p-values to be universally equal among different populations since the residuals from the single-linewidth method are enhanced when the pulse-CW linewidth component plays a larger role in the overall spectral shape.

Until now, the discussion has focussed on the benefits of having a leakage power, which generates an additional narrow Lorentzian component in the Brillouin loss profile. This is advantageous when using short pulses, which exhibit inherently broad Gaussian profiles, because the narrow Lorentzian component reduces the error in Brillouin frequency and hence temperature and strain measurements according to Equation A.5. However, the existence of a CW leakage component in the Stokes pulse has been shown to generate cross talk from different fibre sections, which influence the Brillouin frequency information acquired through BOTDA [Afshar *et al.* 2003b]. In particular, a stronger leakage power enhances this cross talk noise and thus decreases the SNR significantly. This could degrade the strain and temperature resolutions since SNR appears in the denominator of Equation A.5.

4.4 BOTDA Limitations

Brillouin optical time domain analysis (BOTDA) involves measuring the round trip time of an optical pulse to monitor all sensing fibre regions in a distributive manner. This round trip time represents the time required for light to travel to a desired fibre location plus the time needed to return to the detector. The spatial resolution of this technique is determined by the optical pulse width, which acquires the average strain and temperature conditions within a fibre region of equivalent length. Therefore, time and fibre position exhibit a 1:1 correspondence through $z = ct/2n$, and equivalently $\Delta z = c\tau/2n$, where Δz and τ are the spatial resolution and pulse width respectively. Taking $c = 3\times10^8 m/s$ and $n = 1.5$, the ratio between time and distance is $10 ns/m$. Therefore, BOTDA indicates that a signal detected at time t represents the Stokes-pump interaction at time $t/2$ and position $z = ct/2n$.

As previously discussed, the Brillouin interaction consists of competing leakage-CW and pulse-CW interactions. Since the leakage-CW interaction continuously occurs within the fibre, the availability of CW pump power for pulse-CW interaction depends on the amount of CW-CW interactions occurring before and after the pulse entrance. In particular, assuming that z lies in region B (see Figure 4.12), the existence of leakage power complicates the corresponding Brillouin frequency measurement acquired through BOTDA in two ways. First, before the pulse-pump interaction at $t/2$ and $z = ct/2n$, the CW leakage continuously depletes the oncoming pump during time interval [0, $t/2$] in region C. Second, after the pulse-pump interaction at z, the depleted pump continues to interact with the CW leakage component as it propagates in region A toward the detector. Therefore, the signal detected at time t carries the Brillouin frequency information of position z as well as regions A and C.

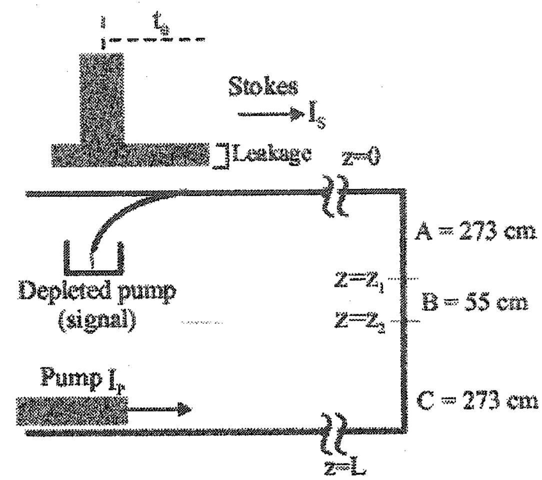

Figure 4.12: Geometry for numerically examining Brillouin frequency cross talk.

Consequently, the strength of leakage-pump interactions in regions A and C dictates their influence on the Brillouin frequency spectrum from region B. This impact emerges as additional Brillouin frequency peaks corresponding to regions A and C, which are pronounced under strong leakage-CW interactions, thus yielding complex Brillouin spectra like those shown in Figure 4.13. In this example, three different fibre sections, A, B, and C, have different strains and lengths along the sensing fibre, as shown in Figure 4.12. The strains of these sections correspond to Brillouin frequencies f_1=12800 MHz, f_2=12800-31.9 MHz, and f_3=12800+31.9 MHz, respectively.

Figure 4.13 shows the Brillouin profiles corresponding to the middle of section B for different extinction ratios. In the absence of leakage power ($R_x = \infty$), one peak corresponding to the Brillouin frequency of section B (f_2) is shown, as expected. However, for finite extinction ratios, the Brillouin profile actually comprises three peaks at f_1, f_2, and f_3 corresponding to the Brillouin frequencies of all three sections. In this way, the emergence of frequencies f_1 and f_3 only occur when a CW leakage component influences the measurement. This causes confusion in determining the true Brillouin frequency shift of strained section B, and errors when the Brillouin frequencies of neighbouring sections are near that of this section.

This confusion and error is dependent on the relative interactions of the pulse and leakage with the oncoming pump beam, which are dependent on the pulse width, extinction ratio, and fibre section lengths. The pulse-CW interaction brings out information from region B whereas leakage-CW interactions bring information from regions A-C. Consequently, decreasing the extinction ratio and/or pulse width, or increasing the lengths of neighbouring fibre sections causes more confusion and error [Afshar *et al.* 2003b]. However, this limitation can be resolved by investigating the Brillouin time domain for different beat frequencies.

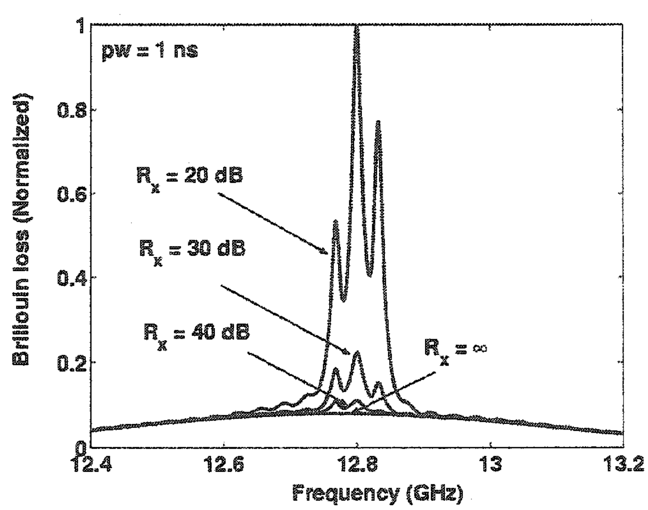

Figure 4.13: Theoretical Brillouin profiles from a point in the middle of section B for different extinction ratios. Section B is under strain with a Brillouin frequency of $f_2 = 12800 - 31.9$ MHz. Three different peaks at $f_2 = 12800 - 31.9$, $f_1 = 12800$, and $f_3 = 12800 + 31.9 MHz$ are observed in the profiles. The height of extra peaks, f_1 *and* f_3, relative to the true Brillouin peak from section B, f_2, reduces for bigger extinction ratios. All curves are normalized to the maximum intensity of the strongest profile.

4.5 Resolving BOTDA Limitations

In this section, the Brillouin time domain is used to resolve the complex Brillouin spectrum, described above, from a given fibre position to identify its true Brillouin frequency peak. In particular, when the pump and Stokes beams generate beat frequencies matching those of the Brillouin spectral peaks, the respective Brillouin time domains acquire unique identifiable characteristics.

For example, consider Figure 4.13 where three frequency peaks f_1, f_2, and f_3 exist in the Brillouin profile. The corresponding time domain curves for three beat frequencies ($\nu_p - \nu_s = f_1, f_2, f_3$) and two extinction ratios $R_x = \infty$ and $R_x = 40dB$ are shown in Figures 4.14 a) and b).

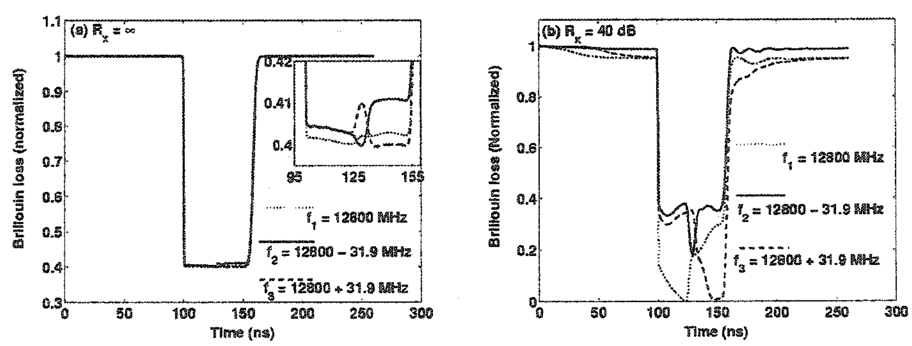

Figure 4.14: Time domain signals for a) $R_x = \infty$ and b) $R_x = 40dB$ were examined for 260 ns. In each plot, three Stokes frequencies matching the Brillouin frequencies of fibre sections A, B, and C (see Figure 4.12) have been examined. In each figure, all curves are normalized to the maximum intensity of the strongest profile.

To simulate having a leakage power present in the fibre before the pulse enters, a time difference, t_0=100 ns, between the arrivals of the leakage and pulse is introduced (see Figure 4.12). This time is chosen to be greater than the 600 cm (60 ns) fibre length to ensure that the whole fibre is engulfed with leakage before the pulse enters. Since the speed of light in fibres is approximately 20 cm/ns, the full Brillouin time domain, encompassing $2\times\frac{600(cm)}{20(cm/ns)} = 60ns$, represents the time required to detect the pulse-pump interaction from the end of the fibre. Hence, a one-to-one correspondence between time and fibre distance exists within the $t \in [100ns,160ns]$ timeframe. Finally, another 100 ns was added after the pulse exited the fibre, thus completing a full 100+60+100=260 ns interaction time.

As shown in Figure 4.14 a), the CW pump experiences no depletion before 100 ns and after 160 ns since no leakage power ($R_x = \infty$) exists to initiate the depletion. However, during time interval $t \in [100ns,160ns]$, a large depletion owing to the pulse-CW interaction occurs within fibre region B when its Brillouin frequency matches the beat frequency (i.e. $\nu_p - \nu_s = f_2$). Consequently, since the remaining fibre regions A and C do not resonate with the beat frequency (i.e. $\nu_p - \nu_s \neq f_1, f_3$), they experience less depletion. In a similar fashion, maximum depletion occurs in regions A and C when their respective Brillouin frequencies match the input beat frequency, as shown in the inset of Figure 4.14 a).

This depletion resulting from pulse-CW interaction is also apparent in Figure 4.14 b) even when a small leakage component ($R_x = 40dB$) is included with the Stokes pulse. However, in contrast with Figure 4.14 a) having no leakage, an additional depletion of the CW pump beam during $t_2 \in [0,100ns] \cup [160ns,260ns]$ occurs with an amount dependent on the number of CW-CW resonance interactions occurring within the fibre. For instance, at beat frequency f_2, almost no CW-CW depletion is observed during time t_2 since the Brillouin frequencies of larger fibre sections A and C, constituting the bulk of the fibre length, do not match f_2. Conversely, when beat frequencies f_1 and f_3 are used, a significantly larger depletion occurs during time t_2 because many strong resonating CW-CW interactions occur over the fibre lengths A and C respectively.

Figure 4.14 b) also reveals that the CW-CW interactions ultimately generated larger pump depletions within the sensing fibre; nearly doubling in regions A and C when they experience resonance. With this in mind, fibres experience maximum pump depletion when operating at the resonance condition. Hence, the maximum pump depletions in regions A, B, and C occur when the beat frequencies are f_1, f_2, and f_3 respectively. Therefore, finding the time domain exhibiting a global maximum depletion in region B can identify the Brillouin frequency of region B. Indeed, as shown in Figures 4.14 a) and b), this global maximum occurs within region B only at beat frequency f_2. Although the absolute pump depletion from beat frequency f_1 is superior in region B [Figure 4.14 b)], it does not constitute a global maximum depletion within the fibre length, and hence does not resonate with region B. Consequently, the true Brillouin frequency from any fibre section can be identified by subsequently resolving the time domain behaviours from the observed Brillouin frequencies when the depletion varies more than the noise fluctuations.

Chapter 5: Brillouin Temperature Spectrum

This chapter presents measurements of Brillouin loss intensity vs. temperature for real-time temperature monitoring. Analysis of distributed *Brillouin temperature spectra* will determine their feasibility in real-time dynamic temperature applications such as fire detection.

5.1 Introduction

Distributed fibre optic temperature sensing has recently been introduced for fire detection [Meacham 1994, Morgan 2000] and, unlike conventional fire detectors, uses an entire optical fibre as the sensing medium. Consequently, the fibre temperature can be determined at every fibre location along fibre lengths approaching 51 km [Bao *et al.* 1995b]. Fibre optic cables are ideal for temperature measurement due to numerous physical attributes including low mass, fast response, high strength and flexibility, resiliency, and immunity to electromagnetic interference. Conceivably, the location, size, and development of a fire [Morgan 2000] can be determined with an unmatched flexibility of measurement locations and a virtually unlimited number of locations simultaneously. Distributed fibre optic temperature sensors have been used to monitor a variety of environments including tunnels, underground railways and stations, conveyor lines, steelworks, and petrochemical plants [Iida *et al.* 1994, Morgan 2000, Maegerle 2001, Wang *et al.* 2001].

In conventional applications, distributed Brillouin sensor systems employing the probe-pump amplification technique obtain temperature and strain information by collecting the Brillouin frequency spectra from every position along an optical fibre. Although this method has proven to be effective in monitoring quasi-static (slow) temperature or strain variations, it is impractical for rapidly varying environmental monitoring. This is because for every beat frequency within a specified frequency range, polarization scrambled time-domain waveform data must be collected and averaged within the timeframe of possible strain or temperature variations. The full process typically requires 5-10 minutes but can be extended by using longer fibres and increased averaging (Figure 5.1) and sampling rates.

Clearly, this scanning technique would be inappropriate for fire detection where much shorter response times are required.

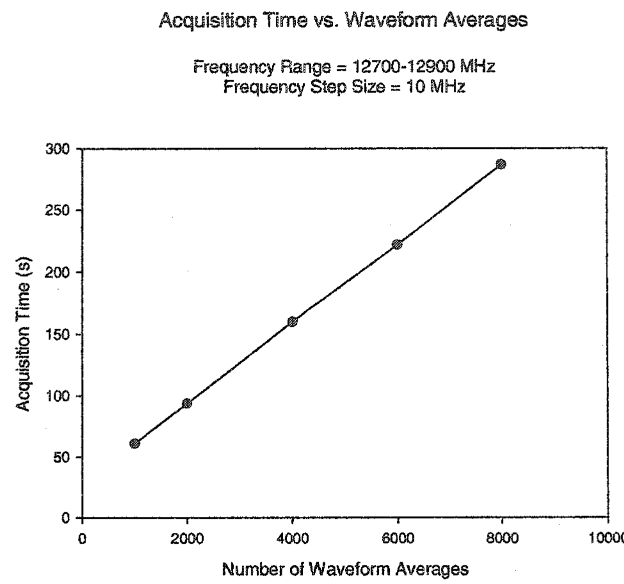

Figure 5.1: Experimental data confirms a linear increasing relationship between acquisition time and waveform averaging.

To deal with this problem, Bao *et al.* performed transient experiments, which involved monitoring the Brillouin intensity versus time for given threshold temperatures [Bao *et al.* 1996]. As expected, the maximum Brillouin intensities occurred at temperatures corresponding to the fibre's Brillouin frequencies. A spatial resolution of 5 m was achieved using a 22 km fibre length with an approximately 2 - 4 s response time. Since there is a great demand from the fire detection community for point-to-point distributed sensing of various structures, the spatial resolution should be as short as possible. In addition, for remote monitoring, the fibre must be several kilometres in length. Therefore, a series of experiments were conducted using short pulse widths and long fibre lengths to demonstrate the capabilities of the current Brillouin system for distributed temperature sensing.

5.2 Theory

As shown in Chapter 4, the Brillouin frequency spectrum follows the double linewidth pseudo-Voigt function given by

$$P(\nu)=P_{MAX}\left(\frac{\beta}{1+4\left(\frac{\nu-\nu_B}{\gamma_1}\right)^2}+(1-\beta)e^{-4\ln 2\left(\frac{\nu-\nu_B}{\gamma_2}\right)^2}\right). \tag{5.1}$$

For a narrow frequency range, the Brillouin spectrum approximates well to a Lorentzian function given by

$$P(\nu)=\frac{P_{MAX}}{1+4\left(\frac{\nu-\nu_B}{\gamma_1}\right)^2}. \tag{5.2}$$

In the absence of strain changes ($\varepsilon=\varepsilon_0$ in Equation 2.16), the Brillouin frequency behaves linearly with temperature through

$$\nu_B(T)=\nu_{B0}+C_T(T-T_0). \tag{5.3}$$

Again, T_0 represents the temperature for a known Brillouin frequency ν_{B0}, and C_T is the temperature-frequency slope. Therefore, assuming P_{MAX} and γ_1 are invariant with temperature, the *Brillouin temperature spectrum* also behaves as a Lorentzian function through

$$P(T)=\frac{P_{MAX}}{1+4\left(\frac{\eta-T}{\kappa}\right)^2}, \tag{5.4}$$

where $\eta=\frac{1}{C_T}(\nu-\nu_{B0}+C_T T_0)$ and $\kappa=\gamma_1/C_T$.

Two things are noteworthy from Equation 5.4. First, a constant η implies a constant beat frequency (ν) between the two lasers. Therefore, acquiring a Brillouin temperature maximum or threshold requires matching the environmental temperature T to a known beat frequency ν. Interestingly enough, this procedure is the complete reverse of that required to obtain Brillouin frequency spectra. Hence, this procedure advantageously eliminates the time required to step the beat frequency. Second, the temperature linewidth (κ) is inversely proportional to C_T. Although single mode fibres nominally exhibit wavelength-dependent C_T values near 1.2 MHz/°C, panda-type polarization maintaining fibres (PMF's) can yield C_T values near 2.8 MHz/°C [Imai and Shimada 1993]. Therefore, these PM fibres could allow for rapid alarm signals when the threshold temperature is exceeded, since the Brillouin intensity falls off more rapidly away from the maximum.

However, the Brillouin temperature spectrum becomes more complex when P_{MAX} and γ_1 changes with temperature. Indeed, previous investigations have shown that the Brillouin frequency linewidth (γ_1) decreases linearly with temperature [Niklès *et al.* 1997, Smith 1999]. Using a 55 ns pulse width, Smith acquired a linear linewidth-temperature relationship given by [Smith 1999]

$$\gamma = 37.8MHz - 0.173MHz/°C\left(T(°C) - 23°C\right), \tag{5.5}$$

over a small temperature range (-20 to 50 °C). With this information and using Equation 5.4, plots of Brillouin loss vs. temperature for given "γ vs. T" slopes are shown in Figure 5.2. When a weak decreasing linear relationship between Brillouin frequency linewidth and temperature exists, a slight asymmetry favouring temperatures below threshold occur as the slope magnitude increases.

Both Parker and Smith determined that the Brillouin peak power increased linearly with temperature in the steady state regime [Parker *et al.* 1997, Smith 1999]. Under this regime, we have

$$P_{MAX}(T) = P_{MAX}(T_0) + \mu(T - T_0), \tag{5.6}$$

where the Brillouin peak power vs. temperature slope, $\mu > 0$. Hence, Equation 5.4 becomes

$$P(T) = \frac{P_{MAX}(T_0) - \mu T_0}{1 + 4\left(\dfrac{\eta - T}{\kappa}\right)^2} + \frac{\mu T}{1 + 4\left(\dfrac{\eta - T}{\kappa}\right)^2}. \tag{5.7}$$

When $\mu \neq 0$, the Brillouin temperature spectra no longer experiences a maximum interaction when $\eta = T$. Indeed, the maximum will be shifted by an amount dependent on the magnitude of $P_{MAX}(T_0)/\mu$, as shown in Appendix B. An experimental investigation of the Brillouin linewidth and peak power vs. temperature can be found in section 5.3.3.

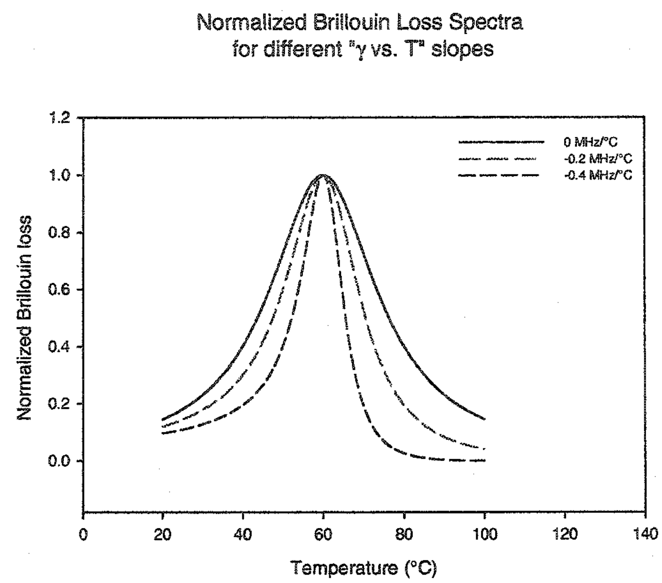

Figure 5.2: Brillouin temperature spectra are given for representative "γ vs. T" slopes of 0, -0.2, and -0.4 MHz/°C. Each profile is normalized to its intensity maximum.

5.3 Experimental Investigations

This section presents experimental investigations on distributed Brillouin temperature spectra. Section 5.3.1 discusses preliminary Brillouin gain measurements obtained from a 10 m fibre section on an 11 km fibre length using a 20 ns (2 m) pulse width. Sections 5.3.2 and 5.3.3 present Brillouin loss vs. temperature measurements from a 2 km fibre length using a 20 cm pulse width. Section 5.3.2 reveals the distributed nature of the Brillouin sensor by monitoring separate 2, 5, and 10 m fibre sections exposed to the same temperature variations. Brillouin intensity measurements were collected every 20 seconds to capture a 4000-averaged 2 km fibre length while the beat frequency was held constant at 12830 MHz. Section 5.3.3 presents a more thorough investigation on the Brillouin peak power and frequency linewidth as a function of temperature. In this investigation, a 30 m optical fibre section was placed in a thermally insulated Styrofoam box. For several well-established temperature conditions, the corresponding Brillouin frequency spectra were acquired to determine the relationship between Brillouin peak power and linewidth vs. temperature.

5.3.1 "Hot Spot" Detection

The following experiment involves monitoring the temperature conditions of an 11 km fibre by monitoring the Brillouin intensity versus time [Liu *et al.* 2002]. A looped 10 m fibre section was subjected to temperature variations, while the remaining fibre was left at room temperature. This was done to demonstrate the potential of the system at a 2 m spatial resolution. The temperature varying fibre, hereafter called the "hot spot", was positioned approximately 8 km from the CW pump laser. The experiment began by having the frequency difference between the lasers locked to a value of 12860 MHz, which corresponds to a preset threshold temperature. A heat gun was used to increase the temperature of the 10 m "hot spot", and was placed within close proximity for increased heat intensity. A thermocouple was then placed near the "hot spot", while both were thermally insulated to minimize the heat loss. Finally, the Brillouin signals were observed and recorded using a digitizing oscilloscope at a rate of approximately 2 seconds per waveform. By limiting the number of time domain averages to just 10, this data acquisition rate was accessible.

5.3.1.1 Experiment Results

The Brillouin intensities of the 10 m "hot spot" have been acquired for several temperatures in the 40-80 °C temperature range over a 20 s timeframe. The threshold temperature corresponding to a 12860 MHz Brillouin frequency has been determined experimentally from the Brillouin intensity results, and theoretically using Equation 5.3. The reference data, ν_{B0} and T_0, are obtained from the temperature-frequency calibration shown in Figure 5.3, yielding the following relationship

$$\nu_B(T) = 12796 + 1.22(T - 20). \tag{5.8}$$

From this equation, a 72.4 °C temperature corresponds to a 12860 MHz Brillouin frequency. For C_T, the value of 1.22 MHz/°C is regarded as standard for SMF-28 single mode fibre [Smith 1999, DeMerchant 2000].

The experimental results are provided in Figures 5.4 and 5.5, where the Brillouin intensity of the "hot spot" was plotted versus time and temperature respectively. Both plots reveal that the Brillouin intensity increases with time during heating, and that the maximum gain was obtained at a temperature of 66 °C. Consequently, a 6-7 °C temperature uncertainty is apparent from this experiment. This is mainly attributed to a relatively long 2 m spatial resolution compared with the 10 m "hot spot", combined with the slowly changing temperature gradients existing near its boundaries, resulting in non-uniform temperature changes throughout the entire "hot spot" region.

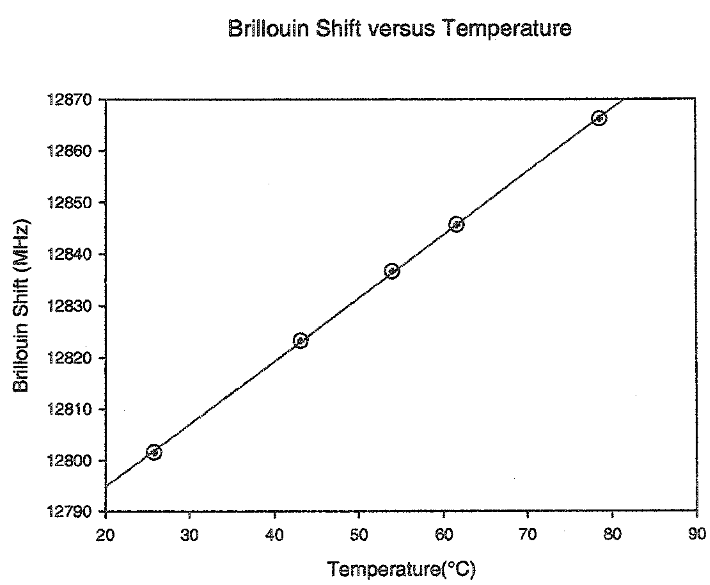

Figure 5.3: A temperature-frequency calibration confirms a linear relationship between the two variables. The slope provides an accurate value for C_T, over the operating temperature range.

In Figure 5.4, this phenomenon is observed as the central region buckles relative to the "hot spot" boundaries. Since the Brillouin detection system averages the temperature over a given spatial resolution to obtain temperature information, the Brillouin gain throughout the 10 m has been somewhat diminished. In addition, by using only 10 time-domain averages, the noise levels increase and hence influences the Brillouin gain data, especially when the gain is low. This would explain the non-uniform temperature variations shown in Figure 5.5, where the Brillouin gain changes are small.

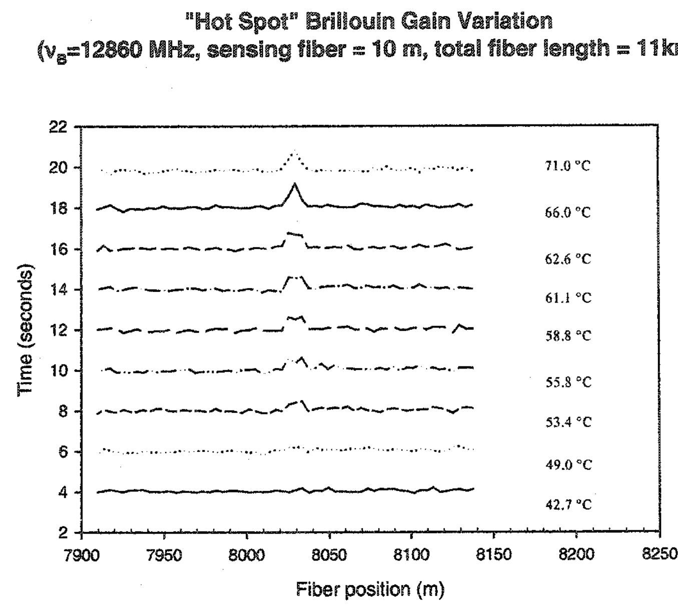

Figure 5.4: Variation of the Brillouin power gain with time. The fibre position is the distance from the CW pump laser. The Brillouin gain increases within the 10 m "hot spot" during heating, and maximizes after 18 s.

To practically limit the temperature uncertainty, it would seem that more time-domain averages are required to filter out excess optical and electrical noise. However, in a similar temperature threshold experiment [Bao *et al.* 1996], only 8 time-domain averages were required to monitor transient temperature measurements in a 22 km single mode fibre, where a 100 m sensing length was monitored using a 50 ns pulse (5 m spatial resolution). The larger 20:1 *length ratio* creates a more uniform temperature distribution throughout the majority of the sensing fibre length. In this way, the pulse energy is used in a more constructive manner in maintaining temperature integrity. Consequently, this length ratio is an important parameter in real-time temperature monitoring. The temperature error could also be reduced if temperatures could be collected at shorter time intervals.

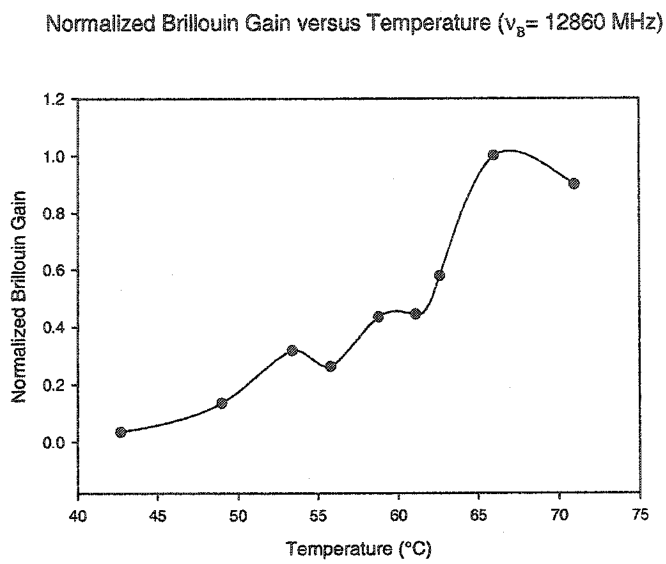

Figure 5.5: Variation of Brillouin power gain with "hot spot" temperature. During heating, the "hot spot" Brillouin gain increases until the threshold temperature (T_{th}) of 66°C is reached. Continued heating (T > 66°C) results in diminished gains as the Brillouin frequency corresponding to T_{th} is no longer matched. The data are normalized to the global intensity maximum.

5.3.2 Rapid Distributed Data Acquisition

The following experiment involves rapid Brillouin intensity measurements of three fibre loops (2 m, 5 m, and 10 m), each separated by 20 m of loose, room temperature fibre, with a 20 cm spatial resolution. The three loops were submerged in a 1000 ml beaker filled with water, which was heated using a hot plate. The water temperature was monitored using a thermometer. As in section 5.3.1, the temperature ranges from 20-80 °C so a beat frequency of 12830 MHz, corresponding to a 49.1 °C threshold temperature, was chosen to ensure that a relatively equal number of data points were acquired on either side of the intensity maximum. In this way, a symmetric Brillouin temperature spectrum could be analyzed. The 49.1 °C threshold temperature value was evaluated using the Brillouin frequency vs. temperature calibration performed in section 5.3.3.

By maintaining a constant beat frequency, averaged Brillouin time-domain data along 2 km were collected every 20 seconds throughout the entire heating cycle. Due to the fibre length involved and the memory limitations of the digitizer, Brillouin time domain data were acquired at a 2 m/S (2 m per sample) sampling rate. Although a 20 cm pulse was used in this experiment, the 2 m/S acquisition rate becomes the true spatial resolution since no Brillouin intensity information is known within 2 m. As in Chapter 4, the pump and peak pulse powers are 1 mW and 70 mW respectively utilizing a 19 dB extinction ratio.

Figure 5.6 compares two representative Brillouin time domains of the 2, 5, and 10 m fibre loops. The Brillouin time domains within the three loops achieve maximum intensities at 47.5 °C. Compared with room temperature (22.5 °C), the Brillouin intensity has increased significantly. Figure 5.7 reveals the resulting Brillouin temperature spectra for the three loops. The 5 and 10 m fibre regions experienced slightly larger gains than that of the 2 m fibre. Like Figure 5.6, all spectra reached a maximum intensity at 47.5 °C, as confirmed by respective curve fits. Hence an absolute $49.1 - 47.5 = 1.6°C$ threshold temperature error is determined. Due to non-uniform temperature increases between and during consecutive 20 s runs, the spectral shapes are highly asymmetric and thus deviate greatly between the symmetric profile fits. In general, the intensity error in the Brillouin temperature spectrum arises primarily from baseline fluctuations (approximately ± 250 a.u.) and an approximately ± 2°C temperature error accounts for temperature ramping over 20 s.

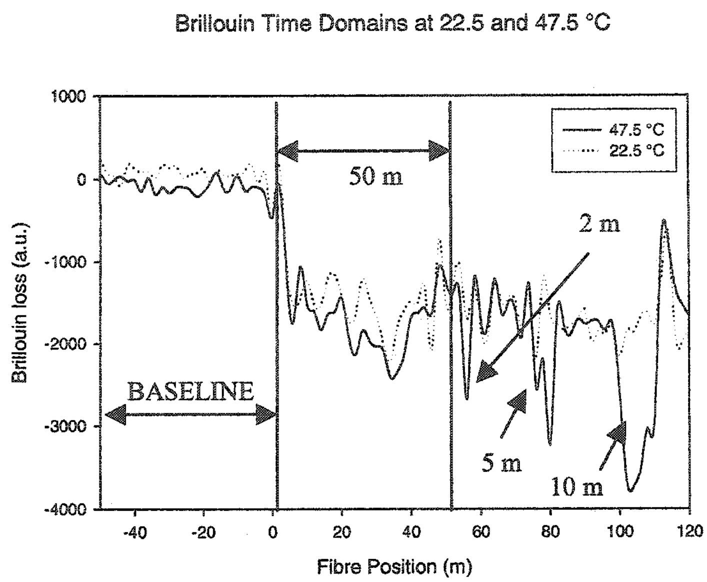

Figure 5.6: Brillouin Time-Domain revealing 2, 5, and 10 m regions, each separated by 20 m, starting approximately 50 m from the fibre end.

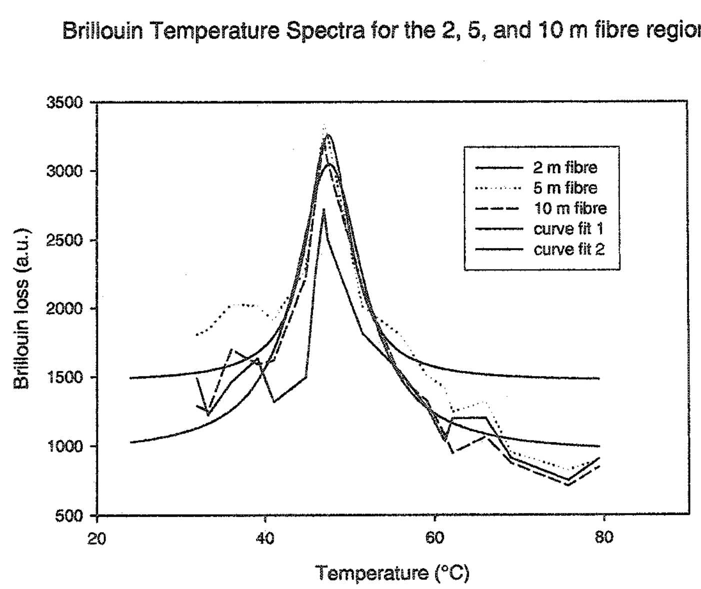

Figure 5.7: Brillouin temperature spectra from the 2, 5, and 10 m regions revealing asymmetries in the profile shape, likely arising from a non-uniform heating rate resulting in linewidth spreading.

5.3.3 Brillouin Linewidth and Power vs. Temperature

In this section, the Brillouin frequency linewidth and power relationships vs. temperature are acquired from the fibre in section 5.3.2 to determine their impact on the Brillouin temperature spectral shape. The experiment involves measuring a 30 m fibre section within a thermally insulated Styrofoam box while the remaining 2 km was left at room temperature. The temperature within the box was varied using embedded heating cords, which were attached to a temperature controller located outside the box. The temperature controller works by monitoring the environmental temperature using a thermocouple. When the environmental temperature dips below a preset temperature, the controller raises the voltage in the heating cords to raise the temperature. When the temperature exceeds the threshold temperature, no voltage is given to the heating cords, allowing them to cool slowly. In this experiment, 30 minutes of waiting time are required to acquire a stable temperature within the box since the controller responds in an oscillatory fashion until the desired temperature reaches equilibrium.

Four Brillouin spectra, representing four different temperature conditions, are given in Figure 5.8. Also shown are the corresponding Lorentzian and double linewidth pseudo-Voigt curve fits, which predict the Brillouin frequency peak very well. However, as in Chapter 4, the main differences between the fitting techniques are observed in the spectral tails. This is particularly evident in the 34.5 °C spectrum, where the long tail following the right side of the main Brillouin peak ranges from 12850 – 13000 MHz. The discrepancies arise because longer spectral tails provide more information about the Gaussian component in the profile. Conversely, the 69.9 °C spectrum is symmetric with shorter tails about the 12700-13000 MHz frequency range, and hence yields negligible differences between the curve fitting methods.

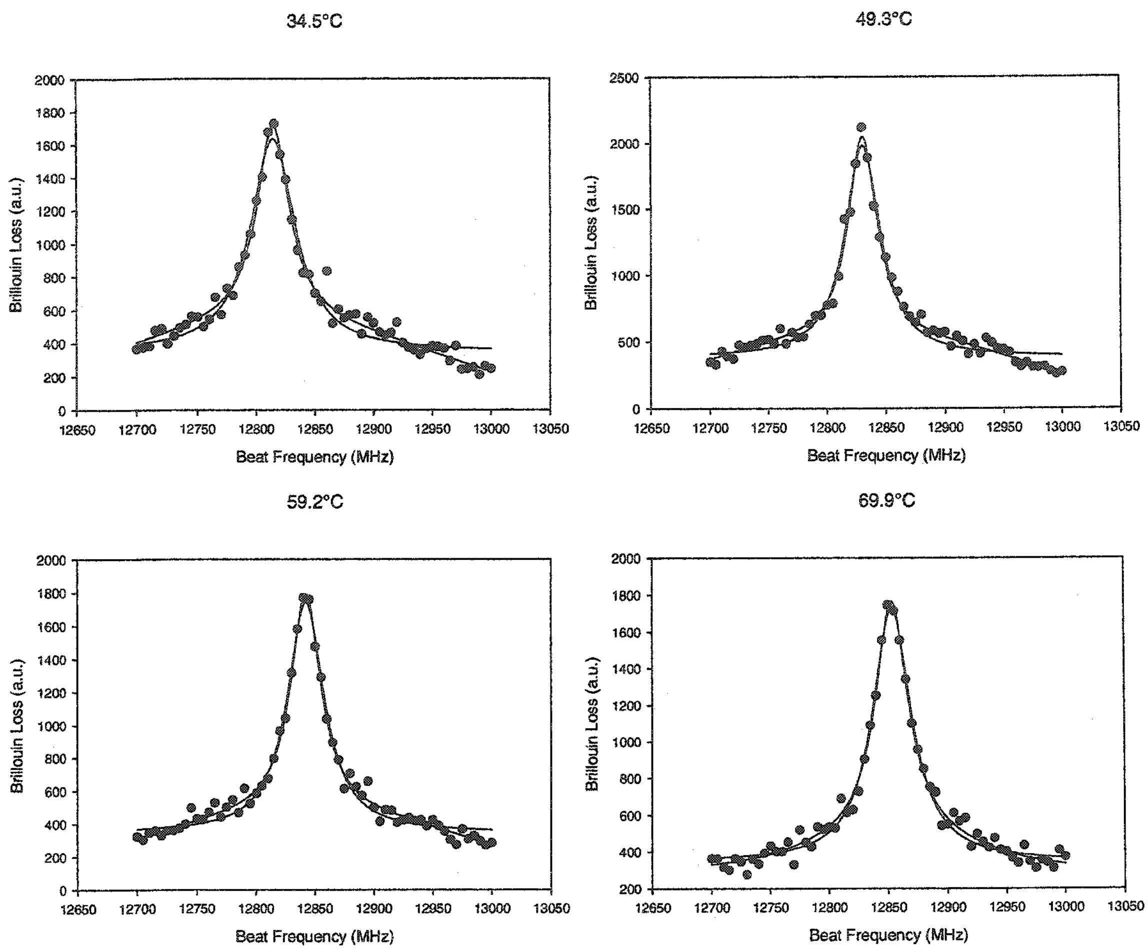

Figure 5.8: Evolution of the Brillouin frequency spectrum as a function of temperature. Each spectrum is shown with Lorentzian and double linewidth curve fitting methods.

These differences become apparent in measurements of Brillouin peak power, as shown in Figure 5.9. When the Brillouin peak loss calculation includes the offset term (P_0 in Equation 4.2), large differences between the fitting methods emerge, i.e. the predicted offset powers are very different. The double linewidth profile utilizes the behaviour of the spectral tails to determine the offset power whereas the upper spectral portion more largely influences the Lorentzian profile. Hence, the double linewidth profile overestimates the offset term due to the limited frequency range covered by the spectral tails, and the Lorentzian profile consistently underestimates the offset by attempting to satisfy a single linewidth form dominated by the upper spectral region. However, when the offset terms are accounted for, the true Brillouin peak power, defined as the maximum intensity from zero, is consistently determined by both profiles. The experimental peak loss values shown in Figure 5.9 are determined from the absolute maximum loss values collected by the detection system without manipulation. Like in Chapter 4, the double linewidth pseudo-Voigt profile provides slightly better predictions of the Brillouin peak loss. However, since the Brillouin peak loss varies within only ± 200 a.u. over the full temperature range, the Brillouin peak power must be treated as invariant with temperature.

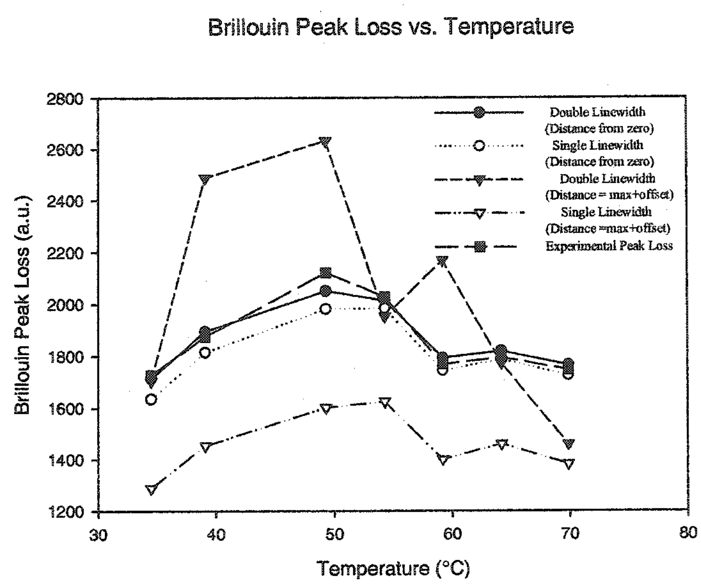

Figure 5.9: Plot of Brillouin peak loss vs. temperature. The "inverted triangle" curves show the maximum-to-minimum distances whereas the "circled" data represents the true maximum-to-zero Brillouin peak loss. Open and filled labels signify data obtained using the Lorentzian and double-linewidth curves respectively. The "square" label signifies experimental peak powers.

The different curve fitting methods yield negligible differences (Figure 5.10) in determining the linear relationship between Brillouin frequency and temperature given as

$$\nu_B = (12775.3 \pm 0.7) + (1.12 \pm 0.02)T \,. \tag{5.9}$$

Both The error values are determined from curve fitting errorAlthough the Brillouin frequency maintains a well-defined linear relationship vs. temperature in the transient regime, the Brillouin linewidth offers a very unclear relationship. As shown in Figure 5.10, the double linewidth fitting method predicts an essentially constant linewidth within ± 2 MHz. On the other hand, the Lorentzian curve predicts broader linewidths with an approximately ± 5 MHz spread, but an apparently more distinctive nonlinear relationship vs. temperature. However, since the frequency profiles are obtained in the transient regime ($\tau_{pulse} < 10ns$), they do not resemble a single uniform shape, and thus their shape cannot be represented accurately by the Lorentzian profile. Indeed, as shown in Figures 5.8 and 5.10b, the Brillouin linewidth is most overestimated by the Lorentzian profile for lower temperatures since it deviates more from the spectral tails. Hence, the linewidth must be treated as approximately constant with temperature.

By collecting the Brillouin intensities corresponding to specific beat frequencies from each of the seven Brillouin frequency spectra collected, and plotting them versus temperature, the Brillouin temperature spectra shown in Figure 5.11 are formed. For three beat frequencies, 12835, 12845, and 12850 MHz, the corresponding threshold temperatures are 53.3, 62.2, and 66.7°C respectively, based on Equation 5.9. When the Brillouin temperature spectra in Figure 5.11 are fit with a symmetric Lorentzian temperature spectrum (Equation 5.4), the results of curve fitting yield 53.2 ± 0.6, 61.7 ± 0.6, and 67 ± 3 °C. The theoretical and experimental threshold temperatures agree well within experimental error.

5.4 Summary

These experiments have successfully incorporated long fibre lengths (2 and 11 km) for monitoring the temperature variations of relatively small sensing lengths (2, 5, 10 and 30 m) using short spatial resolutions (0.2 and 2 m). The data acquisition time improves from minutes to seconds when the Brillouin intensity is monitored directly, rather than sweeping through a range of frequencies, thus allowing measurements to be made in real-time. The maximum Brillouin intensity corresponding to a threshold temperature, T_{th}, can be used to trigger an alarm signal for fire detection purposes. However, to accurately utilize Brillouin temperature spectra, the origins of spectral asymmetries must be well known. For instance, non-uniform heating rates can also artificially influence the Brillouin frequency- and hence temperature linewidths when the timeframe of temperature changes is shorter than the data acquisition time. Within experimental error, the Brillouin peak power and linewidth were found to experience no changes as a function of temperature within a short 30-70 °C temperature range.

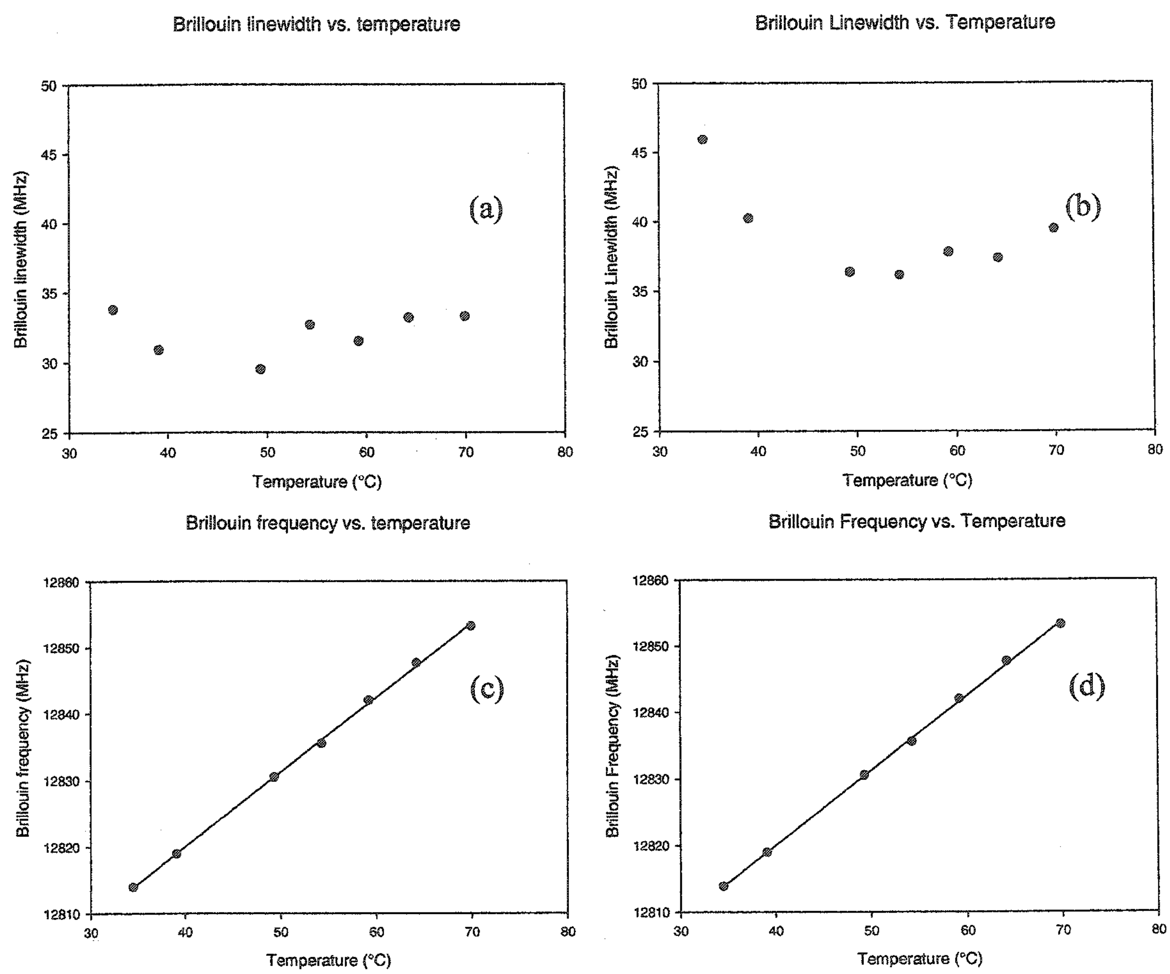

Figure 5.10: Brillouin linewidth (a, b) and frequency (c, d) relationships with temperature. The left and right columns represent results obtained from the double linewidth pseudo-Voigt and single linewidth Lorentzian curve fitting methods respectively.

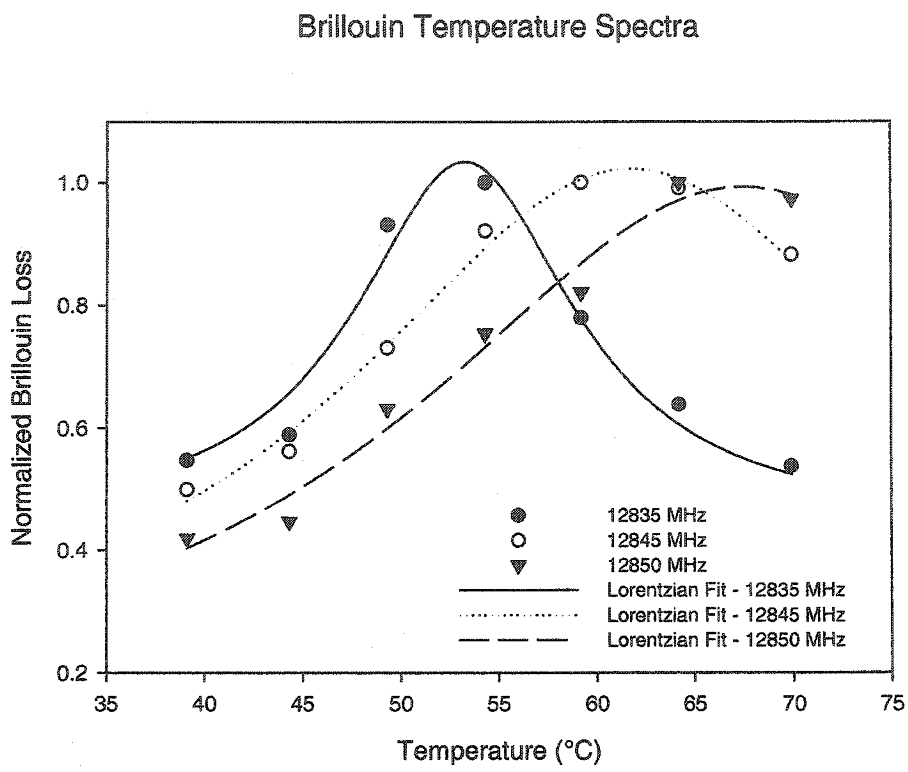

Figure 5.11: Brillouin temperature spectra generated from the Brillouin intensities of all seven temperatures at the 12835, 12845, and 12850 MHz beat frequencies.

Chapter 6: Pipeline Monitoring

This chapter presents longitudinal (axial) and circumferential (hoop) strain measurements of an internally pressurized 1.8 m steel end-capped pipe from an externally applied fibre optic distributed Brillouin sensor [Zou *et al.* 2003]. The locations of pre-embedded defective (cut-out) regions, comprising 50-60% of the inner wall, are found and distinguished by their corresponding strain-pressure data using a 13 cm spatial resolution. These results are quantified in terms of the fibre orientation, defect size and depth, and behaviour relative to unperturbed pipe sections.

6.1 Introduction

The dynamics of civil structures have been studied using various sensing technologies. In particular, distributed fibre optic Brillouin sensors have shown great promise in structural applications by providing very accurate measurements of both strain and temperature [DeMerchant *et al.* 2000, Bao *et al.* 2001]. The main goal of this study is to establish the Brillouin scattering system as a viable method for strain measurements of a pipeline and to investigate its capability in monitoring small defective regions normally caused by corrosion, erosion, or abrasion, which all inevitably cause pipeline failures. The abundance of pipeline failures over the past two decades has been astonishingly high, and according to the Alberta Energy and Utilities Board, corrosion fatigue was the most common cause (63%) of pipeline failures in Canada between 1980-1997 [Alberta Energy Report 1998].

In the field, pipeline integrity and disturbance lack reliable and durable monitoring techniques [Tapanes 2001]. Pipeline disturbances such as cracking, corrosion, and tampering are usually detected when the output flow is affected or when a severe impact is made on the surrounding environment. Unfortunately, the lack of information available on the type and location of pipeline faults has created inefficient and costly situations. For example, due to corrosion fatigue cracking, a 28-inch-diameter pipeline ruptured and released approximately 564,000 gallons of gasoline on March 9, 2000, in Greenville, Texas, USA, resulting in a damage and clean-up cost of $18,000,000 [USA Safety Report 2001].

Hence, there is a desperate need for a real-time structural health monitoring system that can intelligently monitor the integrity of pipelines.

One of the major difficulties of monitoring pipelines stems from the fact that the pipeline length can have tens of meters to hundreds of kilometres buried underground. Conventional conductive sensors encounter difficulties surviving the surrounding environments and encounter electrical noise problems. Furthermore, numerous such point-sensing devices are required to adequately monitor the health of long pipelines at a substantial cost. Fortunately, the advent of optical fibre technology utilizing low-cost optical fibre communication cables enables distributed structural health monitoring of pipelines.

6.2 Stress and Strain Analyses of a Pipe with Internal Pressure

When an end-capped hollow pipe experiences an internal pressure due to fluids or gases, three principal geometrical stresses (illustrated in Figure 6.1) are imposed on the pipe structure:

i) hoop ii) radial iii) axial

All stresses act to deform the structure with a rate dependent on its material properties (Young's Modulus, Poisson's Ratio), geometrical dimensions (radii, thickness, length), and the boundary conditions at the ends of the pipe (end-cap geometry: flat, round; attached by: bolting, welding), which can often depend on the quality of end-cap construction.

The three principal stresses (hoop, radial, axial) on a thick-walled end-capped cylindrical pressure vessel subjected to internal pressure are calculated using Lamé's solutions [Budynas 1999a, Barber 2001]:

$$\sigma_{h,r} = \frac{R_i^2 p}{R_o^2 - R_i^2}\left(1 \pm \frac{R_o^2}{r^2}\right), \tag{6.1a}$$

$$\sigma_z = \frac{R_i^2 p}{R_o^2 - R_i^2}, \tag{6.1b}$$

where p, R_i, R_o and r are internal pressure, internal and external radii, and the polar coordinate ($R_i \le r \le R_o$) of the pipe, respectively. In Equation 6.1a, the hoop and radial stresses (σ_h *and* σ_r) correspond to the + and – solutions respectively, and the axial stress (Equation 6.1b) is independent of the radial coordinate. At the surface of the cylinder ($r = R_o$), $\sigma_h = 2\sigma_z$ and the radial stress falls to zero.

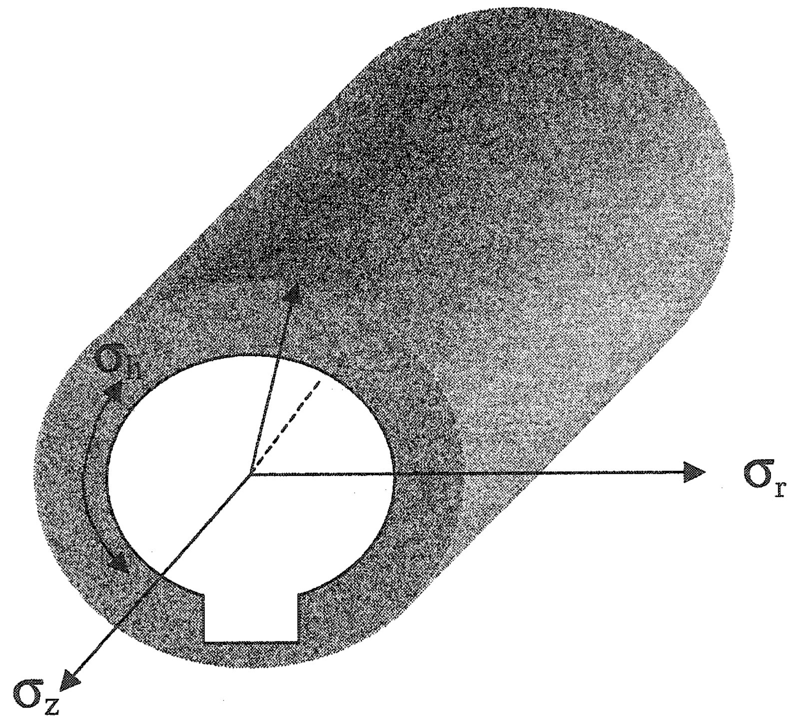

Figure 6.1: Principal stress directions imposed on the pipe. Due to cylindrical symmetry, no shear stresses exist.

The validity of $\sigma_h = 2\sigma_z$ can be more readily understood by considering the thin-wall approximation of the wall reactions, which agrees with reality within 5% assuming R/t<10, where R and t are the internal radius and wall thickness respectively. Considering the force equilibrium $(\Sigma F = 0)$ diagrams shown in Figures 6.2 and 6.3, the axial and hoop stresses are derived in the following manner:

$$F = \sigma A$$

$$p\pi r_i^2 = \sigma_z \pi \left(r_0^2 - r_i^2\right)$$

$$p\pi r_i^2 = \sigma_z \pi (r_0 - r_i)(r_0 + r_i)$$

Assuming $r_0 \cong r_i$:

$$p\pi r_i^2 = \sigma_z \pi t 2r_i$$

$$\sigma_z = \frac{pr_i}{2t} \tag{6.2}$$

Similarly, the hoop stress is:

$$p2r_iL = 2\sigma_h tL$$

$$\sigma_h = \frac{pr_i}{t} \tag{6.3}$$

Knowing the hoop and axial stresses, the hoop and axial strains at the outside surface are calculated by the following equations:

$$\varepsilon_h = \frac{1}{E}(\sigma_h - \upsilon\sigma_a), \tag{6.4}$$

$$\varepsilon_a = \frac{1}{E}(\sigma_a - \upsilon\sigma_h), \tag{6.5}$$

where ν and E are Poisson's ratio and Young's modulus respectively. Substituting Equations 6.1a and 6.1b into Equations 6.4 and 6.5 yields linear relationships between strain and pressure, which are valid within the elastic regime of the material.

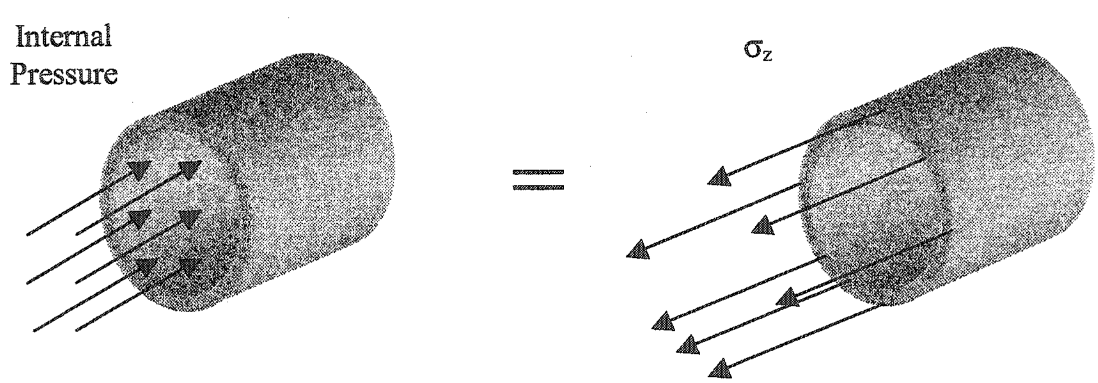

Figure 6.2: Longitudinal force equilibrium. Internal pressure acts on $A = \pi r^2$ whereas σ_z acts on $A = 2\pi r \times t$. Equating the forces yields $\sigma_z = \frac{pr}{2t}$.

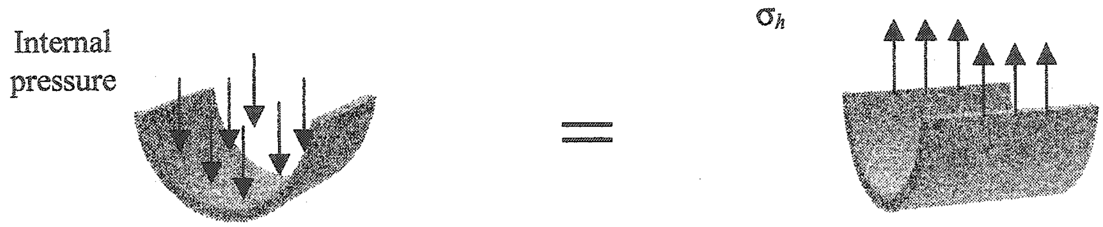

Figure 6.3: Circumferential force equilibrium. The internal pressure applies a force vertically onto the cross section of the pipe. The pipe responds with a stress σ_h to maintain equilibrium.

The given theory applies to sections of a uniform end-capped pipe located far from the distal ends since the pressure dynamics near the double-capped boundaries are generally far more complex. Such complexities generally arise from regions exhibiting high *stress concentrations*, which result from discontinuities in continuum and contact forces [Budynas 1999b]. Discontinuities in continuum are geometrical structural variations such as holes, sharp corners, and material flaws, which alter the flow of stress distributions within a structure. Contact forces occur when two or more structural pieces join to form a structure, and specifically emerge at the corresponding intersections of contact possibly resulting in local deformation or buckling. These effects are pronounced when the stress distributions in each assembled component are different along a common direction (e.g. hoop, axial). Hence, in pressure vessels, the end-caps used to contain compressed air are normally designed to endure stress distributions equivalent to those experienced by the main body of the vessel. Since the pipeline analyzed here encompasses several abruptly changing cutout regions and large 42 kg flat end-caps, stress concentrations have become an important consideration. However, for industrial pipes extending over several kilometres, the effect of end-caps is non-existent.

6.3 Experimental Procedures and Fibre Installation

6.3.1 Pipeline Description and Procedures

To simulate the structural degradation in pipes, rectangular indentations were entrenched within the inner wall of a steel pipe constructed in the CANMET Materials Technology Laboratory in Ottawa, Ontario. The pipeline schematic and material specifications are shown in Figure 6.4 and Table 6.1.

The pipe was pressurized using argon gas, and 90% filled with distilled water, which has a reduced compressibility compared with that of air. At predetermined locations along its inner wall, structural cutouts compromising 50 and 60% of the wall (Figure 6.5a) simulated the condition where a corroded pipeline has approached its threshold for replacement (50%). For comparison, the behaviour of 60% cutouts will determine whether the Brillouin sensor system could differentiate the strain responses of pipe regions having different wall thickness. The locations and dimensions of the cutouts are given in Table 6.2.

6.3.2 Installation of Sensing Fibres

A 30 m acrylate buffered SMF-28 optical fibre monitored both the laboratory temperature conditions and the strain distributions along the pipe. To prepare the pipe for fibre installation, coarse sandpaper was used to remove surface irregularities caused by excess welding and thus created a smooth, uniform surface around its external circumference. Optical fibres were then pre-strained and mounted externally on the pipe to monitor the strain changes at its outer surface, and were secured using a special low-viscosity glue made by Mastercraft, which required approximately 3 hours to dry. Based on practical experience, the type and amount of glue applied onto a fibre is found to have a significant impact on its strain measurements. In particular, the strain and thermal expansion coefficients of the glue do not necessarily match those of fibres and the material under examination. Consequently, a low-viscosity glue ensured that only a thin layer remained on the fibre's top surface, while the residual glue surrounded the fibre, thus creating the fibre-pipe interface (Figure 6.6). To avoid signal cross talk and additional noise resulting from fibre overlap, two separate experiments were conducted to measure the axial (Figure 6.5b) and hoop (Figure 6.5c) strains. Three thermocouples monitored the pipe temperature at various locations (Figures 6.5b and 6.5c) to monitor temperature fluctuations.

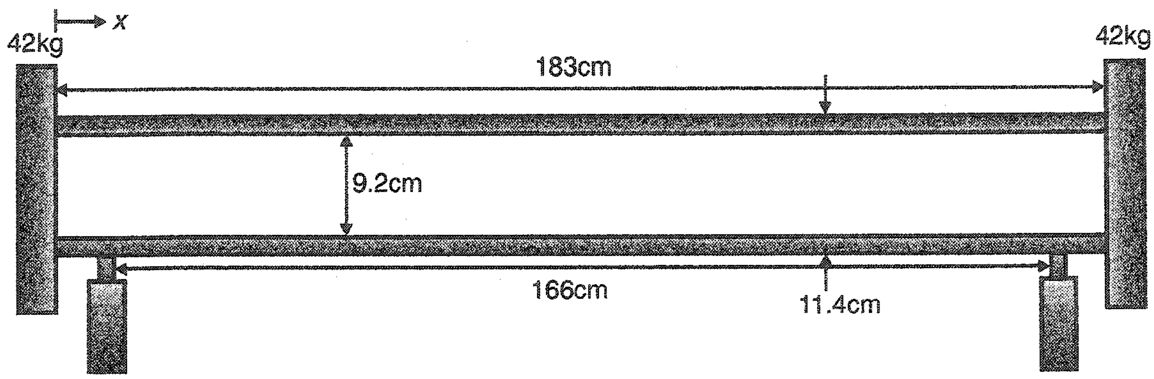

Figure 6.4: Schematic diagram of the steel pipe

Poisson's Ratio	Young's Modulus	Length	Outer diameter	Wall thickness
0.3	200 GPa (30 x 10^6 psi)	1.83 m	0.114 m	0.011 m

Table 6.1: Material specifications of the steel pipe

Defect	Location (o'clock)	Reduced thickness (%)	Width (cm)	Length (cm)
A	5-7	60	5.3	61
C	7	50	1.3	10
D	5	60	1.3	10

Table 6.2: Parameters of defects

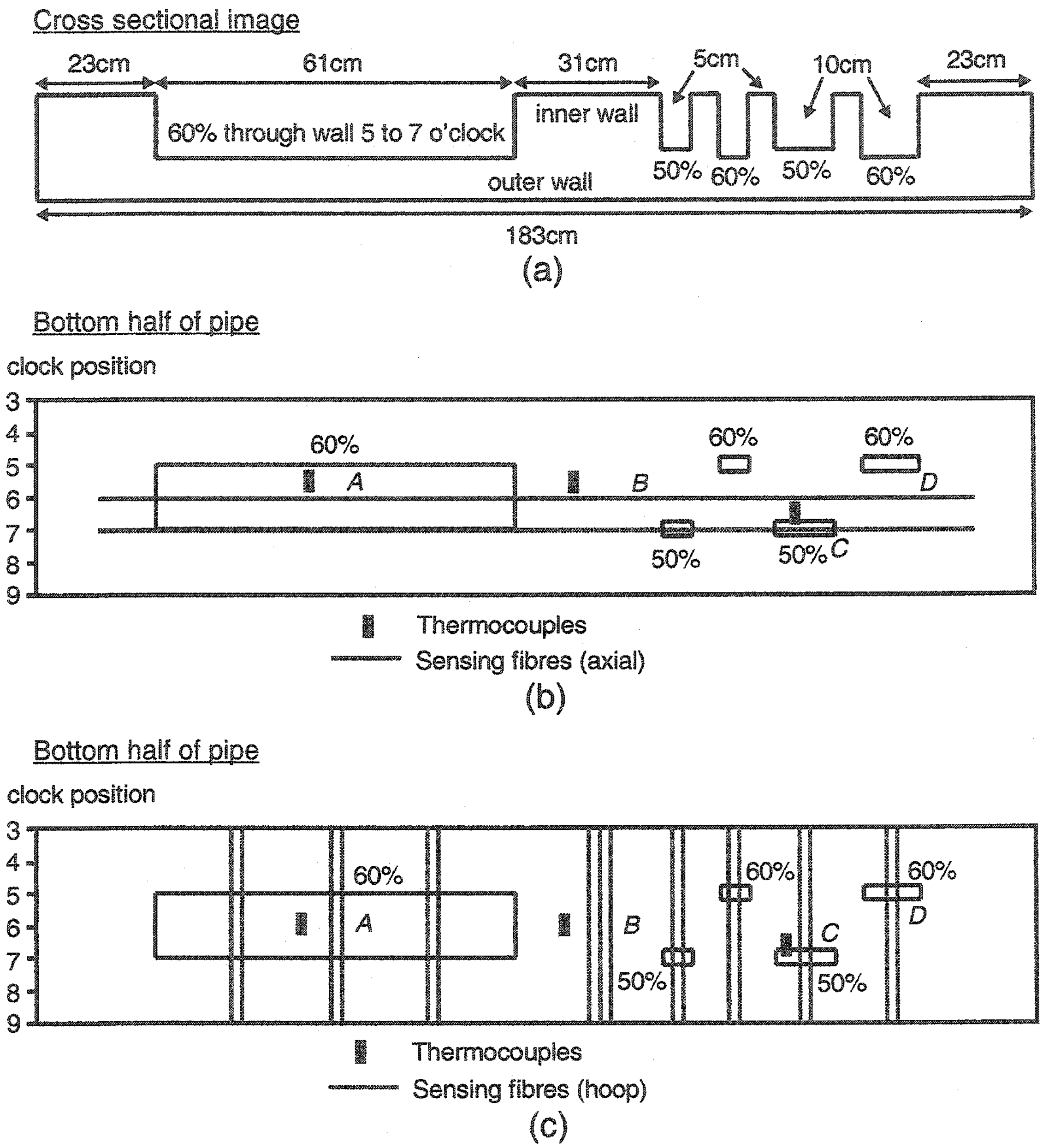

Figure 6.5: (a) Schematic diagram of the distribution of cutouts, and fibre installation in the axial (b) and hoop (c) configurations. The cutout dimensions are given in Table 6.2.

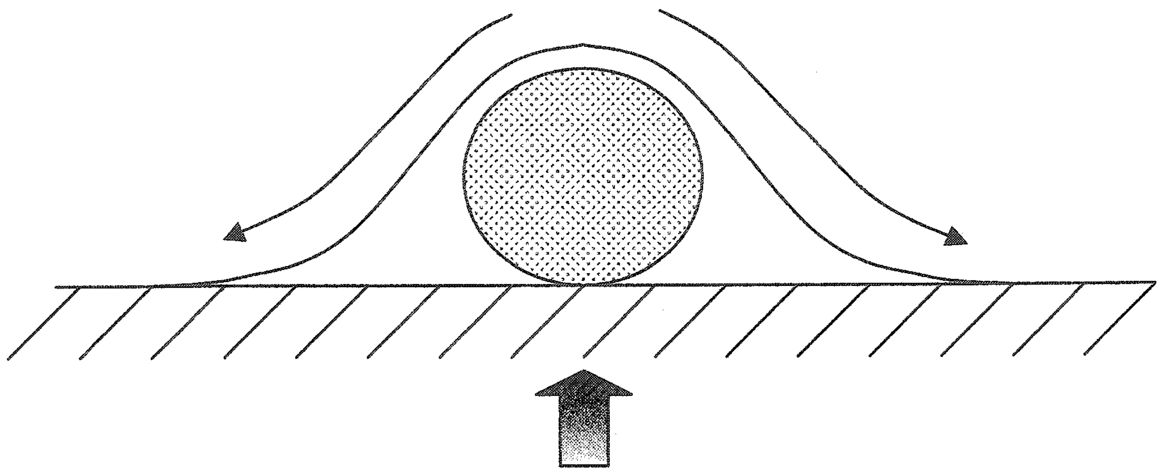

Figure 6.6: Utilization of low-viscosity glue ensures that a thin layer of glue covers and secures the optical fibre to the pipe wall.

6.3.3 Data Acquisition and Analysis

Brillouin loss spectra were acquired every 5 cm along a 30 m optical fibre using the experimental apparatus described in Chapter 4. The 5 cm/S (cm/sample) data acquisition rate is achieved using a 2 GS/s data acquisition system. Time domain waveforms required 8000 averages to minimize the noise, which would otherwise overwhelm the signal from the short 1.3-ns pulse duration used to provide a 13-cm spatial resolution. The electro-optic modulator operated at a 19 dB extinction ratio and released a 70 mW peak pulse power, which counter-propagated with a 4 mW CW pump power. For data analysis, the pseudo-Voigt function described in Chapter 4 was used for fitting the Brillouin spectral profiles spanning a 12700-13000 MHz frequency range. A 2 MHz frequency step size was chosen to ensure all data was collected within the allocated timeframe while maximizing accuracy of curve fitting. This procedure was repeated for 50 psi pressure increments from 0 to 500 psi. Finally, the strain information was determined from the Brillouin frequency deviations from the 0 psi condition, which were then multiplied by the 17.09 $\mu\varepsilon$/MHz strain coefficient (C_ε in Equation 2.16) [Zeng 2003] obtained by calibration.

6.4 Results and Discussion

6.4.1 Axial Strain Measurement

The axial strain distribution along the pipe was measured using the configuration shown in Figure 6.5b. The large defective region *A* is located between 23 and 84 cm and the remaining pipe length at the 6 o'clock (bottom) position is unperturbed. The strain distribution along the longitudinal direction of the pipe under a 200 psi internal pressure is presented in Figure 6.7. The maximum (46 $\mu\varepsilon$) and minimum strains (14 $\mu\varepsilon$) occur near the middle of the defective and unperturbed regions, respectively. Since this 32 $\mu\varepsilon$ difference is outside the experimental error range (~15 $\mu\varepsilon$ based on standard deviation) and therefore results from the wall thinning, the capability of this system in distinguishing defective and unperturbed regions is successfully demonstrated.

In the absence of stress concentrations from end-caps or defects, a fibre traversing the bottom of the pipe experiences a uniform tension along its length due to the expansion of the pipe under internal pressure through Equation 6.5. Furthermore, the magnitude of this tension increases with decreasing wall thickness (Equation 6.1b or 6.2). This explains the strain differences quoted above. However, the evolution from one strain condition to another does not arise from simple analytical theory, but rather from the behaviour of the boundaries separating them. For example, as the fibre traverses toward the edge between the defective and unperturbed regions, it experiences a gradually lower tension due to the restrictive behaviour of the boundary. Like balloons, the bulge occurs farthest from the boundaries where the "torque" is greatest. In addition, when the fibre position is within 13 cm of the edge, the corresponding Brillouin signal represents an average of the defective and unperturbed regions, yielding overall reduced strains. However, the abrupt strain changes near the pipe ends occur due to stress concentrations from the local end-caps. In general, such strains depend sensitively on proximity to the cap, end-cap size and type, and overall pipe design. Since this pipe is asymmetric in terms of the defective region distribution, quantification of the strain distributions requires sophisticated finite element analysis techniques involving complex shell analyses. Furthermore, such analyses should account for the forces occurring from the supporting frame, which is currently beyond the scope of this work.

As mentioned earlier, the strain-pressure relationship of a uniform pipe operating within its elastic regime remains linear. Hence, the subsequent analysis is based on strain-pressure slopes, which indicate the extent of pipe deformation for given pressure changes. As shown in Figure 6.8, the strain-pressure slopes of the defective region exceed those within the unperturbed region. Furthermore, the strain-pressure slope maximizes at 0.48 $\mu\varepsilon$/psi in the middle and decreases toward the edges of the defect. Hence, the strain bulge occurs in the middle of the defect, and increases most rapidly there for a given pressure change. However, a small local maximum arises near the edge, located at 84 cm, due to the non-continuous boundary condition arising from a local stress concentration at the edge. In addition, reduced strain measurements near the defect boundary generally occur due to the overlapping 13 cm pulse, which acquires an average strain from both regions. The strain-pressure slope remains constant at 0.16 $\mu\varepsilon$/psi within the experimental error near the middle of the unperturbed region, as expected, because the influence of boundaries is very small.

The strain-pressure behaviours of unperturbed and two defective regions are shown in Figure 6.9. As expected, deeper defects exhibit larger strain-pressure slopes due to decreased wall thickness. Since the strain-pressure slope of region *B* is less than those of regions *A* and *C*, pre-embedded defects comprising 50% and 60% of reduced inner wall thickness have been discriminated from the corresponding axial strain measurements.

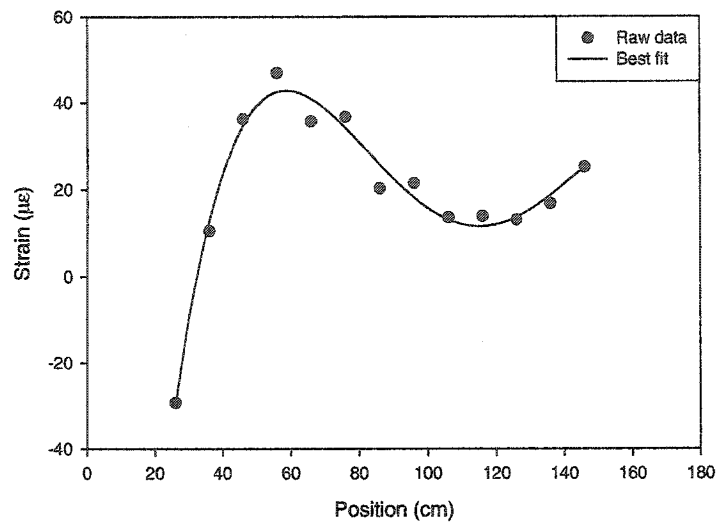

Figure 6.7: Axial strain distribution through cutout region *A* and unperturbed region *B*. The strain difference between the maximum from the defect region and the minimum from the unperturbed region is 30 με. The "best fit" line simply represents a trend line for the data.

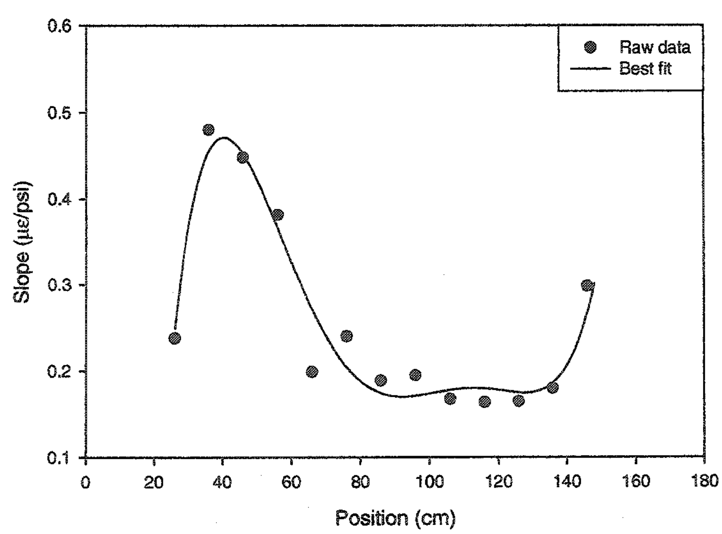

Figure 6.8: Axial strain-pressure slope distribution through cutout *A* and unperturbed region *B*. The cutout region between 23-84 cm exhibits larger strain-pressure slopes. The "best fit" line simply represents a trend line for the data.

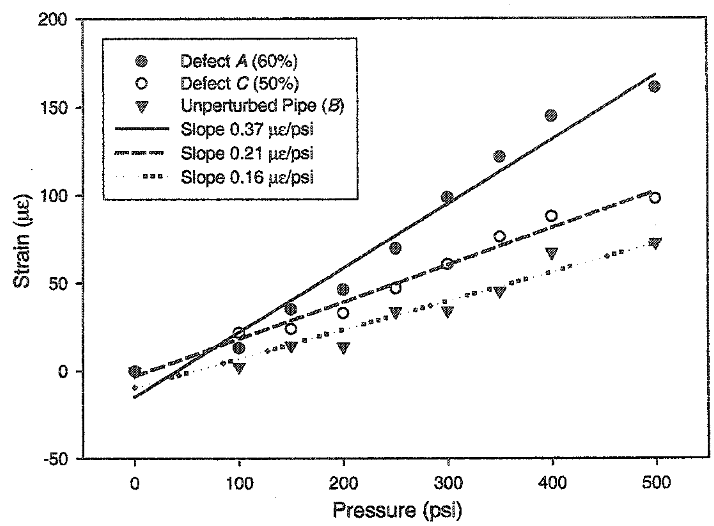

Figure 6.9: Axial strain-pressure slopes from regions *A*, *B*, and *C*. Larger strain-pressure slopes occur in larger and deeper cutout regions.

6.4.2 Hoop Strain Measurement

Distributed hoop strain measurements were obtained using the fibre configuration shown in Figure 6.5c. The strain distributions for 300 and 500 psi internal pressures, along with their corresponding strain-pressure slope distribution around one pipe circumference encompassing defective region *A*, are shown in Figure 6.10. Since the minimum and maximum slopes of 0.21 and 0.27 με/psi are spaced approximately 180° apart, and are outside the experimental error range, the defective and unperturbed regions are differentiated. The 180° spacing is "approximate" since data points were collected every 5 cm and therefore do not exactly overlap after half a pipe circumference, as its 17.94 cm value is not an integer multiple of 5 cm. The slope differences indicate a larger deformation of the defective region relative to that of the unperturbed region due to the reduced wall thickness. Furthermore, as shown in Figure 6.11, the strain-pressure relationships of the defective and unperturbed regions are linear within a 15 με standard deviation.

Another method of distinguishing defective regions is by determining their behaviour at different positions along the pipe length. This can be achieved by determining the average of all strain-pressure slopes around a single fibre loop, and comparing this with other averages along the pipe. The average of all strain-pressure slopes obtained around one fibre loop is a good indication of the arc length of the defective region. Hence, for equivalent penetration depths (60% cutout), the average strain slopes of 0.24 and 0.18 $\mu\varepsilon$/psi for fibre loops wrapping defective regions A and D indicate the dominance of a larger defective region A (5.3 cm) over the smaller region D (1.3 cm) on the net strain distribution around one fibre loop.

To compare defective regions having the same arc length but different penetration depths, measurements of their strain-pressure slopes directly indicates the effect of wall penetration. As shown in Figure 6.12, the strain-pressure slopes of defective regions C and D are 0.18 and 0.21 $\mu\varepsilon$/psi, which correspond to 50 and 60% depleted walls respectively. As expected, a larger strain-pressure slope indicates a thinner pipe wall. Again, the unperturbed wall in both fibre loops experiences a constant strain-pressure slope of 0.15 $\mu\varepsilon$/psi.

The hoop strain-pressure slopes quoted above do not represent the exact strain-pressure values since the pulse duration (0.13 m) always exceeds the defective width (0.013 and 0.053 m) and hence carries the strain behaviour from both the unperturbed and defective regions. Hence, the hoop strain-pressure slope increases with defect width as well as depth. Despite having different wall thicknesses, the smaller defects *C* and *D* (1.3 cm wide) did not affect the neighbouring unperturbed regions significantly. Consequently, the corresponding unperturbed regions (12 o'clock positions) maintained a 0.15 $\mu\varepsilon$/psi strain-pressure slope. An increased slope from the unperturbed region corresponding to large defect *A* (0.21 $\mu\varepsilon$/psi) likely arose from a larger deformation from the large defect.

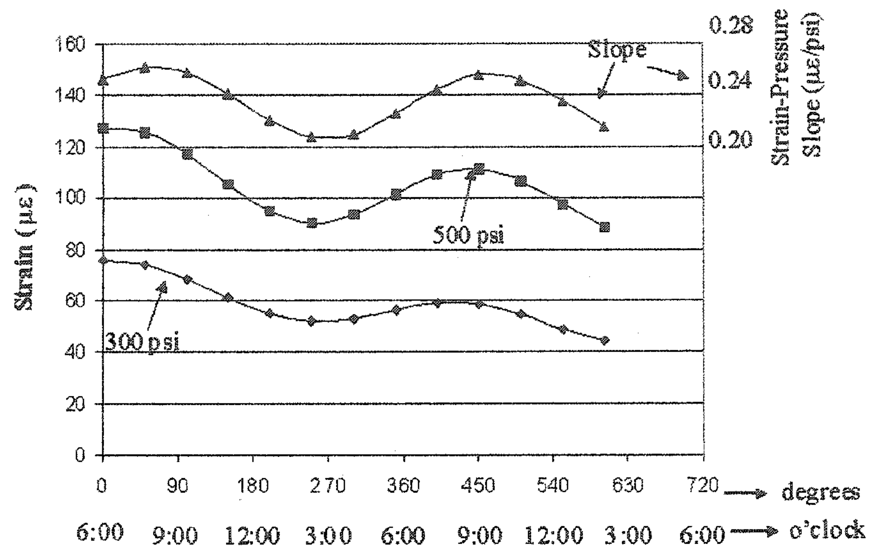

Figure 6.10: Hoop strain distribution along the circumference of large defect *A*. Maximum strain-pressure slopes, occurring once every 360°, correspond to fibre positions closest to the centre of the defective region.

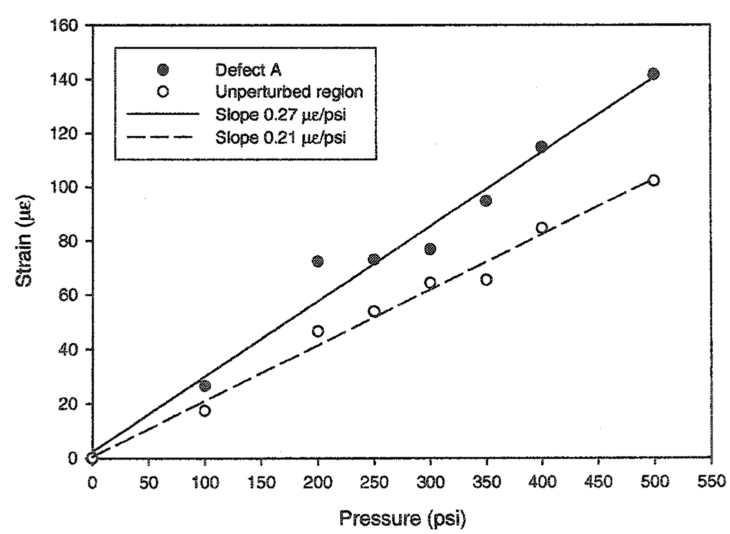

Figure 6.11: Hoop strain-pressure relationships from a pipe circumference encompassing large defect *A*. The maximum (0.27 με/psi) and minimum (0.21 με/psi) slopes correspond to fibre positions closest and farthest from the centre of the defective region.

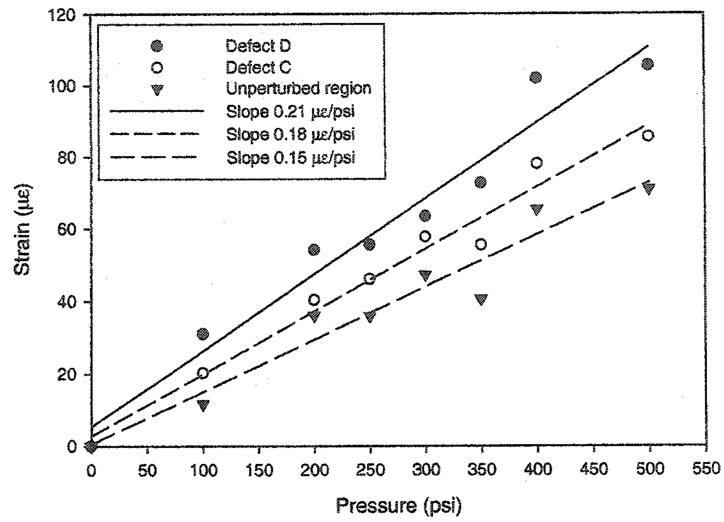

Figure 6.12: Strain-pressure slopes corresponding to defective regions C (50% cutout) and D (60% cutout), having 0.18 and 0.21 με/psi slopes respectively. Both exceed the unperturbed (12 o'clock) slope of 0.15 με/psi.

6.5 Error Analysis

There are three main experimental error sources inherent in strain measurements: Temperature- and power fluctuations, and curve fitting efficiency. The controlled laboratory environment allowed for minimization of temperature fluctuations. In particular, based on the information provided by attached thermocouples, the temperature deviated less than ± 0.2 °C or ± 5 με of thermal strain between trial runs. This error is systematic since no temperature fluctuations occurred during the data acquisition time.

The error from power fluctuations affects the minimum detectable Brillouin frequency shift through [Horiguchi *et al.* 1995]

$$\delta \nu_B = \frac{\Delta \nu_B}{\sqrt{2}(SNR)^{1/4}}, \tag{6.6}$$

where $\Delta \nu_B$ and SNR are the Brillouin linewidth and signal-to-noise ratio respectively. Hence, any power fluctuations varying the signal level will degrade the SNR, and increase the minimum detectable Brillouin frequency (strain) change.

The sources of power fluctuations are twofold. First, any fluctuation in the laser power affects the Brillouin interactions along the fibre, especially when using short pulses having low energy. This problem is handled by: 1) increasing the number of waveform averaging, and thus the polarization scrambling time, to allow a stable average laser interaction to overwhelm any polarization noise; and 2) by attentively monitoring the leakage power emerging from the EOM.

As previously mentioned, 8000 waveform averages generated stable probe-pump Brillouin interactions, and allowed the rather slow polarization controller (a few seconds) to fully scramble the polarization. To ensure that 8000 averages was a sufficient value, two separate experiments under equivalent conditions but different averaging values (8000 and 12000) determined the impact of averaging on the Brillouin spectrum. The corresponding Brillouin spectra shown in Figure 6.13 reveal that experimental accuracy has asymptotically approached a maximum level, i.e. the Brillouin spectra have negligible differences. Therefore, 8000 averages adequately minimized polarization noise and laser fluctuations, even for a 1.3 ns pulse duration, and no improvement was made by increasing the number of waveform averages (12000) and data acquisition time.

The constant leakage power level entering the fibre was maintained by recalibrating the system between trial runs. For instance, after a trial run, any thermal drift experienced by the EOM would cause it to begin the following run at a shifted bias level. By recalibrating each time, the system is always aware of the specified bias level, so although a new calibration shifts the sine curve relation between bias level and input driving voltage (Equations 3.2 and 3.5), only the input driving voltage varies in response to the desired bias level. Careful monitoring of this leakage power allowed for a minimization of leakage power fluctuations.

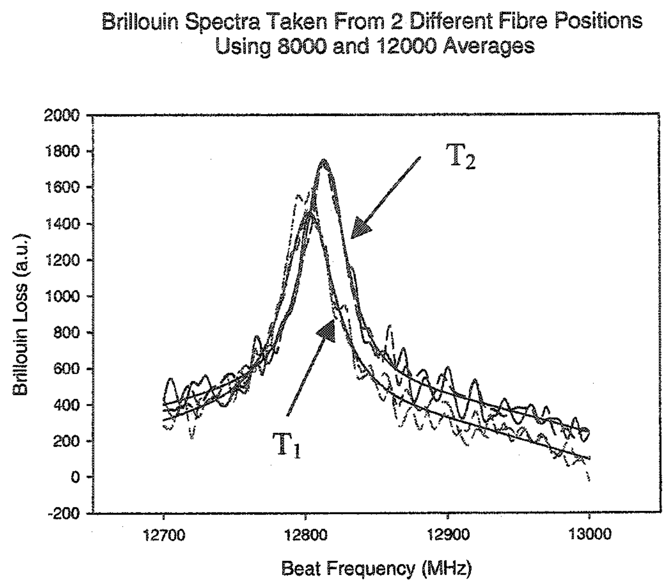

Figure 6.13: Brillouin frequency spectra from two different fibre positions at different temperature conditions (T_1 and T_2). Regardless of fibre position or temperature condition, the 8000 and 12000 averaged data yield nearly identical Brillouin spectra.

The second power fluctuation source arises from Brillouin interactions occurring before and after the desired interaction location, which affect its Brillouin spectrum as discussed in Chapter 4. When the pipe pressure changes, the laser interactions occurring in strained fibre regions depend on the degree of resonance with the incoming light beams. Hence, the laser powers available for Brillouin interaction within a specific fibre region depend on the temperature and strain conditions within adjacent fibre sections. As well, the possibility of additional Brillouin frequencies emerging from adjacent fibre sections may become a reality. By examining the Brillouin spectra from various fibre regions, this effect can be determined.

As evidence of such cross talk, an asymmetric peak lying at 12770 MHz exists in Brillouin spectra from strained fibre sections (241 ns) as shown in Figure 6.14. This peak is not apparent in Brillouin spectra from loose fibre regions (202 and 354 ns), making it either a property of strained fibre or cross talk from loose fibres. Since no additional peaks of this nature occur within the strained fibre spectrum, this peak likely emerges as cross talk from the loose fibre. Furthermore, as shown in Figure 6.15, when Brillouin spectra are acquired for different temperature conditions from the centre of a 2 m sensing fibre using a 20 cm spatial resolution, cross talk emerging at approximately 12790 MHz occurs due to overshooting of the Brillouin signal. Near the intersection between two fibres having very different environmental conditions, the Brillouin intensity changes very rapidly. Unfortunately, due to bandwidth limitations, the detection system cannot pick-up such fast changes and thus the time domain trace artificially shifts down, and often drops below the baseline level (where Brillouin loss = 0) yielding negative Brillouin loss values [Smith 1999]. This *oscilloscope overshooting* explains the initial drop in the Brillouin spectra (Figure 6.15) at approximately 12770 MHz.

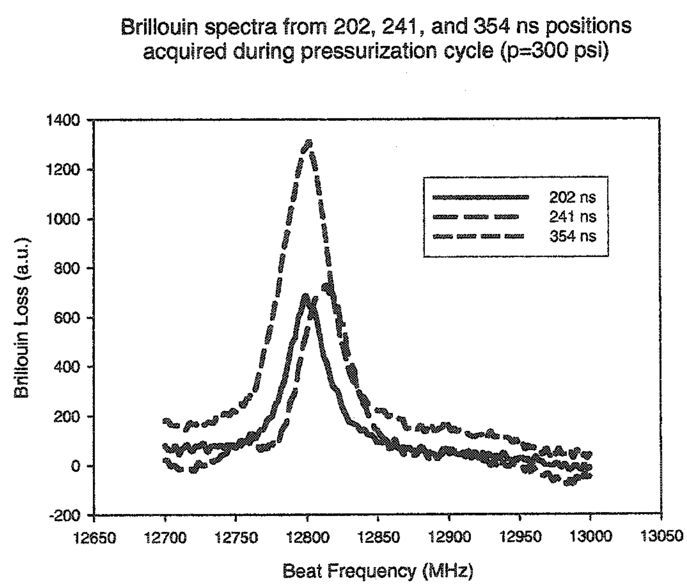

Figure 6.14: Brillouin spectra from two unattached (loose) fibre sections (202 and 354 ns, representing lead fibres before and after the pipe) and one strained fibre section (241 ns). The strained fibre spectrum contains a frequency peak at 12770 MHz, which likely originates as cross talk from the loose fibre region.

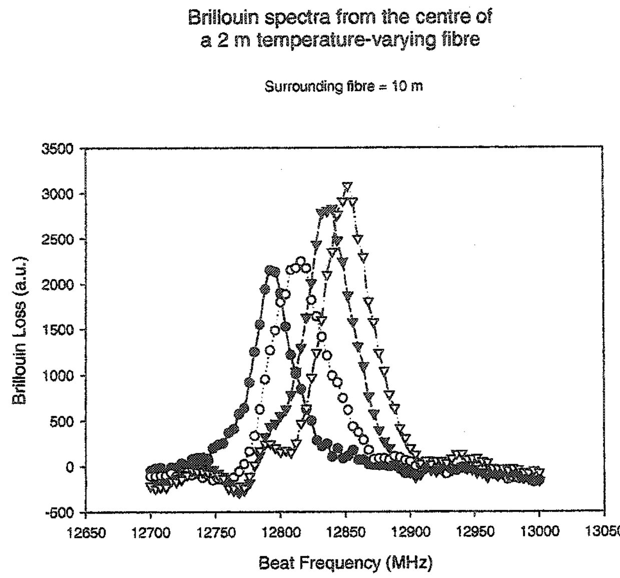

Figure 6.15: Brillouin spectra from the centre of a 2 m temperature varying fibre for different temperature conditions. Cross-talk emerges as an additional peak at approximately 12790 MHz – the Brillouin frequency of the 10 m room-temperature fibre. The spatial resolution was 20 cm.

Figures 6.16 and 6.17 reveal additional satellite peaks emerging at 12900 and 12930 MHz, which likely originate from the loose and strained fibres respectively. Brown has found that such satellite peaks experience no relative frequency shifts under both temperature and strain changes [Brown 2000], i.e. their frequency spacing from the main Brillouin peak is always constant (~ 70-100 MHz). This finding is consistent with peaks observed here, where 12900 and 12930 MHz peaks correspond to frequencies 100 MHz greater than the loose (~ 12800 MHz) and strained (~ 12830 MHz) fibre regions. Since both Figures 6.16 and 6.17 represent two separate loose fibre regions, the 12930 MHz peak arises from cross talk. Indeed, Figure 6.17 reveals a spreading of the satellite peak within a 12900-12940 MHz range perhaps indicating the level of cross talk from intermediate pipe sections.

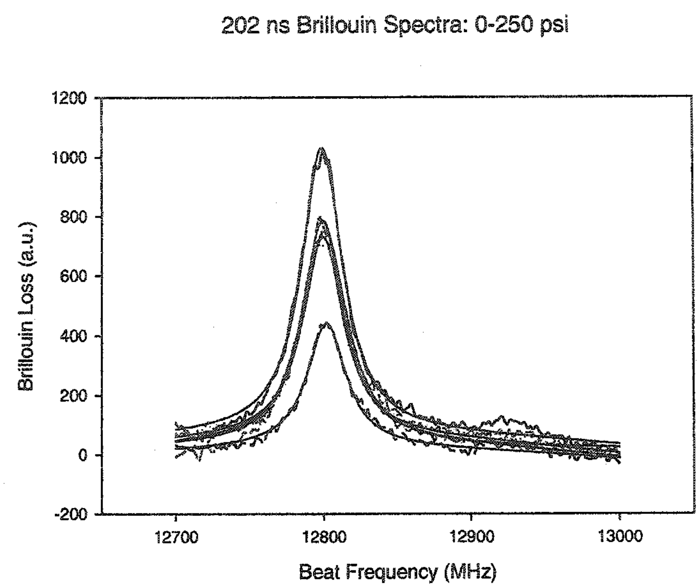

Figure 6.16: Brillouin spectra (and respective curve fits) from the loose fibre section, which leads from the pulsed laser (before the pipe). Each spectrum corresponds to a specific pressure within the 0-250 psi range.

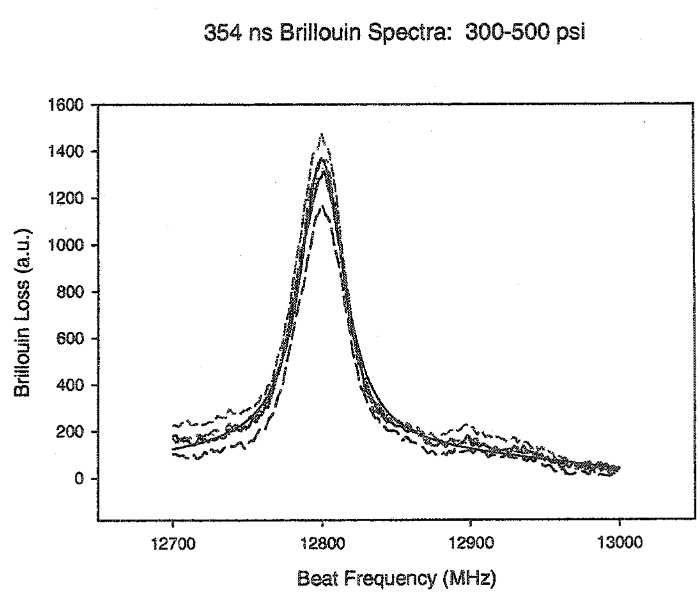

Figure 6.17: Brillouin spectra (and a representative curve fit) from a loose fibre section leading from the pump laser (after the pipe). Each spectrum corresponds to a specific pressure within the 300-500 psi range.

In the hoop strain results, the 150 and 450-psi data are omitted. For the 150-psi spectrum, the power fluctuation created a low SNR (see bottom spectrum, Figure 6.16), and larger strain error through Equation 6.6. Hence, any additional asymmetries (e.g. satellite peak) impose a larger influence on the peak-fitting results. However, as shown in Figure 6.18, zooming on the Brillouin peak and ignoring the remaining spectrum improves the frequency measurement by 1-2 MHz (17-34 $\mu\varepsilon$). The 450-psi omission is justified by examining its Brillouin spectrum, as shown in Figure 6.19. A heavy intensity asymmetry favours frequencies leftward from the main Brillouin peak, thereby shifting the fitted curve to the left. This asymmetry likely arises from pressure instability within the pipe. Between trial runs, the pipe pressure was increased 50 psi and then allocated a few minutes to establish static equilibrium with its newly pressurized environment. If the pipe continued to extend during the trial run, the frequency spectrum would spread asymmetrically depending on how fast the pipe reached equilibrium. As an additional possible factor, after all trial runs were completed, the pipe had leaked 40-50 psi while held at constant internal pressure over a period of several hours due to pressure absorption of the argon-water combination within the pipe.

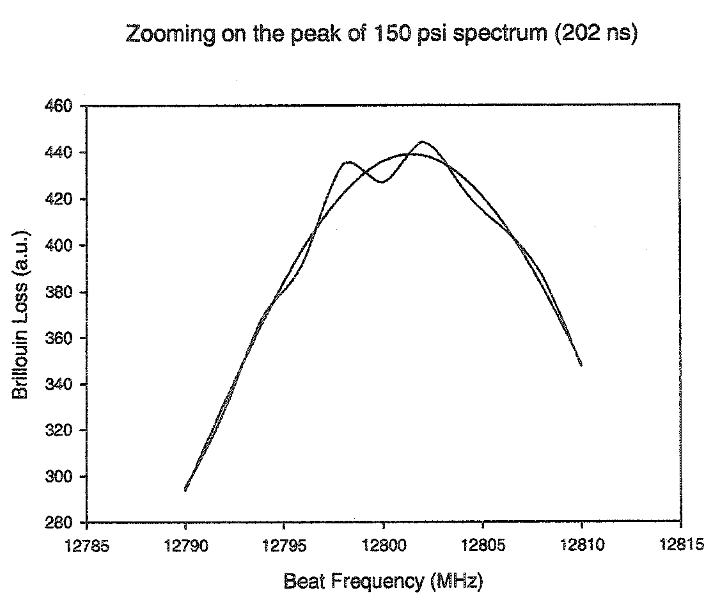

Figure 6.18: Zoomed view of the 150 psi Brillouin peak (bottom spectrum, Figure 6.16) and corresponding curve fit, which improves the Brillouin frequency by 1-2 MHz.

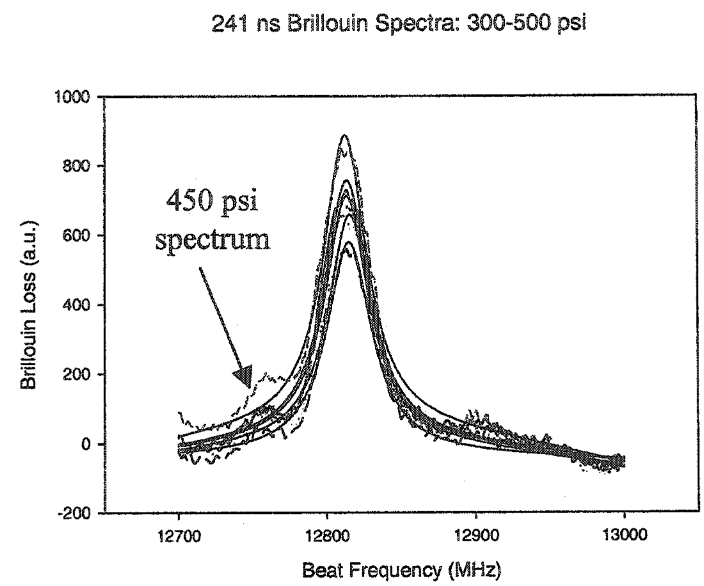

Figure 6.19: Brillouin spectra (and respective curve fits) from an attached fibre section for different pressures. The asymmetric 450-psi spectrum favours beat frequencies leftward from the Brillouin peak.

6.6 Summary and Future Research

Through hoop and axial strain measurements, varying sized defective regions were discriminated from those of unperturbed pipe regions using a 13 cm spatial resolution. Smaller defective regions (1.3 and 5.3 cm) were detected based on the increased average strain-pressure slopes within the 13 cm pulse. Therefore, research on this distributed Brillouin sensing technology should continue by acquiring strain measurements of more realistic longer and larger pipelines. The results of pressurizing such pipes will likely improve since the end-cap effects become negligible.

Of either hoop or axial fibre configurations, the axial is preferable by industry since pipeline failures often occur through axial bending and buckling due to shear stresses imposed by land movement. In addition, the axial configuration requires less fibre, and can thus traverse along potentially dynamic pipe positions in affordable fashion. Furthermore, when internally pressurized, pipelines tend to crack longitudinally (axial) rather than circumferentially (hoop) due to larger hoop stresses ($\sigma_h = 2\sigma_a$).

Chapter 7: Conclusions & Future Work

Highlights and key results in this thesis include:

1) Finding and characterizing two-fold Brillouin spectral profiles, occurring in the transient regime, and demonstrating their usefulness for temperature and strain measurements.
2) Identification of unwanted frequency cross-talk emerging from various fibre regions, and establishing system parameters to minimize effects.
3) Evaluating Brillouin temperature spectra for rapid threshold temperature measurements.
4) Demonstrating the Brillouin system's performance in monitoring the strain distributions in a pressurized pipeline under laboratory conditions.

In this thesis, advantages and disadvantages of improving the spatial resolution of the Brillouin scattering process, using short optical pulses, have been identified. Both the advantages and disadvantages originate from an electro-optic modulator, which always allows a small CW light component into the sensing fibre. The resulting narrow linewidth CW-CW interaction has been exploited to generate improved temperature and strain accuracies when short pulses having inherently broad spectra are used. However, this same interaction also exploits the BOTDA acquisition technique to generate frequency cross-talk from adjacent fibre regions, and effectively decreases the SNR and thus the temperature and strain accuracies. Hence, the amount of CW leakage should always be chosen carefully.

The interactions of the pulse and leakage (CW) components with an oncoming CW pump beam have been investigated in terms of pulse width and extinction ratio, and their combined effect has been found to generate a twofold Brillouin spectral profile. Hence, the spectral characterization was done utilizing a double-linewidth pseudo-Voigt profile. The frequency cross-talk limitations initiated by the CW-CW interaction have been investigated in terms of pulse width, linewidth, and extinction ratio, and have been overcome by analyzing the time-domain behaviour of the Brillouin signal. With an optimized SNR, this time-domain scheme can be tested experimentally.

Distributed Brillouin temperature spectra were successfully generated over 20 s time intervals, and can thus be used in dynamic threshold temperature ventures such as fire detection. From the Brillouin frequency, linewidth, and peak power relationships with temperature, the behaviour of the Brillouin temperature spectra can be predicted. However, to accurately utilize Brillouin temperature spectra in practice, the origins of spectral asymmetries must be well known. For instance, non-uniform heating rates can also artificially influence the Brillouin frequency- and hence temperature linewidths when the timeframe of temperature changes is shorter than the data acquisition time. However, at the present time, the temperature error for many fire detection applications is quite flexible (up to 5 - 6 °C), and the additional flexibility of making the threshold temperature much larger than room temperature can reduce the temperature error.

Using two different fibre configurations, varying sized defective regions within a 1.8 m end-capped pipeline were identified from their corresponding strain-pressure slopes. This was done despite having a 13 cm pulse width, which is larger than the defective region widths (1.3 and 5.3 cm). Future efforts on using Brillouin scattering for health monitoring of pipelines should continue along the outline presented in section 6.6.

The nature of spectral satellite peaks (Figure 7.1) is becoming a subject of intense investigation. Previous research [Brown 2000] indicates that they simply follow the main Brillouin peak as a function of temperature or strain, thus making them a material property. Furthermore, they appear to be independent of pulse width, thus eliminating the possibility of following the sinc frequency spectrum from rectangular time-domain pulses. However, in an experiment seeking to determine the Brillouin intensity vs. pump power (Figure 7.2), the satellite peaks were found to shift toward the Brillouin peak for large increasing pump powers (Figure 7.3). Furthermore, the numerical model discussed in Chapter 4 predicts oscillatory peaks arising from the non-instantaneous transient nature of the Brillouin interaction (see for example Figure 4.8). Future investigations along these lines may provide physical insight into these peaks, and determine whether the theoretical and experimental satellite peaks originate from the same phenomenon.

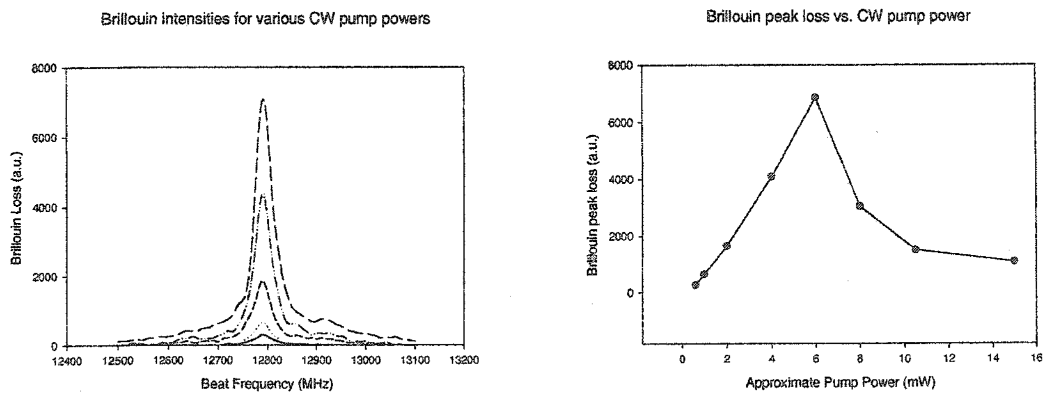

(a) (b)

Figure 7.1: Evolution of the Brillouin loss spectra (a) and corresponding Brillouin peak powers (b) versus pump power.

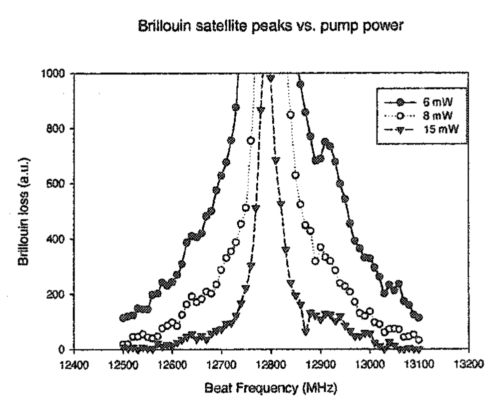

Figure 7.2: Zoomed view of Brillouin loss spectra obtained under high pump powers revealing a shift in the Brillouin side peaks.

Ongoing Brillouin scattering research is evolving into the 1550 nm wavelength regime since fibre optic components operating therein are widely available and inexpensive. However, although 1550 nm lasers are cheap, they lack the necessary stability to obtain accurate beat frequency measurements from our current configuration. For this reason, our group has recently developed a "frequency offset locking technique", which has successfully locked the beat frequency of 1550 nm distributed feedback (DFB) lasers within a 20 kHz frequency stability [Chen *et al.* 2003]. Fortunately, 20 kHz yields negligible error compared with desired temperature and strain errors (nominally ± 1 MHz → ± 1 °C or ± 20 με). With the implementation of this technology, a future 1550 nm system will explore longer fibre lengths due to the inherently reduced fibre loss.

References

[Afshar *et al.* 2003a] S. Afshar V., G. A. Ferrier, X. Bao, and L. Chen, "Brillouin spectral characterization of probe–pump distributed fiber optic sensors in the transient regime," submitted to *J. Lightwave Technol.*, July 2003.

[Afshar *et al.* 2003b] S. Afshar V., G. A. Ferrier, X. Bao, and L. Chen, "The impact of finite extinction ratio of EOM on the performance of distributed probe-pump Brillouin sensor systems," Accepted for publication in *Opt. Lett.*, August 2003.

[Afshaarvahid *et al.* 1998] S. Afshaarvahid, V. Devrelis, and J. Munch, "Nature of intensity and phase modulations in stimulated Brillouin scattering," *Phys. Rev. A*, **57**, pp. 3961-3971, 1998.

[Afshaarvahid and Munch 2001] S. Afshaarvahid and J. Munch, "A transient, 3-dimensional model of stimulated Brillouin scattering," *J. Nonlin. Opt. Phys. and Mat.*, **10** (1), pp. 1-27, 2001.

[Agrawal 1995] G. P. Agrawal, Nonlinear fiber optics. 2nd edition, Academic Press, Boston, USA, 1995.

[Agrawal 1997] G. P. Agrawal, Fibre optic communication systems. 2nd edition, John Wiley & Sons Inc., 1997.

[Alberta Energy Report 1998] Report of the Alberta Energy and Utilities Board, "Pipeline performance in Alberta 1980-1997," December 1998, http://www.eub.gov.ab.ca/bbs/documents/reports/r98g.pdf.

[Ashcroft and Mermin 1976] N. W. Ashcroft and N. D. Mermin, Solid State Physics. © Saunders College Publishing, pp. 421-450 (Chapter 22), 1976.

[Bao *et al.* 1993a] X. Bao, D. J. Webb, and D. A. Jackson, "22-km distributed temperature sensor using Brillouin gain in an optical fiber," *Opt. Lett.*, **18**, pp. 552-554, 1993.

[Bao *et al.* 1993b] X. Bao, D. J. Webb, and D. A. Jackson, "32-km distributed temperature sensor based on Brillouin loss in an optical fiber," *Opt. Lett.*, **18**, pp. 1561-1563, 1993.

[Bao *et al.* 1995] X. Bao, J. Dhliwayo, N. Heron, D. J. Webb, and D. A. Jackson, "Experimental and theoretical studies on a distributed temperature sensor based on Brillouin scattering," *J. Lightwave Tech.*, **13** (7), pp. 1340-1348, 1995.

[Bao *et al.* 1995b] X. Bao, D. J. Webb, D. A. Jackson, "Recent progress in distributed fibre optic sensors based upon Brillouin scattering," Invited paper, Proc. SPIE, **2507**, pp. 175-185, 1995.

[Bao *et al.* 1996] X. Bao, D. J. Webb, and D. A. Jackson, "Distributed temperature sensor based on Brillouin loss in an optical fiber for transient threshold monitoring," Canadian Journal of Physics, **74**, pp. 1-3, 1996.

[Bao *et al.* 1999] X. Bao, A. W. Brown, M. DeMerchant, and J. Smith, "Characterization of the Brillouin-loss spectrum of single-mode fibers by use of very short (<10-ns) pulses," *Opt. Lett.*, **24** (8), pp. 510-512, 1999.

[Bao *et al.* 2001] X. Bao, M. DeMerchant, A. Brown, and T. Bremner, "Tensile and compressive strain measurement in the lab and field with the distributed Brillouin scattering sensor," *J. Lightwave Tech.*, **19** (11), pp. 1698-1704, 2001.

[Barber 2001] J. R. Barber, Intermediate mechanics of materials. © McGraw-Hill Companies, Inc., pp. 440-443, 2001.

[Basnett and Barber 1994] T. Basnett and S. J. Barber, "Distributed temperature measurement with optical fibres," – System document, Cossor Electronics Ltd, Harlow, Essex, 1994.

[Bass *et al.* 1962a] M. Bass, P. A. Franken, A. E. Hill, C. W. Peters, and G. Weinreich, "Optical mixing," *Phys. Rev. Lett.*, **8** (1), pp. 18, 1962.

[Bass *et al.* 1962b] M. Bass, P. A. Franken, J. F. Ward, and G. Weinreich, "Optical rectification," *Phys. Rev. Lett.*, **9** (11), pp. 446-448, 1962.

[Boyd 1992] R. W. Boyd, Nonlinear optics. Academic Press, San Diego, California, USA, 1992.

[Boyd and Rzazewski 1990] R. W. Boyd and K. Rzazewski, "Noise initiation of stimulated Brillouin scattering," *Phys. Rev. A*, **42** (9), pp. 5514-5521, 1990.

[Brillouin 1922] L. Brillouin, "Diffusion de la lumière et des rayons X par un corps transparent homgène," *Ann. Physique.* (Paris), **17** (88), 1922.

[Brown *et al.* 1998] A. W. Brown, M. DeMerchant, X. Bao, and T. Bremner, "Advances in distributed sensing using Brillouin scattering," Proc. SPIE, **3330**, pp. 294-300, 1998.

[Brown *et al.* 1999] A. W. Brown, M. D. DeMerchant, X. Bao, and T. W. Bremner, "Spatial resolution enhancement of a Brillouin distributed sensor using a novel signal processing method," *J. Lightwave Technol.*, **17**, pp. 1179-1183, 1999.

[Brown 2000] A. W. Brown, "Development of a Brillouin scattering based distributed fiber optic strain sensor," Ph.D. Thesis, University of New Brunswick, 2000.

[Budynas 1999a] R. G. Budynas, Advanced strength and applied stress analysis. © McGraw-Hill Companies, Inc., pp. 348-357, 1999.

[Budynas 1999b] R. G. Budynas, Advanced strength and applied stress analysis. © McGraw-Hill Companies, Inc., pp. 364-371, 1999.

[Chen *et al.* 2003] O. Chen, L. Zou, G. Wu, D. Falk, J. Bernard, and X. Bao, "Frequency stabilized 1550 nm lasers for distributed fiber optic Brillouin sensor systems," Poster Session, 8th Annual ISIS Canada Conference, 2003.

[Corning 1998] Corning, "SMF-28 CPC6 single-mode optical fiber product information," Corning Inc., Corning N.Y., 1998.

[DeMerchant 2000] M. DeMerchant, "Distributed strain sensing for civil engineering applications," Ph.D. Thesis, University of New Brunswick, 2000.

[DeMerchant *et al.* 2000], M. D. DeMerchant, A. W. Brown, J. Smith, X. Bao, and T. Bremner, "Distributed strain sensing for structural monitoring applications," *Can. J. Civil. Eng.*, **27**, pp. 873-879, 2000.

[Ericsson 1994] Ericsson Network Engineering AB, Sundbyberg, Sweden, "Distributed temperature measurement using optical fibres," – System Document, 1994.

[Fellay *et al.* 1997] A. Fellay, L. Thévenaz, M. Facchini, M. Niklès, and P. Robert, "Distributed sensing using stimulated Brillouin scattering: towards ultimate resolution," OSA Technical Digest Series, **16**, pp. 324-327, 1997.

[Ferrier *et al.* 2003] G. A. Ferrier, S. Afshar V., X. Bao, and L. Chen, "A new spectral fitting method for distributed Brillouin sensing in the transient regime," submitted to *J. Lightwave Tech.*, March 2003.

[Franken *et al.* 1961] P. A. Franken, A. E. Hill, C. W. Peters, and G. Weinreich, "Generation of optical harmonics," *Phys. Rev. Lett.*, **7** (4), pp. 118-119, 1961.

[Fujii 1980] Y. Fujii, B. S. Kawasaki, K. O. Hill, and D. C. Johnson, "Sum-frequency light generation in optical fibers," *Opt. Lett.*, **5** (2), pp. 48-50, 1980.

[Heckman 1998] D. Heckman, "Finite element analysis of pressure vessels," Intern papers of the Monterey Bay Aquarium Research Institute (MBARI) 1998, http://www.mbari.org/education/internship/98interns/98internpapers/98heckman.pdf.

[Hecht 1999] J. Hecht, Understanding fiber optics – 3rd edition. © Prentice-Hall Inc., pp. 308, 1999.

[Horiguchi *et al.* 1990] T. Horiguchi, T. Kurashima, and M. Tateda, "A technique to measure distributed strain in optical fibres," *IEEE Photon. Technol. Lett.*, **2**, pp. 352-354, 1990.

[Horiguchi *et al.* 1995] T. Horiguchi, K. Shimizu, T. Kurashima, M. Tateda, and Y. Koyamada, "Development of a distributed sensing technique using Brillouin scattering," *J. Lightwave Tech.*, **13**, pp. 1296-1302, 1995.

[Iida *et al.* 1994] O. Iida, D. Onoda, S. Kono, K. Hshiba, and S. Ohsawa, "Expansion of measuring range for a fiber-optic distributed temperature sensor and applications to commercial plants," IMTC'94, May 1994, Hamamatsu, Japan.

[Imai and Shimada 1993] Y. Imai and N. Shimada, "Dependence of stimulated Brillouin scattering on temperature distribution in polarization-maintaining fibers," *IEEE Photon. Technol. Lett.*, **5** (11), pp. 1335-1337, 1993.

[Kaiser and Maier 1972] W. Kaiser and M. Maier, "Stimulated Rayleigh, Brillouin and Raman spectroscopy," Laser Handbook, vol. 2, North-Holland, Amsterdam, 1972.

[Kurashima *et al.* 1990] T. Kurashima, T. Horiguchi, and M. Tateda, "Thermal effects on the Brillouin frequency shift in jacketed optical silica fibers," *Appl. Opt.*, **29**, pp. 2219-2222, 1990.

[Lee 1986] D. L. Lee, Electromagnetic principles of integrated optics. John Wiley & Sons Inc., pp. 224-231, 1986.

[Lecoeuche *et al.* 2000] V. Lecoeuche, D. J. Webb, C. N. Pannell, and D. A. Jackson, "Transient response in high-resolution Brillouin-based distributed sensing using probe pulses shorter than the acoustic relaxation time," *Opt. Lett.*, **25**, pp. 156-158, 2000.

[Liu *et al.* 2002] Z. Liu, G. Ferrier, X. Bao, X. Zeng, Q. Yu, and A. Kim, "Brillouin scattering based distributed fiber optic temperature sensing for fire detection," presented at the 7th International Symposium on Fire Safety Science, Worcester, Massachusetts, USA, June 2002.

[Maegerle 2001] R. Maegerle, "Fire protection systems for traffic tunnels under test," 12th International Conference on Automatic Fire Detection, March 2001, Gaithersburg, USA.

[Marquardt 1963] D. W. Marquardt, "An algorithm for least squares estimation of parameters," *J. Soc. Ind. and Appl. Math.* **11**, pp. 431-441, 1963.

[Mauro 2003] J. Mauro, "Raman amplification of optical signals," Web article, http://cs.alfred.edu/~maurojc/papers/pdf/raman.pdf, Accessed July 26, 2003.

[Meacham 1994] B. J. Meacham, "International developments in fire sensor technology," *J. of Fire Protection Engineering*, **6** (2), pp. 89-98, 1994.

[Mills 1998] D. L. Mills, Nonlinear Optics: Basic Concepts. © Springer-Verlag, pp. 73-82, 1998.

[Moll 2002] K. D. Moll, D. Homoelle, A. L. Gaeta, and R. W. Boyd, "Conical harmonic generation in isotropic materials," *Phys. Rev. Lett.*, **88** (15), 153901, 2002.

[Morgan 2000] A. Morgan, "New fire detection concepts with fibre optics technology," *Fire Safety Engineering*, pp. 35-37, 2000.

[Naruse and Tateda 1999] H. Naruse and M. Tateda, "Trade-off between the spatial and the frequency resolutions in measuring the power spectrum of the Brillouin backscattered light in an optical fibre," *Appl. Opt.* **38**, pp. 6516-6521, 1999.

[Naruse and Tateda 2000] H. Naruse and M. Tateda, "Launched pulse-shape dependence of the power spectrum of the spontaneous Brillouin backscattered light in an optical fiber," *Appl. Opt.,* **39** (34), pp. 6376-6384, 2000.

[Niklès *et al.* 1997] M. Niklès, L. Thévenaz, and P. A. Robert, "Brillouin gain spectrum characterization in single-mode optical fibres," *J. Lightwave Technol.* **15**, pp. 1842-1851, 1997.

[Parker *et al.* 1997] T. R. Parker, M. Farhadiroushan, V. A. Handerek, and A. J. Rogers, "Temperature and strain dependence of the power level and frequency on spontaneous Brillouin scattering in optical fibers," *Opt. Lett.* **22** (11), pp. 787-789, 1997.

[Pedrotti and Pedrotti 1993] F. L. Pedrotti and L. S. Pedrotti, Introduction to optics – second edition. Prentice Hall Inc., 1993.

[Raman, 1928] C. V. Raman and K. S. Krishnan, "A new radiation," *Indian J. Phys.*, **2**, p. 387, 1928.

[Rogers 2000] A. J. Rogers, "Nonlinear optics and optical fibers," in Optical fiber sensor technology. edited by K.T.V. Grattan and B.T. Meggitt, pp. 219-225, 2001.

[Shen 1984] Y. R. Shen, Principles of nonlinear optics. Wiley, New York, pp. 1-2, 1984.

[Shiraki *et al.* 1996] K. Shiraki, M. Ohashi, and M. Tateda, "SBS threshold of a fiber with a Brillouin frequency shift distribution," *J. Lightwave Tech.*, **14** (1), pp. 50-57, 1996.

[Smith 1972] R. G. Smith, "Optical power handling capacity of low loss optical fibres as determined by stimulated Raman and Brillouin scattering," *Appl. Opt.*, **11**, pp. 2489-2494, 1972.

[Smith 1999] J. Smith, "Characterization of the Brillouin loss spectrum for simultaneous distributed sensing of strain and temperature," M.Sc. Thesis, University of New Brunswick, 1999.

[Smith *et al.* 1999] J. Smith, A. Brown, M. DeMerchant, and X. Bao, "Simultaneous distributed strain and temperature measurement," *Appl. Opt.*, **38** (25), pp. 5372-5377, 1999.

[Smith *et al.* 1999b] J. Smith, A. Brown, M. DeMerchant, and X. Bao, "Pulse width dependence of the Brillouin loss spectrum," *Opt. Commun.*, **168**, pp. 393-398, 1999.

[Stolen and Lin 1978] R. H. Stolen and C. Lin, "Self phase modulation in silica optical fibers," *Phys. Rev. A.*, **17** (4), pp. 1448-1453, 1978.

[Sugimoto *et al.* 1999] N. Sugimoto, T. Shintaku, A. Tate, H. Terui, M. Shimokozono, E. Kubota, M. Ishii, and Y. Inoue, "Waveguide polarization-independent optical circulator," *IEEE Phot. Tech. Lett.* **11** (3), pp. 355-357, 1999.

[Tang 1966] C. L. Tang, "Saturation and spectral characteristics of the Stokes emission in the stimulated Brillouin process," *J. Appl. Phys.*, **37**, pp. 2945-2955, 1966.

[Tapanes 2001] E. Tapanes, "Fibre optic sensing solutions for real-time pipeline integrity monitoring," Australian Pipeline Industry Association National Convention, October 27-30, 2001, http://www.iceweb.com.au/Newtech/FFT_Pipeline_Integrity_Paper.pdf.

[USA Safety Report 2001] Report of the US National Transportation Safety Board, "Pipeline accident brief," July 6, 2001, http://www.ntsb.gov/publictn/2001/PAB0103.htm.

[Valley 1986] G. C. Valley, "A review of stimulated Brillouin scattering excited with a broad-band pump laser," *IEEE Journal of Quantum Electronics*, **22**, pp. 704-705, 1986.

[Wang *et al.* 2001] A. Wang, W. Liu, X. Li, C. Yue, Y. Wang, Q. Wang, and X. Cai, "Distributed optical fiber temperature detecting and alarm system," 12th International Conference on Automatic Fire Detection, March 2001, Gaithersburg, USA.

[Yariv 1971] A. Yariv, Introduction to optical electronics. © Holt, Rinehart, and Winston, Inc., pp. 178-186, 1971.

[Yariv 1989] A. Yariv, Quantum electronics – 3rd edition. © John Wiley & Sons Inc., pp. 631-640, 1989.

[Yeniay 2002] A. Yeniay, J.-M. Delavaux, and J. Toulouse, "Spontaneous and stimulated Brillouin scattering gain spectra in optical fibers," *J. Lightwave Tech.*, **20** (8), pp. 1425-32, 2002.

[Zeng 2003] X. Zeng, "Characterization and application of Brillouin scattering based distributed fiber optic sensor," M.Sc. thesis, University of Ottawa, 2003.

[Zou *et al.* 2003] L. Zou, G. A. Ferrier, S. Afshar V., Q. Yu, L. Chen, and X. Bao, "Distributed Brillouin scattering sensor for discrimination of wall thinning defects in steel pipe under internal pressure," submitted to *Appl. Opt.*, August 2003.

Appendix A: Derivation of the minimum detectable Brillouin frequency shift

Experimentally, the performance of distributed Brillouin sensors is dependent on the minimum detectable frequency shift, which depends on the Brillouin linewidth and signal-to-noise ratio (SNR). On a qualitative level, this frequency shift can be determined by calculating the behaviour of the Brillouin spectrum near its peak [Naruse and Tateda 2000]. Consider a minimum Brillouin frequency shift, $\delta\nu_B = \nu - \nu_B \neq 0$, and the pseudo-Voigt Brillouin loss spectral function given by Equation 4.2. Near the Brillouin loss maximum, i.e. $\nu - \nu_B$, the function can be approximated by a Taylor series expansion:

$$g(\nu) = g(\nu_B) + \frac{\partial^2 g(\nu_B)}{\partial \nu^2}\frac{(\nu - \nu_B)^2}{2}. \tag{A.1}$$

Since the second derivative term and the RMS optical noise power are

$$\frac{\partial^2 g(\nu_B)}{\partial \nu^2} = -8g_0\left[\frac{\beta}{\gamma_1^{\ 2}} + \frac{(1-\beta)\ln 2}{\gamma_2^{\ 2}}\right], \qquad g_N = \tfrac{1}{2}\left|g(\nu) - g(\nu_B)\right|, \tag{A.2}$$

the minimum Brillouin frequency shift becomes

$$\delta\nu_B = \nu - \nu_B = \sqrt{\frac{g_N}{2g_0\left[\frac{\beta}{\gamma_1^{\ 2}} + \frac{(1-\beta)\ln 2}{\gamma_2^{\ 2}}\right]}} \tag{A.3}$$

The signal-to-noise ratio (*SNR*) is the ratio of the electrical signal to its rms noise, and since the electrical signal power obtained by photoelectric conversion is proportional to the square of the received optical power [Naruse and Tateda 2000], the *SNR* is:

$$SNR = (P_0/P_N)_{electrical} = (P_0/P_N)^2_{optical} = (g_0/g_N)^2 \tag{A.4}$$

Therefore, the minimum detectable Brillouin frequency shift is

$$\delta\nu_B = \frac{1}{\sqrt{2}(SNR)^{1/4}}\sqrt{\frac{\gamma_1^{\ 2}\gamma_2^{\ 2}}{\beta\gamma_2^{\ 2} + (1-\beta)\gamma_1^{\ 2}\ln 2}} \tag{A.5}$$

and varies between $\frac{\gamma_1}{\sqrt{2}(SNR)^{1/4}}$ [Horiguchi *et al.* 1995] and $\frac{\gamma_2}{\sqrt{2\ln 2}(SNR)^{1/4}}$ as the spectrum changes from a Lorentzian ($\beta = 1$) to a Gaussian ($\beta = 0$) form.

Appendix B: Impact of Brillouin peak power variations on the Brillouin temperature spectrum

The following is a series of Maple commands, which illustrates the impact of Brillouin peak power and Brillouin frequency linewidth on the Brillouin temperature spectrum.

We begin with Equation 5.7:

```
> restart; P:=(P0+mu*(T-T0))/(1+4*((eta-T)/kappa)^2);
```

$$P := \frac{P0 + \mu\,(T - T0)}{1 + \frac{4\,(\eta - T)^2}{\kappa^2}}$$

Using Equation 5.5, we then determine an expression for the first derivative dP/dT.

```
> kappa:=(alpha+beta*(T-tau))/Ct; First_derivative:=diff(P,T);
```

$$\kappa := \frac{\alpha + \beta\,(T - \tau)}{Ct}$$

$$First\_derivative := \frac{\mu}{1 + \frac{4\,(\eta - T)^2\,Ct^2}{(\alpha + \beta\,(T-\tau))^2}} - \frac{(P0 + \mu\,(T - T0))\left(-\frac{8\,(\eta - T)\,Ct^2}{(\alpha + \beta\,(T - \tau))^2} - \frac{8\,(\eta - T)^2\,Ct^2\,\beta}{(\alpha + \beta\,(T - \tau))^3}\right)}{\left(1 + \frac{4\,(\eta - T)^2\,Ct^2}{(\alpha + \beta\,(T - \tau))^2}\right)^2}$$

When the Brillouin peak power is invariant with temperature, $\mu = 0$. The Brillouin temperature intensity maximum occurs when the first derivative dP/dT=0, and the second derivative is negative. Here, we find that two solutions satisfy the first requirement. The first solution, η=T, is expected. However, the second solution arises from the Brillouin frequency linewidth dependence on temperature.

```
> mu:=0; solve(First_derivative=0,T);
```

$$\mu := 0$$

$$\eta,\ \frac{-\alpha + \beta\,\tau}{\beta}$$

Here, we give some typical values in MHz and °C

```
> alpha:=31.8; beta:=-0.173; tau:=23; T0:=40; eta:=40;
mu:=1000e-6; P0:=1; Ct:=1.22;
```

$\alpha := 31.8$ $\eta := 40$

$\beta := -0.173$ $\mu := 0.001000$

$\tau := 23$ $P0 := 1$

$T0 := 40$ $Ct := 1.22$

Calculating the second derivative...(omitting the large expression for simplicity)

```
> Second_derivative:=diff(First_derivative, T):
```

Determining the roots of the second derivative...

```
> solve(Second_derivative=0,T);
```

$$-0.1652160778\,10^{8},\ 33.34317499,\ 46.96602241,\ 312.6415622,\ 0.1652041650\,10^{8}$$

By picking values of T between these roots, we determine the range(s) of T whereby the second derivative is positive and negative.

```
> T:=20; Second_derivative; T:=40; Second_derivative; T:=300;
Second_derivative; T:=600; Second_derivative;
```

$T := 20$

0.001710632657

$T := 40$

-0.01429707160

$T := 300$

$0.8531058610\,10^{-8}$

$T := 600$

$-0.8972112231\,10^{-8}$

We find two regions having a negative second derivative...however, only one is practical. By solving for the roots of the first derivative, we find that 40.06985412 °C is the new shifted maximum temperature.

```
> solve(First_derivative=0,T);
```

$$206.8150289,\ -41.77365809 - 570.7042447\,I,\ -41.77365809 + 570.7042447\,I,\ 40.06985412$$

Here, we find that the amount of shift in the Brillouin temperature maximum depends highly on the ratio between the original Brillouin peak power and the rate at which it changes with temperature.

When the original Brillouin peak power is much larger than its variation, then the temperature shift is small. On the other hand, larger shifts are possible when the peak power and its variation are comparable in size.

```
>mu:=1e-6: P0:=1: fsolve(First_derivative=0,T,T=0..100);
```

40.00006994

```
>mu:=1: P0:=1e6: fsolve(First_derivative=0,T,T=0..100);
```

40.00006994

```
>mu:=1: P0:=1: fsolve(First_derivative=0,T,T=0..100);
```

49.61740290

Appendix C: Publications and Conferences

C.1 Refereed Publications

- S. Afshar V., **G. A. Ferrier**, X. Bao, and L. Chen, "The impact of finite extinction ratio of EOM on the performance of distributed probe-pump Brillouin sensor systems," accepted for publication in Optics Letters, August 2003.

- S. Afshar V., **G. A. Ferrier**, X. Bao, and L. Chen, "Brillouin spectral characterization of probe-pump distributed fiber optic sensors in the transient regime," submitted to IEEE Journal of Lightwave Technology, July 2003.

- L. Zou, **G. A. Ferrier**, S. Afshar V., Q. Yu, L. Chen, and X. Bao, "Distributed Brillouin scattering sensor for discrimination of wall thinning defects in steel pipe under internal pressure," submitted to Applied Optics, 2003.

- **G. A. Ferrier**, S. Afshar V., X. Bao, and L. Chen, "A new spectral fitting method for distributed Brillouin sensing in the transient regime," submitted to IEEE Journal of Lightwave Technology, March 2003.

- X. Zeng, X. Bao, C. Y. Chhoa, T. W. Bremner, A. W. Brown, M. D. DeMerchant, **G. Ferrier**, A. L. Kalamkarov, and A. V. Georgiades, "Strain measurement in a concrete beam using the Brillouin scattering based distributed fiber sensor with single mode fibers embedded in GFRP rod and bonded to steel reinforcing bars," *Applied Optics*, **41** (27), 2002.

C.2 Conference Papers

- L. Zou, **G. A. Ferrier**, S. Afshar V., and X. Bao, "Structural health monitoring of pipelines with distributed Brillouin sensor," will be published in the Proceedings of 1st International Conference on Structural Health Monitoring and Intelligent Infrastructure, 2003.

- L. Zou, **G. A. Ferrier**, S. Afshar V., Q. Yu, and X. Bao, "Distributed Brillouin scattering sensor as structural health monitoring system for pipeline integrity monitoring," will be published in the Proceedings of 16th International Conference on Optical Fiber Sensors, 2003.

- Z. Liu, **G. Ferrier**, X. Bao, X. Zeng, Q. Yu, A. Kim, "Brillouin scattering based distributed fiber optic temperature sensing for fire detection," presented at 7th International Symposium on Fire Safety Science, Worcester, Massachusetts, USA, June 2002.

- X. Zeng, Q. Yu, **G. Ferrier**, and X. Bao, "Strain and temperature monitoring of a concrete structure using a distributed Brillouin scattering sensor," in proceedings of the 1st International Workshop on Structural Health Monitoring of Innovative Civil Engineering Structures, Winnipeg, Canada, in print 2002.

- X. Zeng, Q. Yu, **G. Ferrier**, X. Bao, R. E. Steffen, and M. Bowman, "Strain Measurement of the Load Test on the Rollinsford Bridge Using the Distributed Brillouin Sensor," in proceedings of the 1st International Workshop on Structural Health Monitoring of Innovative Civil Engineering Structures, Winnipeg, Canada, in print 2002.

C.3 Oral Presentations

- "A new fitting method for spectral characterization of Brillouin-based distributed sensors," Photonics North, Montreal, Canada, May 2003.

- "Structural health monitoring of pipelines with Brillouin sensors," 8th Annual Conference of ISIS Canada, Vancouver, Canada, May 2003.

- "Taking distributed fibre optic sensors outside," 7th Annual Conference of ISIS Canada, Winnipeg, Canada, May 2002.

C.4 Posters

- **G. Ferrier**, S. Afshar V., X. Zeng, Q. Yu, and X. Bao, "Distributed temperature and strain sensing of concrete structures using stimulated Brillouin scattering in optical fibers," poster session, 7th Annual Conference of ISIS Canada, May 2002.
  - ✓ Received prize for "Most Creative Poster".

- S. Afshar V., **G. Ferrier**, and X. Bao, "New advances in the design of distributed, SBS-based fiber optic sensors," poster session, 7th Annual Conference of ISIS Canada, May 2002.

- Q. Yu, **G. Ferrier**, S. Afshar V., O. Chen, and X. Bao, "Polarization maintaining fiber & fiber Bragg gratings for simultaneous measurement of strain and temperature," poster session, 7th Annual Conference of ISIS Canada, May 2002.